

# Proof of concept of a calibration method for the laser Raman system for KATRIN based on the determination of the system's spectral sensitivity

Simone Rupp

Diplomarbeit

bei Prof. Dr. G. Drexlin  
Institut für experimentelle Kernphysik, Fakultät für Physik,  
Karlsruher Institut für Technologie

Korreferent Prof. Dr. H. H. Telle  
Department of Physics, Swansea University (Wales)

FAKULTÄT FÜR PHYSIK  
KARLSRUHER INSTITUT FÜR TECHNOLOGIE

14. DEZEMBER 2012



# Erklärung

Hiermit versichere ich, die vorliegende Arbeit selbständig angefertigt, alle dem Wortlaut oder Sinn nach entnommenen Inhalte anderer Werke an den entsprechenden Stellen unter Angabe der Quellen kenntlich gemacht und keine weiteren Hilfsmittel verwendet zu haben.

Simone Rupp  
Karlsruhe, den 14. Dezember 2012



# Zusammenfassung

Im Folgenden wird der Inhalt der vorliegenden Arbeit kurz zusammengefasst. Für eine ausführliche Darstellung mit den dazugehörigen Quellenangaben sei auf den anschließenden englischen Haupttext verwiesen.

Das Ziel des KATRIN-Experiments (**K**ARlsruhe **TR**Itium Neutrino Experiment) ist die modellunabhängige Bestimmung der Neutrinomasse mit einer Sensitivität von 200 meV. Dazu wird das Spektrum von  $\beta$ -Elektronen aus dem Zerfall von Tritium im Bereich des kinematischen Endpunktes von 18,6 keV untersucht. Für die Messungen werden eine fensterlose, gasförmige Tritiumquelle mit hoher Luminosität und ein hochauflösender elektrostatischer Hochpassfilter verwendet.

Die angestrebte Sensitivität kann nur erreicht werden, wenn statistische und systematische Unsicherheiten in allen Bereichen des Experiments minimiert werden. In Bezug auf die systematischen Unsicherheiten ist die Stabilisierung und Überwachung wesentlicher Parameter des Experiments von entscheidender Bedeutung. Ein solcher Parameter ist die isotopische Reinheit  $\epsilon_T$  des Tritiumgases, das in die Quelle eingespeist wird. Es besteht hauptsächlich aus molekularem Tritium ( $T_2$ ), enthält aber auch Anteile aller anderen Wasserstoffisotope (DT, D<sub>2</sub>, HD, HT und H<sub>2</sub>).

Eine Änderung der isotopischen Reinheit und damit der Aktivität der Quelle wirkt sich direkt auf die gemessene Zählrate der  $\beta$ -Elektronen aus. Außerdem wird das gemessene Spektrum von sekundären, gasartabhängigen Effekten beeinflusst, wie zum Beispiel unterschiedlichen Rückstoßenergien des Tochterkerns oder einer anderen Wahrscheinlichkeitsverteilung der Endzustände, die das Tochtermolekül nach dem Zerfall einnehmen kann. Aus diesem Grund muss die Zusammensetzung des Tritiumgases kontinuierlich mit einer Präzision von 0,1% und einer Richtigkeit von 10% oder besser überwacht werden.

Zur Messung der Gaszusammensetzung wird ein eigens entwickeltes Laser-Raman-System verwendet. Raman-Spektroskopie ermöglicht die kontinuierliche, simultane Überwachung aller sechs Wasserstoffisotope mit der geforderten Präzision. Eine genaue Kalibrierung des Raman-Systems ist erforderlich, um eine hohe Messrichtigkeit zu erreichen.

Im Rahmen dieser Arbeit wurde ein mögliches Kalibrierverfahren untersucht, das auf einer Kombination aus der experimentell bestimmten spektralen Sensitivität des Raman-Systems und theoretisch berechneten Raman-Intensitäten basiert. Der Fokus der Arbeit lag auf der Bestimmung der spektralen Sensitivität.

Im Vergleich verschiedener Lichtquellen zur Kalibrierung wurden die Vorteile eines sogenannten Lumineszenzstandards deutlich. In einer Reihe von Messungen wurde untersucht, ob der Lumineszenzstandard für die angedachte Aufgabe anwendbar ist. Dabei wurde der

Einfluss von verschiedenen Faktoren wie z.B. der Laserpolarisation auf das Messergebnis studiert. Aus den Ergebnissen konnte ein Ablaufplan für die Messung zur Bestimmung der spektralen Sensitivität entwickelt werden, dessen Einhaltung zu den korrekten Ergebnissen führt; deren Gültigkeit wurde mithilfe von geeigneten Gegenproben bestätigt.

Aus der gemessenen spektralen Sensitivität in Kombination mit theoretischen Raman-Intensitäten konnten die Kalibrierfaktoren, die sogenannten Responsefunktionen  $R$ , für alle sechs Wasserstoffisotopologe bestimmt werden. Mithilfe einer zweiten, unabhängigen Kalibriermethode, welche auf der Herstellung von Gasgemischen genau bekannter Zusammensetzung basiert, konnten die Responsefunktionen der drei inaktiven Isotopologe  $H_2$ ,  $HD$  und  $D_2$  verifiziert werden. Es wurde gezeigt, dass die Anforderungen des KATRIN-Experiments an die Messrichtigkeit des Laser-Raman-Systems erfüllt werden können.

Im Folgenden wird ein kurzer Überblick über die einzelnen Kapitel dieser Arbeit gegeben:

**1. Einführung** Die vorliegende Arbeit beschäftigt sich mit Methoden für die Kalibrierung des Laser-Raman-Systems für KATRIN. KATRIN ist ein Experiment, dessen Ziel die Messung der Masse des Antielektronneutrinos mit bisher unerreichter Sensitivität ist. Die Bestimmung der Neutrinomassen ist von großer Bedeutung für aktuelle Fragestellungen im Bereich der Teilchenphysik ebenso wie der Kosmologie. Die Kenntnis der Neutrinomassen kann erheblich zum Verständnis des Mechanismus beitragen, durch den diese Massen erzeugt werden. Erkenntnisse erhofft man sich auch zur Strukturbildung im Universum, bei der die Neutrinos als sogenannte heiße dunkle Materie eine Rolle gespielt haben.

Zur Bestimmung der Neutrinomasse gibt es verschiedene Verfahren. Die derzeit sensitivste modellunabhängige Methode basiert auf der Untersuchung der Kinematik von schwachen Zerfällen. Diese Methode macht sich auch das KATRIN-Experiment zunutze.

**2. Das KATRIN-Experiment** Das KATRIN-Experiment untersucht das Elektronenspektrum des  $\beta$ -Zerfalls von Tritium, um die Neutrinomasse zu bestimmen. Die Form des Spektrums der Zerfallselektronen in der Nähe des kinematischen Endpunktes hängt von der Neutrinomasse ab. Das Spektrum wird mithilfe eines sogenannten MAC-E-Filters<sup>1</sup> genau vermessen. Die Neutrinoexperimente in Troitsk und Mainz, die einen ebensolchen Filter verwendet hatten, lieferten die bisher beste Neutrinomassenobergrenze von 2 eV. Mit dem KATRIN-Experiment soll diese Obergrenze um eine Größenordnung auf 200 meV reduziert werden. Um dieses Ziel zu erreichen, müssen statistische und systematische Unsicherheiten minimiert werden. In Bezug auf die Tritiumquelle ist daher eine kontinuierliche Überwachung der Zusammensetzung des Tritiumgases mit einer Präzision von  $<0,1\%$  und einer Messrichtigkeit von 10% erforderlich.

**3. Quantitative Raman-Spektroskopie für KATRIN** Der Raman-Effekt beschreibt die inelastische Streuung von Licht an Molekülen. Die Wellenlängenverschiebung, die das gestreute Licht erfährt, ist charakteristisch für das Molekül, an dem gestreut wird. Daher ist Laser-Raman-Spektroskopie eine geeignete Methode, um die Zusammensetzung einer Gasmischung, die alle Wasserstoffisotopologe enthält, zu überwachen. Da die Intensität

---

<sup>1</sup>Magnetic Adiabatic Collimation and Electrostatic Filter

der Raman-Linien eines Moleküls proportional zur Anzahl dieser Molekülsorte im Streuvolumen ist, kann aus dem Raman-Spektrum eines Gases auf dessen Zusammensetzung geschlossen werden. Dazu muss allerdings die dazugehörige Proportionalitätskonstante bekannt sein. Diese molekül- und systemabhängige Konstante wird Responsefunktion genannt. Sie ist ein Maß für den Wirkungsquerschnitt dieses Moleküls mit dem Laserlicht, berücksichtigt aber auch die Sensitivität des Messsystems auf Licht der Streuwellenlängen.

Um Raman-Spektren für KATRIN quantitativ analysieren zu können, ist eine Bestimmung der Responsefunktionen aller Wasserstoffisotope nötig, d.h. eine Kalibrierung des Raman-Systems. Es gibt verschiedene Möglichkeiten für eine solche Kalibrierung. Falls man Gas von genau bekannter Zusammensetzung zur Verfügung hat, entweder weil die Gaszusammensetzung über eine Referenzmethode bestimmt wurde oder weil die Gasmischung auf kontrollierte Art in bekannter Zusammensetzung hergestellt wurde, können die Responsefunktionen über die Messung des Raman-Spektrums dieser Gas Mischung erhalten werden. Allerdings kann diese Methode derzeit nicht mit der geforderten Messrichtigkeit auf tritiierte Gas Mischungen angewandt werden. Eine zweite Möglichkeit zur Bestimmung der Responsefunktionen ist die Berechnung von theoretischen Raman-Linienintensitäten, die dann mit der spektralen Sensitivität des Messsystems kombiniert werden. Diese Methode erfordert allerdings eine Verifizierung der eingehenden theoretisch berechneten Werte.

Aus diesem Grund wird eine Kombination beider Ansätze vorgeschlagen: Die Responsefunktionen aller Isotope werden mithilfe der zweiten Methode bestimmt; mithilfe der ersten Methode können die erhaltenen Werte dann für die inaktiven Isotope verifiziert werden. Eine erfolgreiche Verifizierung würde für die Korrektheit der zugrundeliegenden Berechnungen und damit aller berechneten Responsefunktionen sprechen.

**4. Kalibrierung basierend auf theoretischen Raman-Signalstärken** Für die Bestimmung der Responsefunktionen wie unter 3. beschrieben muss die spektrale Sensitivität des Messsystems bekannt sein. Diese kann mithilfe einer Kalibrierlichtquelle experimentell bestimmt werden. Da das Spektrum einer solchen Lichtquelle bekannt ist, ergibt sich die spektrale Sensitivität aus dem Vergleich des theoretischen mit dem tatsächlich gemessenen Spektrum.

Im Vergleich möglicher Lichtquellen erweist sich ein NIST-zertifizierter Lumineszenzstandard als besonders vorteilhaft. Allerdings weichen die Messbedingungen, unter denen die spektrale Sensitivität im Falle des KATRIN Laser-Raman-Systems bestimmt werden muss, von denjenigen ab, für die der Standard zertifiziert ist. Aus diesem Grund wurden eine Reihe von Messungen durchgeführt, in denen untersucht wurde, ob der Lumineszenzstandard für die angedachte Aufgabe anwendbar ist. Aus den Untersuchungen zum Einfluss verschiedener Faktoren (z.B. Laserleistung oder -polarisation) auf das Messergebnis wurde ein Ablaufplan für die Messung zur Bestimmung der spektralen Sensitivität entwickelt. Mithilfe geeigneter Gegenproben wurde bestätigt, dass die Einhaltung dieses Ablaufplans zu den korrekten Ergebnissen führt. Somit konnten die für das Raman-System spezifischen Responsefunktionen aller Isotope bestimmt werden.

**5. Verifizierung der Kalibrierung mithilfe von Raman-Messungen von Gasproben** Wie unter 3. erwähnt, ist eine Verifizierung der erhaltenen Responsefunktionen notwendig, da für ihre Berechnung bisher nicht verifizierte Theoriewerte verwendet wurden. Zur Bestimmung der Responsefunktionen der nicht-tritiierten Wasserstoffisotopologe wurden Gasmischungen aus  $H_2$  und  $D_2$  in verschiedenen, genau bekannten Verhältnissen hergestellt und mithilfe eines Katalysators equilibriert, so dass HD entstand. Aus den bekannten  $H_2$ - $D_2$ -Verhältnissen vor der Equilibrierung und den jeweils gemessenen Raman-Signalstärken aller drei Isotopologe nach der Equilibrierung konnten die Responsefunktionen mithilfe eines Fits bestimmt werden. Der Vergleich der mit beiden Methoden erhaltenen Ergebnisse ergab eine Übereinstimmung innerhalb der Messunsicherheit der unter 4. diskutierten Methode. Die Unsicherheit ist  $<3,1\%$ ; somit können die Anforderungen des KATRIN-Experiments an die Messrichtigkeit der Raman-Messungen erfüllt werden.

**6. Zusammenfassung und Ausblick** Zusammenfassend kann festgehalten werden, dass sich die untersuchte Kalibriermethode, die auf einer Kombination aus theoretischen Raman-Linienintensitäten und der spektralen Sensitivität des Messsystems basiert, bewährt hat. Es wurde gezeigt, dass der Lumineszenzstandard – unter Einhaltung eines eigens entwickelten Messablaufplans – für die experimentelle Bestimmung der spektralen Sensitivität verwendet werden kann, so dass eine vergleichsweise unkompliziert durchführbare Kalibrierung des Raman-Systems für KATRIN möglich ist. Die Anforderungen an die Messrichtigkeit bei der Bestimmung der Gaszusammensetzung der KATRIN-Tritiumquelle können erfüllt werden.

Die Planungen der nächsten Schritte umfassen die Entwicklung einer Halterung für den Lumineszenzstandard sowie Langzeituntersuchungen, die eine Abschätzung ermöglichen sollen, wie häufig eine Rekalibrierung des Raman-Systems nötig ist. Außerdem soll die Erweiterung der auf genauen Gasproben basierenden Kalibriermethode auf die radioaktiven Isotopologe untersucht werden.

# Contents

<b>Zusammenfassung</b>	<b>i</b>
<b>Contents</b>	<b>v</b>
<b>List of Figures</b>	<b>ix</b>
<b>List of Tables</b>	<b>xii</b>
<b>1 Introduction</b>	<b>1</b>
<b>2 The KATRIN experiment</b>	<b>7</b>
2.1 Tritium $\beta$ -decay experiments . . . . .	7
2.1.1 The $\beta$ -decay spectrum . . . . .	7
2.1.2 Working principle of the MAC-E filter . . . . .	9
2.1.3 Results of previous tritium $\beta$ -decay experiments . . . . .	10
2.2 Overview of the KATRIN experiment . . . . .	11
2.3 KATRIN requirements . . . . .	12
2.3.1 General requirements . . . . .	13
2.3.2 WGTS requirements . . . . .	13
2.3.3 Isotopic purity . . . . .	14
<b>3 Quantitative Raman spectroscopy for KATRIN</b>	<b>17</b>
3.1 The Raman effect . . . . .	17
3.1.1 Basic principle of Raman scattering . . . . .	17
3.1.2 Laser Raman spectroscopy . . . . .	19
3.1.3 Raman intensities . . . . .	21
3.1.4 Quantitative analysis of Raman spectra . . . . .	23
3.2 Setup of the KATRIN laser Raman system . . . . .	25
3.3 Raman intensity calibration methods . . . . .	29
3.3.1 Accurately known gas samples . . . . .	29
3.3.2 Theoretical intensities and spectral sensitivity . . . . .	32
3.3.3 Conclusions . . . . .	33

<b>4</b>	<b>Calibration based on theoretical Raman signal amplitudes</b>	<b>35</b>
4.1	Calibration principle . . . . .	35
4.2	Theoretical Raman intensities of hydrogen isotopologues . . . . .	37
4.3	Methods for the spectral sensitivity determination . . . . .	38
4.3.1	Necessity of an experimental approach . . . . .	38
4.3.2	Principle behind the experimental determination of the spectral sensitivity . . . . .	39
4.3.3	Calibration light source requirements . . . . .	39
4.3.4	Overview of possible calibration light sources . . . . .	41
4.4	Use of a luminescence standard as calibration light source . . . . .	45
4.4.1	Description of the luminescence standard SRM 2242 . . . . .	45
4.4.2	Advantages of the use of SRM 2242 for LARA . . . . .	46
4.4.3	Challenges connected to the use of SRM 2242 for LARA . . . . .	48
4.5	Investigation of the applicability of SRM 2242 to KATRIN . . . . .	52
4.5.1	Influence of the incident position of the laser beam on the spectral shape . . . . .	53
4.5.2	Influence of polarization on the spectral shape . . . . .	58
4.5.3	Influence of the Raman cell window on the spectral shape . . . . .	64
4.5.4	Difference between double-pass and single-pass mode . . . . .	66
4.5.5	Influence of temperature and laser power on the spectral shape . . . . .	69
4.5.6	Conclusions for the measurement procedure . . . . .	71
4.6	Validity cross-check of the spectral sensitivity determination . . . . .	72
4.7	Summary and conclusions . . . . .	76
<b>5</b>	<b>Verification of the calibration via Raman measurements of gas samples</b>	<b>77</b>
5.1	Motivation of measurements with well-known H-D-mixtures . . . . .	78
5.2	Measurement principle . . . . .	78
5.3	Setup of the Hydrogen Deuterium Equilibration loop . . . . .	80
5.4	Measurement procedure . . . . .	82
5.5	Analysis and discussion . . . . .	84
5.5.1	Analysis procedure . . . . .	84
5.5.2	Results and discussion . . . . .	86
5.6	Comparison of the measurement results . . . . .	90
5.7	Conclusion . . . . .	91
<b>6</b>	<b>Summary and outlook</b>	<b>93</b>

<i>CONTENTS</i>	vii
<b>A Terminology of ‘accuracy’, ‘precision’ and ‘trueness’</b>	<b>97</b>
<b>B Excited states of diatomic molecules</b>	<b>99</b>
<b>C Determination of the spectral sensitivity by using a stabilized, calibrated LED light source</b>	<b>103</b>
C.1 Stabilization and calibration of the LED light source . . . . .	103
C.1.1 Basic principle . . . . .	103
C.1.2 The LED source . . . . .	103
C.1.3 Calibration of the LED source . . . . .	104
C.2 Replication of the Raman scattering region . . . . .	107
<b>D Supplements to the HYDE measurements</b>	<b>111</b>
D.1 Measurement procedure of the HYDE measurements . . . . .	111
D.2 Correction of the $Q_1$ -branch of HD . . . . .	115
D.3 Determination of Raman signal amplitudes using the <i>ShapeFit</i> method . . .	116
D.4 Correlation of the fit parameters . . . . .	117
D.5 All fit results of the HYDE measurements . . . . .	118
<b>Bibliography</b>	<b>119</b>



# List of Figures

1.1	Neutrino mass scenarios . . . . .	2
1.2	Contribution of the neutrino density to the total energy density of the universe . . . . .	3
2.1	Electron spectrum of tritium $\beta$ -decay . . . . .	8
2.2	Principle of the MAC-E-Filter . . . . .	9
2.3	Setup of the KATRIN experiment . . . . .	11
2.4	Simplified flow diagram of the inner tritium loop . . . . .	12
2.5	Dependence of the systematic shift of $m_\nu^2$ on the calibration error of the composition monitoring system . . . . .	16
3.1	Different types of scattering of light in the quantum mechanical picture . . . . .	18
3.2	Schematic Raman spectrum of a diatomic molecule . . . . .	20
3.3	Raman spectrum of a mixture of H <sub>2</sub> , HD and D <sub>2</sub> gas for an excitation wavelength of 532 nm . . . . .	20
3.4	Measurement setup for Raman spectroscopy (schematic) . . . . .	21
3.5	Typical Raman spectrum of a gas mixture containing all hydrogen isotopologues. . . . .	24
3.6	Schematic sketch of the LARA 1 setup . . . . .	25
3.7	Raman cell . . . . .	27
3.8	Wavelength-dependence of edge filter transmission and spectrometer/CCD quantum efficiency . . . . .	30
4.1	Influence of the fiber position on measured relative Raman signal amplitudes of H <sub>2</sub> , HD and D <sub>2</sub> . . . . .	40
4.2	Examples of external calibration light sources . . . . .	43
4.3	Suggested setup for the spectral sensitivity determination using black body radiation . . . . .	44
4.4	The luminescence standard SRM 2242 . . . . .	45
4.5	Certified polynomial and 95% confidence curves for SRM 2242 . . . . .	46
4.6	Replication of the scattering region by SRM 2242. . . . .	47

4.7	Coverage of the $Q_1$ -branches by the SRM 2242 certification . . . . .	49
4.8	Relative uncertainty of the SRM luminescence spectrum, extrapolated to the uncertified range . . . . .	49
4.9	Differences between the Raman setups (schematic) . . . . .	50
4.10	Different incident positions of the laser beam on SRM 2242 . . . . .	54
4.11	Measured spectra for all incident laser positions and angles . . . . .	55
4.12	Comparison of the spectral shapes for all incident laser positions and angles . . . . .	55
4.13	Maximum relative intensity difference between the spectra obtained for parallel alignment and the ones obtained for incidence on the back surface . . . . .	57
4.14	Relative intensity differences within the respective measurement sets of parallel alignment and incidence on the back . . . . .	58
4.15	Comparison of spectral shapes for different polarizations . . . . .	59
4.16	Influence of the laser polarization on the measured spectra . . . . .	60
4.17	Radiation pattern of an oscillating dipole . . . . .	61
4.18	Differences in the observed radiation for vertical and horizontal laser polarization . . . . .	62
4.19	Measurement setup . . . . .	65
4.20	Difference in the spectral shape for measurements with and without Raman window . . . . .	65
4.21	Use of the luminescence standard in double-pass mode . . . . .	67
4.22	Difference in spectral shape between double- and single-pass mode . . . . .	67
4.23	Difference to parallel alignment . . . . .	68
4.24	Measurement of the luminescence standard temperature . . . . .	70
4.25	Shift of the luminescence spectrum with laser power . . . . .	71
4.26	Spectral sensitivity of two different LARA systems . . . . .	73
4.27	Measurement of the spectrum of a white light LED at the LARA 1 system . . . . .	74
4.28	Measured and corrected white light LED spectra . . . . .	74
4.29	Uncorrected spectrum of the same gas-filled cell measured at two different LARA systems . . . . .	75
5.1	Setup of the HYDE loop (schematic) . . . . .	81
5.2	HYDE data and fit curves . . . . .	87
5.3	Fit results of the relative response functions . . . . .	88
5.4	Comparison of fit results and calculated values of the equilibrium constant $K(T)$ . . . . .	88
A.1	Precision, trueness and accuracy of a measurement . . . . .	98
B.1	Models of excited diatomic molecules . . . . .	99

B.2	Potential curves and energy levels of oscillating systems . . . . .	102
C.1	Coverage of the $Q_1$ -branches of all hydrogen isotopologues by three LEDs .	104
C.2	Schematic sketch of the LED source (not to scale) . . . . .	105
C.3	Schematic sketch of the calibration setup using filters (top view) . . . . .	106
C.4	Calibration setup using a prism (top view) . . . . .	107
C.5	Cylindrical lens . . . . .	109
C.6	Replication of the Raman scattering region by using a movable mirror . . .	109
D.1	Overlap of hydrogen Raman peaks . . . . .	115
D.2	Raman spectra of pure $H_2$ , HD and $D_2$ gas . . . . .	117



# List of Tables

3.1	Classification of branches in the Raman spectrum according to selection rules	19
3.2	Overview of the components of the different LARA systems . . . . .	26
4.1	Comparison of commercially available calibration light sources . . . . .	42
4.2	Comparison of the results obtained with the two LARA systems . . . . .	75
4.3	Raman response functions obtained by the calibration method based on theoretical Raman signal amplitudes . . . . .	76
5.1	Overview of the measurements performed with the HYDE loop . . . . .	82
5.2	Settings of the Raman system during HYDE measurements . . . . .	84
5.3	Measured catalyst temperatures and corresponding reaction constants . . .	86
5.4	Fit results of the relative response functions for 25 °C and ‘binary fixed’ scenario . . . . .	91
5.5	Comparison of the results of the two calibration methods . . . . .	91
D.1	Results of all fit scenarios and at all catalyst temperature setpoints . . . . .	118



# Chapter 1

## Introduction

This thesis focuses on calibration methods for quantitative Raman spectroscopy of hydrogen isotopologues, which is of high relevance for the Karlsruhe Tritium Neutrino Experiment (KATRIN). KATRIN aims to measure the electron antineutrino mass with a sensitivity of  $200 \text{ meV}^1$  (90% C.L.), thus addressing a major issue in the fields of particle physics as well as astroparticle physics and cosmology. This chapter presents a brief overview of neutrinos and the relevance of a neutrino mass determination, before the contribution of the thesis to this field of research is outlined.

**A short history of neutrinos** The neutrino was postulated by W. Pauli in 1930 [Pau30] in order to explain the continuous electron spectrum observed in  $\beta$  decay processes. By assuming the emission of an additional particle in the apparent two-body decay, neutral with spin  $\frac{1}{2}$ , the observation could be explained in accordance with conservation of energy and momentum:

$$n \rightarrow p + e^- + \bar{\nu}_e . \quad (1.1)$$

However, with the neutrino interacting neither strongly nor electromagnetically, it was not until 1956 that it was finally experimentally discovered by C. L. Cowan and F. Reines [Rei56]. Over fifty years later, the elusive neutrino is still subject to a multitude of experimental as well as theoretical investigations; concerning its mass, only an upper limit could be determined up to the year 2012. According to the Particle Data Group, the current upper limit is given by [PDG12]

$$m_\nu < 2 \text{ eV} \quad (95\% \text{ C.L.}) . \quad (1.2)$$

While the three neutrino generations  $\nu_e$ ,  $\nu_\mu$  and  $\nu_\tau$  are regarded as massless particles in the standard model of particle physics [Sch97], the observation of oscillations between the flavors – in experiments with solar and atmospheric neutrinos as well as neutrinos from reactors and accelerators [Kaj12, Ant12, Con12, Har12, Las12] – proves that neutrinos have a non-vanishing mass. A further investigation of this fundamental particle property is the task of next generation neutrino mass experiments like KATRIN.

---

<sup>1</sup>Here and in the following, the convention  $c=1$  is used.

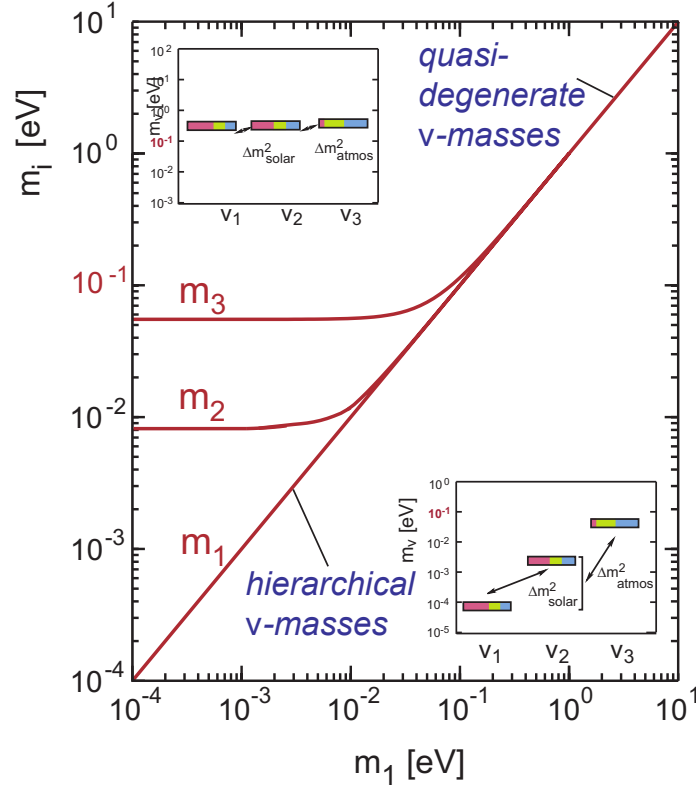


**Figure 1.1: Neutrino mass scenarios.** The values of the three neutrino mass eigenstates  $m_1$ ,  $m_2$  and  $m_3$  are shown as a function of the lightest eigenstate  $m_1$ . In the hierarchical scenario,  $m_1$  is small compared to the differences of the squared masses  $\Delta_{ij}m^2 = |m_j^2 - m_i^2|$ , so that the mass eigenstates differ significantly. In the quasi-degenerate scenarios, the values of all mass eigenstates are in a similar range due to the small mass splitting compared to the absolute values. (From [KAT05].)

**Motivation of neutrino mass experiments** The determination of the neutrinos mass is of great importance for current issues in particle physics as well as cosmology:

- **Particle physics:** Many theories exploring the origin of neutrino masses are based on the so-called see-saw effect [Bar80, Yan80, Moh80]. There are two types of see-saw mechanisms proposed, which predict different neutrino mass scenarios: the first mechanism prefers a hierarchical ( $m_1 \ll m_2 \ll m_3$ ), the second a quasi-degenerate pattern of neutrino masses ( $m_1 \approx m_2 \approx m_3$ ). Both scenarios are illustrated in figure 1.1. A determination of the neutrino masses is necessary to discriminate between the two scenarios and thus gain information about the actual mechanism of neutrino mass generation. This is of high interest with respect to a better understanding of the origin of mass.
- **Cosmology:** A large cosmological neutrino background is left over from the Big Bang. Being relativistic at the time of decoupling from matter, these abundant amounts of neutrinos played a certain role in the structure formation of the universe as so-called neutrino hot dark matter ( $\nu$ HDM); they could freely stream out of density fluctuations and thus slow down their growth [Han04]. The overall influence

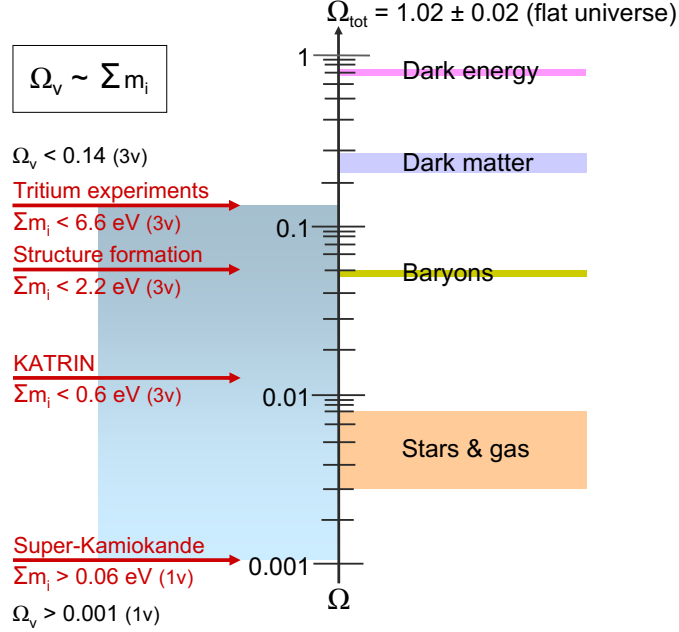


**Figure 1.2: Contribution of the neutrino density to the total energy density of the universe.** The experimentally allowed contribution  $\Omega_\nu$  is compared to the contributions from dark energy, dark matter and baryons. The lower bound results was obtained by the analysis of the oscillation of atmospheric neutrinos, the upper one results from tritium beta decay experiments and studies of structure formation. The upper bound which can be achieved by the KATRIN experiment is indicated as well. Note that the contribution by stars and gas is part of the total baryonic contribution, and the one by neutrinos is part of the dark matter contribution. (Modified from [Eic09], according to [KAT05].)

of  $\nu$ HDM on the evolution of large-scale structures depends on the contribution of the neutrino density  $\Omega_\nu$  to the total energy density  $\Omega_{\text{tot}}$  in the universe. This contribution increases with increasing neutrino masses [Han04]:

$$\Omega_\nu h^2 = \sum_{i=1}^3 m_i / 93 \text{ eV} . \quad (1.3)$$

Here,  $h$  is the Hubble constant and  $m_i$  are the neutrino mass eigenstates.

As shown in figure 1.2, an improved and model-independent neutrino mass measurement by KATRIN will either significantly constrain or even fix the contribution  $\Omega_\nu$ , thus leading to a much better understanding of the role of  $\nu$ HDM in the structure formation of the universe.

**Determination of the absolute neutrino mass scale** As mentioned above, neutrino oscillation experiments provide evidence for massive neutrinos: oscillations can only occur if the flavor states  $\nu_e$ ,  $\nu_\mu$  and  $\nu_\tau$  of the three neutrino generations are mixings of three different neutrino mass states  $\nu_1$ ,  $\nu_2$  and  $\nu_3$  [Ott08]. However, the results from such oscillations experiment can only provide information about mass differences, but not about the absolute mass scale.

The latter information can be obtained by different approaches. Indirect methods are:

- **Determination of neutrino masses from cosmology.** The connection between neutrino masses and the structure formation in the universe mentioned above can of course be used for investigations in both directions: while a better estimation of neutrino masses can improve the understanding of structure formation, studies of this formation can also provide information about the sum of the neutrino masses. Structure formation can be studied by investigating the fluctuations in the cosmic microwave background as well as by galaxy surveys (see e.g. [Kom11, Aih11]). The current upper limits on the sum of the neutrino masses obtained this way are of the range of  $\sum m_i < 0.5 \text{ eV}$  [Aba11]; however, these results are to some extent dependent on the underlying model and analysis procedure [Les12].
- **Determination of the effective neutrino mass from neutrinoless double  $\beta$ -decay.** Another model-dependent method for the determination of the neutrino mass is the investigation of the neutrinoless double  $\beta$ -decay ( $0\nu\beta\beta$ ). It can only be observed if the neutrino is a Majorana particle, i.e. its own antiparticle [Sch97]. In this case, a simultaneous decay of two neutrons in the same nucleus can occur in such a way that the neutrino emitted at one vertex as a right-handed antineutrino  $\bar{\nu}_R$  is absorbed as a left-handed neutrino  $\nu_L$  at the other vertex. This leads to the following effectively neutrinoless decay pattern of a nucleus  $N$  with mass number  $A$  and charge  $Z$ :

$${}^A_Z N \rightarrow {}^A_{Z+2} N' + 2e^- . \quad (1.4)$$

For such a  $0\nu\beta\beta$ -decay to take place, a spin-flip of the neutrino is required. For this reason, the probability of this process and thus the decay rate  $\Gamma_{0\nu\beta\beta}$  depends on the neutrino mass [Giu12]:

$$\Gamma_{0\nu\beta\beta} \propto m_{ee}^2 = \left| \sum_{i=1}^3 U_{ei}^2 m_i \right|^2 . \quad (1.5)$$

The so-called effective neutrino mass  $m_{ee}$  is defined as the coherent sum of the  $m(\nu_i)$  components of the  $0\nu\beta\beta$ -decay [Dre12];  $U_{ei}$  are complex elements of the neutrino mixing matrix. However, the calculated values of these elements differ depending on the calculation method used [Giu12].

The observation of neutrinoless double  $\beta$  decay at  $m_{ee} \approx 0.3 \text{ eV}$  was claimed by parts of the Heidelberg-Moscow collaboration [Kla06]. Recent limits are provided e.g. by the EXO-200 experiment with  $m_{ee} < 0.14 \text{ eV} - 0.38 \text{ eV}$ , depending on the matrix element calculation [Aug12].

Direct measurements of the neutrino mass are based on the relativistic energy momentum relationship

$$E^2 = p^2 c^2 + m^2 c^4 \quad (1.6)$$

and the conservation of energy and momentum. There are two types of these kinematic measurements:

- **Time-of-flight measurements.** The time-of-flight of a neutrino with velocity  $v_\nu$ , which starts at a time  $t_0$  from a certain point (source) and is detected at a time  $t$  in a distance  $L$  to the source, is given by [Sch97]

$$T_\nu = t - t_0 = \frac{L}{v_\nu} = \frac{L}{c} \cdot \frac{E_\nu}{\sqrt{E_\nu^2 - m_\nu^2 c^4}} \quad (1.7)$$

and is thus dependent on the neutrino mass.  $E_\nu$  is the total neutrino energy according to eq. (1.6).

In practice, very long baselines  $L$  are required to obtain evaluable data; supernova explosions can act as sufficiently strong neutrino sources [Dre12]. Since the time of emission  $t_0$  is not known in this case, differences in the time-of-flight of neutrinos with different energies are measured:

$$\Delta t = \Delta t_0 + \Delta T_\nu(L, E_{\nu,1}, E_{\nu,2}, m_\nu) . \quad (1.8)$$

In order to reach a sensitivity for  $m_\nu$  in the few-eV range, the difference in the time of emission  $\Delta t_0$  has to be assumed based on models describing the time evolution of the supernova neutrino burst. At this point, the mass determination becomes model-dependent again. Furthermore, nearby supernova explosions are very rare events, which makes this method less favorable than laboratory neutrino mass experiments. Since the first neutrino detectors were built, there was only one suitable supernova explosion; a detailed analysis of this supernova 1987A yields an upper limit on the neutrino mass of 5.7 eV [Lor02].

- **Kinematics of weak decays.** The currently most sensitive model-independent method for a direct neutrino mass measurement is the investigation of weak decays [Dre12]. The method makes use of the fact that an energy equivalent to the neutrino rest mass is needed for the production of a neutrino in  $\beta$ -decays (see eq. 1.1). Thus, the energy spectrum of the emitted electron is dependent on the neutrino mass: the larger this mass, the smaller the amount of energy set free in the decay as kinetic energy of the decay products, and vice versa. This makes an observation of the neutrino itself unnecessary. The investigation of the  $\beta$ -electron spectrum provided the currently most stringent limit on the electron antineutrino mass [PDG12]:

$$m_{\nu_e} < 2 \text{ eV} \quad (95\% \text{ C.L.}) . \quad (1.9)$$

Based on this last-mentioned direct method, the next generation neutrino mass experiment KATRIN will measure the neutrino mass with a sensitivity of 200 meV (90% C.L.) by high-precision spectroscopy of the decay electrons from tritium  $\beta$ -decay [KAT05].

The projected improvement of the present upper limit by one order of magnitude can only be achieved if systematic uncertainties are minimized in all areas of the experiment. Regarding the tritium source, an important parameter influencing the measured  $\beta$ -spectrum is the isotopic composition of the source gas: it has to be monitored continuously with a precision of at least 0.1% [Bab12] and a calibration accuracy of at least 10% [Sch12d]. The method employed for this purpose is laser Raman spectroscopy.

Within the scope of this thesis, a method for the calibration of the KATRIN laser Raman system was examined. It is based on the determination of the system's spectral sensitivity.

Investigations of the practical applicability of this method to KATRIN were carried out, which showed the eligibility of this approach for the task at hand, and from which operating parameters for the calibration procedure were derived. Furthermore, the calibration results were successfully verified by a second, independent calibration method.

The thesis is structured in the following way: First, a brief introduction to the KATRIN experiment is given, based on which the motivation of this thesis is explained. In section 3, the fundamentals of quantitative Raman spectroscopy are explained. The basic principle of the examined calibration method as well as the investigations of its applicability are presented in section 4, with the focus being set on the determination of the spectral sensitivity. In section 5, the verification of the calibration results by an alternative calibration method is discussed. The thesis concludes with a summary of the results and an outlook on possible future works on this topic.

## Chapter 2

# The KATRIN experiment

This chapter gives an introduction to the KATRIN experiment. After a brief description of the measurement principle of  $\beta$ -decay experiments in section 2.1, an overview of the experimental configuration of KATRIN is given in section 2.2. Section 2.3 discusses the requirements which have to be fulfilled in order to reach the design sensitivity. The focus is set on the requirements to the isotopic purity of the KATRIN tritium source, which leads to the motivation of this thesis.

### 2.1 Tritium $\beta$ -decay experiments

As motivated in the introductory chapter, a direct neutrino mass measurement with high sensitivity is possible using the kinematics of  $\beta$ -decays. The KATRIN experiment will push the precision of  $\beta$ -spectroscopy to the present technological limits. The principles to obtain high resolution  $\beta$ -spectroscopy are outlined in the following.

This section is mainly based on [KAT05] and [Dre12].

#### 2.1.1 The $\beta$ -decay spectrum

The measurement method is based on the dependence of the  $\beta$ -electron spectrum on the neutrino mass. The spectrum is described by the following expression:

$$\begin{aligned} \frac{d^2N}{dt dE} = & C \cdot |M_{\text{nucl}}^2| \cdot F(E, Z') \cdot (E + m_e c^2) \cdot \sqrt{(E + m_e c^2)^2 - m_e^2 c^4} \\ & \cdot \sum_{i,j} (|U_{ei}^2| \cdot P_j \cdot (E - E_0 - V_j) \cdot \sqrt{(E - E_0 - V_j)^2 - m_i^2 c^4} \\ & \cdot \Theta(E - E_0 - V_j - m_i c^2)) . \end{aligned} \quad (2.1)$$

In this expression,  $C$  is a constant factor which includes the Fermi constant and the Cabbibo angle. The nuclear transition matrix element  $|M_{\text{nucl}}^2|$  is characteristic for the  $\beta$ -decaying nucleus, just as the Fermi function  $F(E, Z')$ , which takes into account the Coulomb interaction of the emitted electron with the daughter nucleus of nuclear charge  $Z'$ .  $E$  and  $m_e$  are the  $\beta$ -electron's kinetic energy and mass. The endpoint energy  $E_0$  is

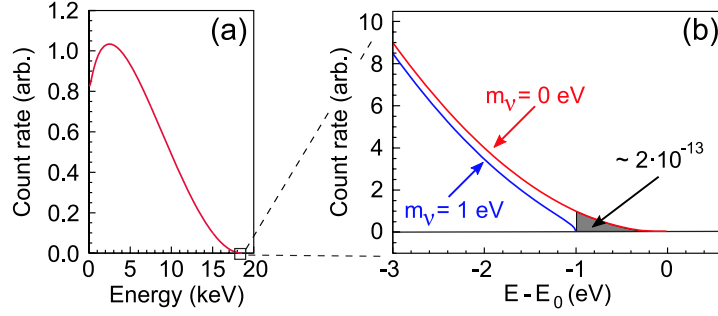


**Figure 2.1: Electron spectrum of tritium  $\beta$ -decay.** (a) Full tritium  $\beta$ -spectrum. The endpoint energy is 18.6 eV. (b) Zoom into the region near the kinematic endpoint. The plot shows the simulated spectra for  $m_\nu=0$  eV and  $m_\nu=1$  eV in order to demonstrate the effect of the neutrino mass on the shape of the curve. In the case of tritium, a fraction of only  $2 \cdot 10^{-13}$  of all  $\beta$ -decays is found in the region 1 eV below the endpoint (gray-shaded area). (From [Sch09], according to [KAT05].)

defined as the maximal kinetic energy of the electron for the case a vanishing neutrino mass. Energy conservation is ensured by the  $\Theta$ -function.

There are several possible final states in which the decaying system can end up; the electron energy spectrum represents effectively a weighted sum over their individual spectra. On the one hand, it has to be summed over all neutrino mass eigenstates  $m_i$ , the probabilities of which are given by the neutrino mixing matrix  $U_{ei}$ . Additionally, for the decay of an atom or molecule, the final states of the daughter system have to be taken into account, where the probabilities are given by  $P_j$  and the excitation energies by  $V_j$ . In case of decaying molecules, electronic as well as rotational and vibrational excitations can occur, which shift the endpoint energy to lower values.

A measurable influence of the neutrino mass on the  $\beta$ -spectrum can only be observed in the energy region close to the endpoint  $E_0$ , as illustrated in figure 2.1. Since the count rate is very low in this region, the  $\beta$ -emitter used should provide a high activity as well as a low endpoint energy: the lower the endpoint energy, the larger the relative fraction of decay events in the region near the endpoint. Experimentally, a high relative energy resolution  $\frac{\Delta E}{E}$  can be more easily achieved at lower endpoint energies. For these reasons, many  $\beta$ -decay experiments for the neutrino mass determination, including KATRIN, have been using tritium as  $\beta$ -emitter due to its advantageous properties [Dre12, KAT05]:

- a low endpoint energy of 18.6 keV, which is the second lowest endpoint energy of all  $\beta$ -emitters;
- a comparatively short half-life of 12.3 y;
- a simple electronic structure, which makes calculations of corrections e.g. due to interactions between  $\beta$ -decay electrons and tritium source gas relatively simple;
- a super-allowed nuclear transition, so that the matrix elements  $|M_{\text{nuc}}^2|$  are independent of the electron energy.

### 2.1.2 Working principle of the MAC-E filter

In order to resolve the shape of the  $\beta$ -spectrum near its endpoint, a high energy resolution as well as a large acceptance and low background is required apart from the large source strength mentioned above. These requirements are fulfilled by the type of spectrometer used in the KATRIN experiment: a so-called MAC-E-Filter (Magnetic Adiabatic Collimation with an Electrostatic Filter).

The main features of the MAC-E-filter are explained in figure 2.2. As implied by its name, this spectrometer type uses the principle of magnetic adiabatic collimation to parallelize the emitted electrons, which are filtered by their kinetic energy by a retarding electrostatic potential. The collimation is necessary since the retarding potential acts only on the component of motion along the electric field. A variation of the retarding potential of this

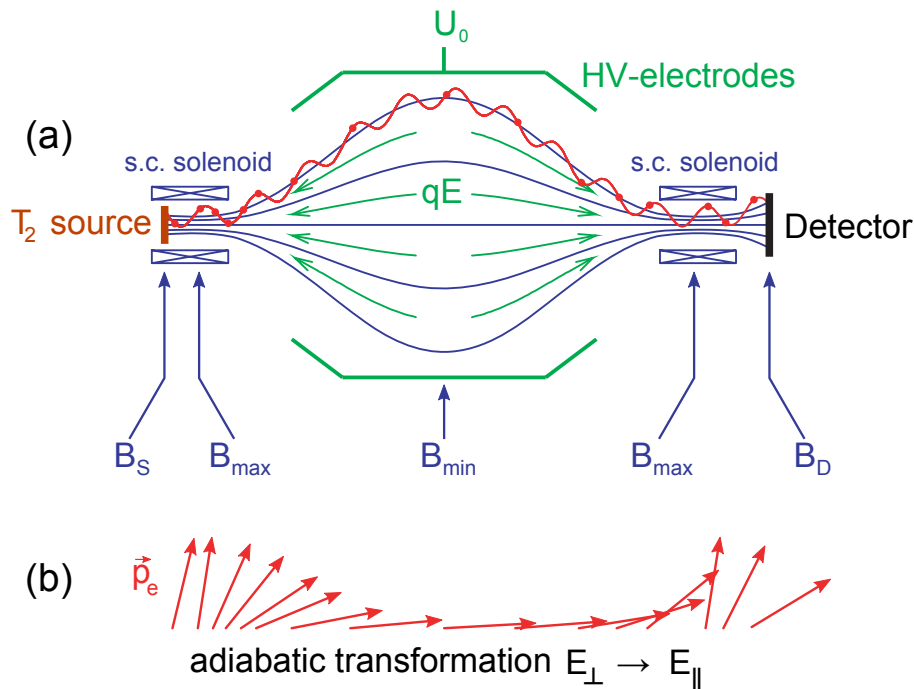


**Figure 2.2: Principle of the MAC-E-Filter.** (a) Experimental setup.  $\beta$ -decay electrons, which are emitted in the tritium source, are guided magnetically to the detector. The guiding field is produced by two superconducting solenoids; the source is located in one of them. This setup allows to obtain an accepted solid angle of nearly  $2\pi$ . The electrons follow the magnetic field lines in a cyclotron motion to the spectrometer, where the magnetic field decreases smoothly by several orders of magnitude towards the center. This slow variation keeps the magnetic orbital moment  $\mu = E_{\perp}/B$  of the electron invariant, so that almost all cyclotron energy  $E_{\perp}$  is transformed into longitudinal motion. The adiabatic transformation of the momentum vector is illustrated in (b). The parallel beam of electrons is filtered by the retarding potential  $U_0$ , which is created by a set of cylindrical electrodes. The electrons with enough energy to pass the barrier are re-accelerated while being guided to the detector. (From [Sch09], according to [KAT05].)

high-pass energy filter allows the measurement of the integrated  $\beta$ -spectrum

$$\int_{E=eU}^{E_0} \frac{d^2 N}{dt dE} dE . \quad (2.2)$$

The ratio between the minimum and the maximum value of the magnetic guiding field (cf. figure 2.2) defines the relative sharpness of the filter:

$$\frac{\Delta E}{E} = \frac{B_{\min}}{B_{\max}} . \quad (2.3)$$

The energy resolution of the KATRIN experiment is  $\Delta E = 0.93$  eV.

### 2.1.3 Results of previous tritium $\beta$ -decay experiments

Neutrino mass experiments based on tritium  $\beta$ -decay have been performed earlier, resulting in upper limits on the neutrino mass. Compared to several experiments using magnetic spectrometers, the introduction of the MAC-E-Filter in the Troitsk and Mainz neutrino mass experiments led to an significant improvement in sensitivity.

The Mainz experiment made use of a quenched-condensed tritium source and a spectrometer of 1 m diameter to obtain a result of [Kra05]

$$m_\nu^2 = -0.6 \pm 2.2_{\text{stat}} \pm 2.1_{\text{syst}} \text{ eV}^2 , \quad (2.4)$$

which corresponds to an upper limit of the neutrino mass of

$$m_\nu < 2.3 \text{ eV} \quad (95\% \text{ C.L.}) . \quad (2.5)$$

The Troitsk experiment used a spectrometer of a similar size (1.5 m in diameter) while refining the concept of a windowless gaseous tritium source pioneered earlier in the Los Alamos experiment [Rob91]. In 2011 the results of a reanalysis of the Troitsk data taken between 1997 and 2002 were published [Ase11]:

$$m_\nu^2 = -0.67 \pm 1.89_{\text{stat}} \pm 1.68_{\text{syst}} \text{ eV}^2 . \quad (2.6)$$

Using the Feldman and Cousins approach [Fel98] to estimate the upper limit on the neutrino mass, this value corresponds to an upper limit of

$$m_\nu < 2.05 \text{ eV} \quad (95\% \text{ C.L.}) . \quad (2.7)$$

The same data are used for an evaluation of the Particle Data Group [PDG12], which results in an upper mass limit of

$$m_\nu < 2 \text{ eV} \quad (95\% \text{ C.L.}) . \quad (2.8)$$

The two experiments provide the best sensitivity reached in direct neutrino mass experiments until today. However, since a further reduction of the systematic errors of these setups is not feasible, significantly better sensitivities could not be reached even if the statistical error was further reduced by more data-taking. This explains the necessity for the next generation neutrino mass experiment KATRIN.

## 2.2 Overview of the KATRIN experiment

The experimental configuration of the KATRIN experiment is shown in figure 2.3. The main components are briefly described in the following, based on the KATRIN design report [KAT05]. A specific focus is set on the tritium source, which is of particular relevance for this thesis.

**The rear section** monitors key source parameters such as the source activity.

**The Windowless Gaseous Tritium Source (WGTS)** is the high luminosity  $\beta$ -decay electron source [Bab12]. Molecular tritium gas is continuously injected into the source tube and pumped off at both ends of the 10 m long source tube, producing  $10^{11}$  electrons per second by  $\beta$ -decay. Superconducting solenoids surrounding the beam tube produce a magnetic field of 3.6 T, by which the  $\beta$ -electrons are guided adiabatically towards the transport section. The gas composition of the tritium source is continuously monitored by a laser Raman system in the tritium loop, as shown in the flow diagram in figure 2.4. The requirements which the WGTS has to fulfill with respect to the targeted KATRIN sensitivity are discussed in section 2.3.1.

**The transport section** has the task to transport the  $\beta$ -decay electrons adiabatically from the source to the spectrometer section, while at the same time reducing the tritium flow significantly. A suppression of the tritium flow by a factor of  $> 10^{14}$  [Kos12] will be achieved by a combination of an active differential and a passive cryogenic pumping section. The large reduction factor is necessary to limit the background due to tritium decays in the main spectrometer to a maximum value of  $10^{-3}$  cps.

**The electrostatic spectrometers** are of MAC-E-Filter type. The pre-spectrometer allows the option to pre-filter and reject the low-energy part of the tritium  $\beta$ -decay spectrum with an energy  $\leq 18.3$  keV, from which no information about the neutrino mass is gained. By this means, background due to ionization of residual gas molecules in the main spectrometer can be minimized. The main spectrometer analyses the remaining electrons, i.e. the part of the energy spectrum close to the endpoint, with an energy resolution of 0.93 eV. Both spectrometers will operate under ultra-high vacuum (UHV) conditions.

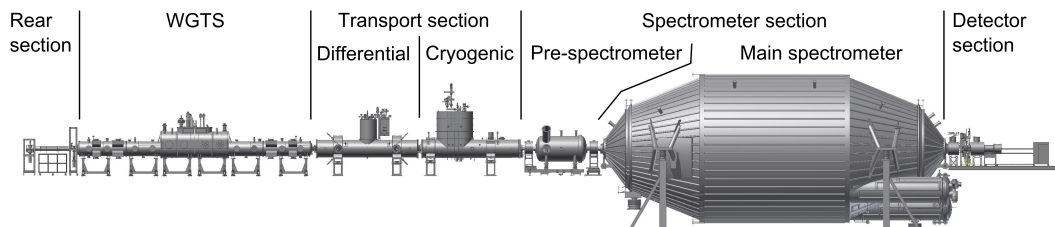


**Figure 2.3: Setup of the KATRIN experiment.** The total setup is 70 m long. The main spectrometer has a length of 24 m and a diameter of 10 m. Not shown here is the system of air coils which surrounds the main spectrometer. (Modified from [Fis10].)

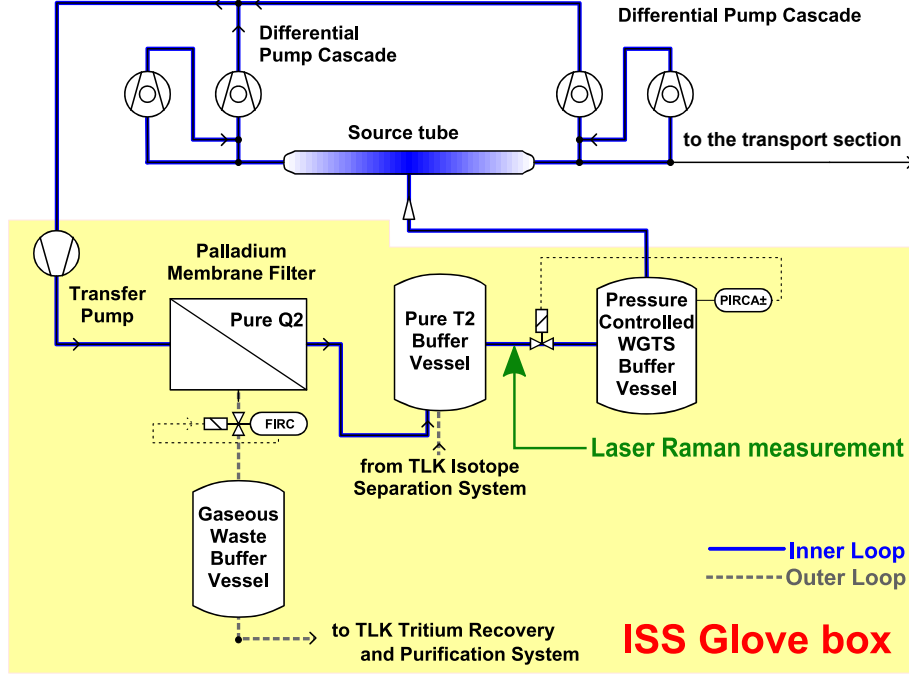


**Figure 2.4: Simplified flow diagram of the inner tritium loop.** Tritium gas is injected into the KATRIN source tube from a pressure and temperature controlled buffer vessel, which provides for a constant injection rate. The gas is pumped off by turbomolecular pumps at both ends of the source tube and cleaned by a filter consisting of a palladium membrane which is only permeable by hydrogen isotopologues. Via a second buffer vessel, into which fresh tritium batches can be injected if necessary, the gas is fed back into the WGTS buffer vessel at a pressure of approximately 130 mbar. The isotopic composition of the tritium gas is continuously monitored by the laser Raman system installed between both vessels. (From [Stu10a].)

**The detector** counts the transmitted electrons. It is a segmented Si-PIN diode array with a detection efficiency of  $> 90\%$  for electrons close to  $E_0$  [Dre12].

All tritium bearing components (rear section, WGTS and transport section) are located in the Tritium Laboratory Karlsruhe (TLK). It provides both the extensive infrastructure and the long-standing expertise needed for this challenging project with a daily tritium throughput of 40 g (see [Bor11] and references therein).

## 2.3 KATRIN requirements

As discussed at the end of section 2.1.3, the next generation neutrino mass experiment KATRIN has been designed to reach significantly better sensitivities than previous experiments by reducing systematic and statistical uncertainties. According to the KATRIN design report, the statistical uncertainty of  $m_\nu^2$  for a measurement time of three years will be  $\sigma_{\text{stat}} = 1.8 \cdot 10^{-2} \text{ eV}^2$ . Together with the anticipated systematic uncertainty of  $\sigma_{\text{sys,tot}} \leq 1.7 \cdot 10^{-2} \text{ eV}^2$ , this sums up quadratically to a total uncertainty of

$$\sigma_{\text{tot}} \approx 2.5 \cdot 10^{-2} \text{ eV}^2 . \quad (2.9)$$

This leads to a sensitivity level  $L(90\% \text{ C.L.}) = \sqrt{1.64 \cdot \sigma_{\text{tot}}}$  of

$$m_\nu = 200 \text{ meV} \quad (90\% \text{ C.L.}) . \quad (2.10)$$

This corresponds to a  $5\sigma$  discovery potential for a neutrino mass of

$$m_\nu = 350 \text{ meV} . \quad (2.11)$$

Compared to previous tritium  $\beta$ -decay experiments, the sensitivity will be improved by one order of magnitude. Thus, KATRIN will be able to probe a neutrino mass range of particular relevance for cosmology and particle physics [KAT05]. However, since the actual observable is  $m_\nu^2$ , an improvement in sensitivity by a factor of 10 requires an improvement in uncertainties by a factor of 100. In the following, the implications for KATRIN are discussed with a focus on the isotopic purity of the WGTS.

### 2.3.1 General requirements

In order to reach the projected sensitivity, several key requirements have to be fulfilled. Of particular importance are [KAT05]:

- A high signal rate in the endpoint region. Compared to the Troitsk and Mainz experiments, the signal rate has to be increased by a factor of 100.
- A good energy resolution of  $\Delta E < 1 \text{ eV}$ .
- A low background rate of  $< 10^{-2}$  cps in the endpoint region.
- A systematic uncertainty  $\sigma_{\text{syst,tot}}$  in the same order of magnitude as the statistical uncertainty  $\sigma_{\text{stat}} = 1.8 \cdot 10^{-2} \text{ eV}^2$  for the observable  $m_\nu^2$ . This corresponds to a maximum systematic uncertainty budget of

$$\Delta m_\nu^2 < 7.5 \cdot 10^{-3} \text{ eV}^2 \quad (2.12)$$

for each of five individual systematic uncertainties identified for KATRIN.

### 2.3.2 WGTS requirements

The signal rate  $S$  is proportional to the tritium content of the source:

$$S \propto \rho d \cdot \epsilon_T . \quad (2.13)$$

with the (effective) column density  $\rho d$  and the isotopic purity or tritium purity  $\epsilon_T$ . The parameter  $\epsilon_T$  is defined as the number of tritium nuclei normalized to the total number of nuclei in the source gas [Höt12]. Thus, the isotopic purity has to be as high as possible in order to maximize the signal rate. At TLK, a value of  $\epsilon_T \geq 95\%$  tritium purity can be maintained over the complete measurement period.

Furthermore, the WGTS has to fulfill stringent stability and monitoring margins in order to fulfill the KATRIN requirements mentioned above:

- The column density  $\rho d = 5 \cdot 10^{17}$  molecules/cm<sup>2</sup> has to be stabilized to a level of at least 0.1%. This requires a stabilization of key WGTS parameters like tube temperature or gas inlet pressure to the 0.1% level as well. Extensive test experiments have shown that all relevant source parameters can be controlled and monitored on the required level [Bab12].
- The tritium gas composition has to be accurately<sup>1</sup> monitored. A detailed discussion of the accuracy requirements of the composition monitoring is given in the following subsection (2.3.3).

### 2.3.3 Isotopic purity

The source gas with a tritium purity of  $\epsilon_T \geq 95\%$  consists mainly of molecular tritium T<sub>2</sub> ( $\geq 90\%$ ) with a small fraction of DT ( $< 10\%$ ) and trace amounts of HT, D<sub>2</sub>, HD and H<sub>2</sub>. The effects of fluctuations in the gas composition and the resulting requirements on the gas monitoring system will be discussed in the following.

**Precision requirements** According to eq. (2.13), the signal rate  $S$  at the detector is directly proportional to the tritium purity  $\epsilon_T$ , which means that any change in the isotopic purity has an impact on the measured  $\beta$ -decay spectrum. For this reason, relative changes in the gas composition have to be monitored with a relative precision of  $\Delta_{\text{prec}}(\epsilon_T)/\epsilon_T < 0.1\%$  [Bab12] in order to keep the contribution of these measurements to the total systematic uncertainty in the required range (see eq. (2.12)).

**Trueness requirements** In the case mentioned above, only relative changes in the composition are of interest, so that the precision of the measurement is important, but not its trueness. However, there are several secondary effects influencing the  $\beta$ -spectrum which require the knowledge of the true gas composition:

- **Nuclear recoil of the daughter molecule**

The momentum of the  $\beta$ -decay electron is balanced by the recoil of the daughter molecule. For the region close to  $E_0$ , the recoil energy can be approximated by the following formula [KAT05]:

$$E_{\text{rec}} \approx E_{e^-} \cdot \frac{m_{e^-}}{m_{\text{daughter}}} . \quad (2.14)$$

This recoil energy is missing in the phase space of the outgoing leptons, i.e. the endpoint energy is reduced by  $E_{\text{rec}}$ . Since the recoil energy depends on the mass of the daughter molecule, which differs significantly for the three daughter molecules of the tritiated hydrogen isotopologues ( $(^3\text{HeT})^+$ ,  $(^3\text{HeD})^+$ ,  $(^3\text{HeH})^+$ ), the observed  $\beta$ -spectrum represents a superposition of the single spectra of T<sub>2</sub>, DT and HT  $\beta$ -decay.

---

<sup>1</sup>The terminology of ‘precision’, ‘trueness’ and ‘accuracy’ is explained in appendix A.

- **Doppler broadening**

Due to the random motion of the molecules in the source gas, the energy of the  $\beta$ -decay products and hence the observed  $\beta$ -electron spectrum is influenced. In the non-relativistic approximation, the difference between the value observed in the laboratory system and the theoretical value, which is valid in the center-of-mass system of the decaying molecule, is given by [KAT05]

$$\Delta E \approx m_e \cdot v_e \cdot v_{\parallel, \text{mol}} \quad (2.15)$$

with the electron velocity  $v_e$  in the molecule's center-of-mass system and the velocity component  $v_{\parallel, \text{mol}}$  of the molecule in the direction of the outgoing electron. The velocity distribution of the gas molecules depends mainly on the gas temperature and the molecular masses. For heavier isotopologues like T<sub>2</sub>, the Doppler broadening  $\Delta E$  is smaller than for the lighter DT and HT molecules.

- **Elastic electron scattering from molecules**

The  $\beta$ -decay electrons can scatter elastically or inelastically off the source gas molecules. In case of elastic scattering, the energy loss of the electron in dependence of the scattering angle  $\theta$  is given by [KAT05]

$$\Delta E = 2 \cdot \frac{m_e}{m_{\text{mol}}} \cdot E_e \cdot (1 - \cos\theta) \quad (2.16)$$

and thus again depends on the mass of the involved source gas molecule.

- **Final state distributions**

With an excitation energy of 27 eV for the first electronic excited state of the T<sub>2</sub> daughter molecule (<sup>3</sup>HeT)<sup>+</sup>, the population of excited electronic states plays almost no role for the narrow energy region of interest for KATRIN [KAT05]. However, the nuclear recoil of the daughter molecule can lead to a large number of rotational-vibrational states, the distribution of which (and accordingly the mean excitation energy) differs for the daughter molecules of the individual isotopologues [Dos06].

In order to correctly account for these influences in the analysis of the  $\beta$ -decay spectrum, an accurate knowledge of the gas composition is crucial.

To obtain an estimate for the required trueness of the composition monitoring measurements, simulations have been performed which investigate the systematic shift on the observable  $m_\nu^2$  for different calibration uncertainties of the monitoring system [Sch12d]. Figure 2.5 shows the results of these simulations. It can be seen that for realistic calibration errors  $\sigma_{\text{cal}} \ll 50\%$  the systematic shift is  $\Delta m_\nu^2 \leq 3 \cdot 10^{-2} \text{ eV}^2$ .

However, in order to obtain the total systematic error connected to the effects listed above, apart from the calibration errors also the errors from the theoretical descriptions of these effects have to be taken into account by adding all errors in quadrature. With a systematic shift of  $\Delta m_\nu^2 = 6 \cdot 10^{-2} \text{ eV}^2$ , the largest contribution to the error budget comes from the theoretical description of the final state distributions [KAT05].

In order to keep the total systematic uncertainty as low as possible, one aims for a calibration uncertainty of 10% or better. In this case, the uncertainty contribution by the LARA calibration will not contribute significantly to the combined uncertainty [Sch12b].

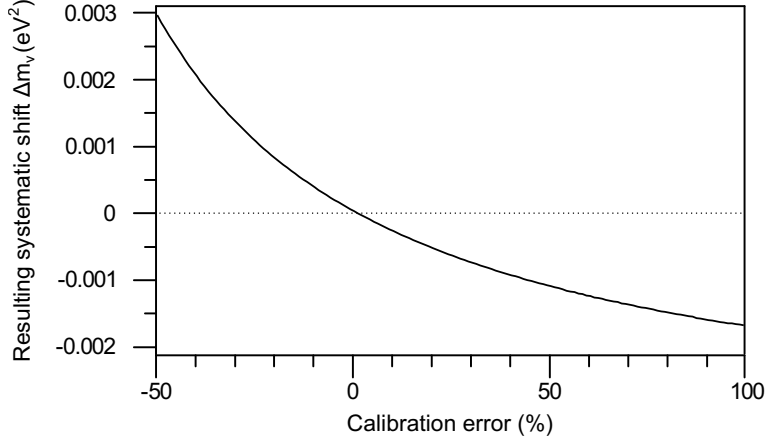


**Figure 2.5: Dependence of the systematic shift of  $m_\nu^2$  on the calibration error of the composition monitoring system.** The calibration error  $\sigma_{\text{cal}}$  relates the assumed (i.e. measured) relative tritium amount to the true value:  $n_{\text{assumed},T_2,\text{rel}} = \frac{n_{\text{true},T_2} \cdot (1 + \sigma_{\text{cal}})}{n_{\text{true},T_2} \cdot (1 + \sigma_{\text{cal}}) + n_{\text{true},DT}}$ . Note that in this simulation, the term ‘calibration error’ refers only to the relative error in the calibration factor which relates the relative amounts of  $T_2$  and  $DT$ , i.e. the main components of the source gas. (According to [Sch12d].)

**The KATRIN composition monitoring method** For a successful neutrino mass measurement, a continuous, real-time monitoring of the WGTS gas composition is required which fulfills the accuracy requirements mentioned above. In this regard, laser Raman spectroscopy has proven to be a specifically advantageous instrument [Fis11, Sch11b]. Most importantly, it offers an excellent separation of the different hydrogen isotopologues present in the source gas. Moreover, measurements can be performed contactless, so that a contamination of the Raman system by the tritiated gas mixture can be avoided. An introduction to laser Raman spectroscopy is given in section 3.1. The laser Raman (LARA) system which has been developed for the KATRIN experiment is presented in section 3.2.

**Accuracy of the KATRIN laser Raman system** In the earlier test experiment LOOPINO it was shown that laser Raman spectroscopy is a feasible method for the long-term monitoring of the WGTS gas composition [Fis11]. Under KATRIN-like measurement conditions, a precision of 0.1% was achieved in less than 250 s sampling time, thus fulfilling the precision requirements.

In order to fulfill the trueness requirements, an accurate intensity calibration of the Raman system employed is necessary. In this thesis, a novel method for the accurate calibration of the laser Raman system for KATRIN is presented, which is based on the determination of the system’s spectral sensitivity. Its applicability for this purpose is discussed in detail (see chapter 4). By making use of a second, independent approach based on accurate gas samples to verify the results, it is shown that said method is well able to fulfill the KATRIN requirements (chapter 5).

## Chapter 3

# Quantitative Raman spectroscopy for KATRIN

This chapter gives an introduction to quantitative Raman spectroscopy and its application in the KATRIN experiment. In section 3.1, the theoretical background of Raman spectroscopy is given as far as necessary for the understanding of this thesis, and the use of this technique at KATRIN is clarified. Section 3.2 gives an overview of the experimental setup of the laser Raman system employed for KATRIN. Possible approaches for the calibration of this system are presented and discussed in section 3.3.

### 3.1 The Raman effect

In the following, an introduction to Raman spectroscopy and its theoretical background is given. The theoretical descriptions in subsections 3.1.1 and 3.1.3 are based on [Hak06], [Lon02] and [Dem07].

#### 3.1.1 Basic principle of Raman scattering

The term Raman scattering denotes the inelastic scattering of light off molecules. It is named after C. V. Raman, who discovered the effect together with K. S. Krishnan in 1928 [Ram28].

In the classical description of the Raman effect, an incident electromagnetic wave with electric field vector  $\vec{E} = \vec{E}_0 \cdot \cos(\omega t)$  induces an oscillating dipole moment

$$\vec{p}_{\text{ind}} = \underline{\alpha} \cdot \vec{E} \quad (3.1)$$

in a molecule with polarizability tensor  $\underline{\alpha}$ . Due to the oscillation of the dipole moment, new light waves are produced. In this process, changes in the molecular polarizability account for Raman scattering, in which the frequency of the emitted light is shifted relative to the one of the incident light.

In the quantum mechanical picture of such a scattering process, a molecule in a certain initial state is excited into a virtual state by absorbing a photon, and enters into its final

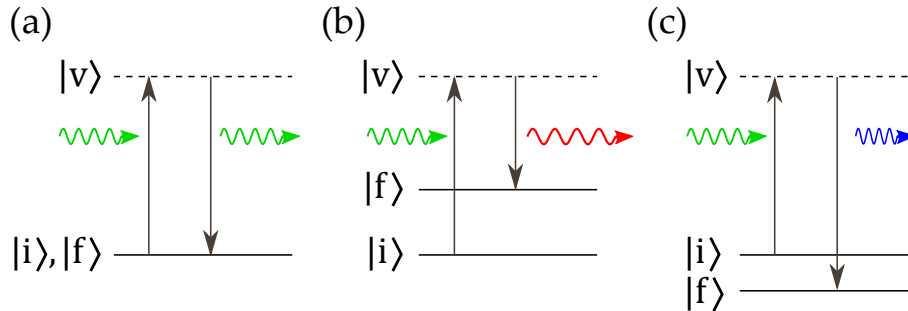


**Figure 3.1: Different types of scattering of light in the quantum mechanical picture.**  $|i\rangle$  denotes the initial,  $|f\rangle$  the final and  $|v\rangle$  the virtual state. (a) Rayleigh scattering (elastic,  $|i\rangle = |f\rangle$ ); (b) Stokes Raman scattering (inelastic,  $E_i < E_f$ ); (c) anti-Stokes Raman scattering (inelastic,  $E_i > E_f$ ). (According to [Hak06].)

state by emitting a photon again. As illustrated in figure 3.1, different types of scattering can be distinguished depending on the relation of initial and final state:

- **Rayleigh scattering.** Here, initial and final state are identical, i.e. the scattering process is elastic.
- **Stokes Raman scattering.** In this scattering process the molecule is excited to a higher energetic state. Since energy is transferred to the molecule by this inelastic process, the wavelength of the scattered photon increases.
- **Anti-Stokes Raman scattering.** If the initial state is not the ground state, the molecule can also de-excite to a less energetic state. In this case, the scattered photon gains energy, so that its wavelength decreases.

Excited states in molecules can arise from electronic, rotational and vibrational excitations. In the case of non-resonant Raman scattering, which is the case considered in this work, only rotational and vibrational (rovibrational) excitations are of relevance. For diatomic molecules like hydrogen, the energy levels of the excitations and thus the resulting spectrum can be approximated using the semi-classical model of a rotating, anharmonic oscillator<sup>1</sup>. A theoretical treatment of said excitations in diatomic molecules in the framework of this model is given in appendix B. It leads to the following formula for rovibrational energy levels:

$$E(v, J) = \hbar\omega_e \left( v + \frac{1}{2} \right) - x_e \hbar\omega_e \left( v + \frac{1}{2} \right)^2 + hcB_v J(J+1) - hcD_v J^2(J+1)^2. \quad (3.2)$$

The first two terms represent the contribution by anharmonic oscillation with the angular eigenfrequency  $\omega_e$  and the anharmonicity constant  $x_e$ . This contribution depends on the vibrational quantum number  $v$ . The third and fourth term are connected to the rotation of the molecule parameterized by the rotational quantum number  $J$ , but are also dependent on  $v$  via the rotational constant  $B_v$  and the stretching constant  $D_v$ .

<sup>1</sup>Note that this approximation is sufficiently good to explain observed Raman spectra; a more accurate description, however, requires more sophisticated calculations.

**Table 3.1: Classification of branches in the Raman spectrum according to selection rules.** The selection rule for rotational transitions is given by  $\Delta J = 0, \pm 2$  in the case of the two-photon process of Raman scattering. For vibrational transitions, the rule is  $\Delta v = 0, \pm 1$ . The selection rules define the branch name, as shown in the table below:  $\Delta J$  is denoted by the letter  $O$ ,  $Q$  and  $S$  for  $\Delta J = -2, 0$  and  $+2$ , respectively, while  $\Delta v$  is indicated by the letter's index. Anti-Stokes Raman lines and vibrational overtones ( $|\Delta v| > 1$ ) are not considered here, since they are of no relevance for this thesis. (According to [Lew07].)

Scattering type	Selection rules		Branch name	Raman shift
	$\Delta v$	$\Delta J$		
Rayleigh	0	0	$Q_0$	-
Stokes Raman (pure rotation)	0	+2	$S_0$	$\tilde{\nu}_i - \tilde{\nu}_{\text{rot}}$
Stokes Raman (rotation- vibration)	1	-2	$O_1$	$\tilde{\nu}_i - \tilde{\nu}_{\text{vib}} + \tilde{\nu}_{\text{rot}}$
	1	0	$Q_1$	$\tilde{\nu}_i - \tilde{\nu}_{\text{vib}}$
	1	+2	$S_1$	$\tilde{\nu}_i - \tilde{\nu}_{\text{vib}} - \tilde{\nu}_{\text{rot}}$

In a scattering process, the difference between the energy levels of initial and final state,  $\Delta E = E_f(v', J') - E_i(v'', J'')$ , represents at the same time the energy difference between incident and emitted photon, and thus their wavelength difference. In a spectrum arising from the scattering of light off molecules, the line positions correspond to the wavelengths  $\lambda_f$  of the emitted photons and are hence given by

$$\lambda_f = \lambda_i - \Delta\lambda = \lambda_i - hc \cdot \left( \frac{1}{E_i} - \frac{1}{E_f} \right). \quad (3.3)$$

In the field of Raman spectroscopy, spectra are typically plotted as a function of Raman shift instead of wavelength. This shift, which denotes the energy shift between incident and emitted photon, is usually expressed in wavenumbers  $\bar{\nu} = \frac{1}{\lambda}$ :

$$\Delta\bar{\nu} = \bar{\nu}_i - \bar{\nu}_f = \frac{1}{\lambda_i} - \frac{1}{\lambda_f} = \frac{E_i - E_f}{hc} = \frac{\Delta E}{hc}. \quad (3.4)$$

The use of the Raman shift allows a direct comparison of Raman spectra, independent of the excitation wavelength.

Due to their different initial and final states, the different scattering types listed above (Rayleigh, Stokes and anti-Stokes) result in different spectral branches in the spectrum. These are further subclassified according to the selection rules of the quantum numbers  $v$  and  $J$  of the excitations. Table 3.1 gives an overview of these branches and the corresponding Raman shift. A typical Raman spectrum of a diatomic molecule, including said branches, is shown in figure 3.2.

### 3.1.2 Laser Raman spectroscopy

Raman spectroscopy is a spectroscopic method based on the Raman effect. It is used not only for the investigation of molecular excitations, but plays an important role for

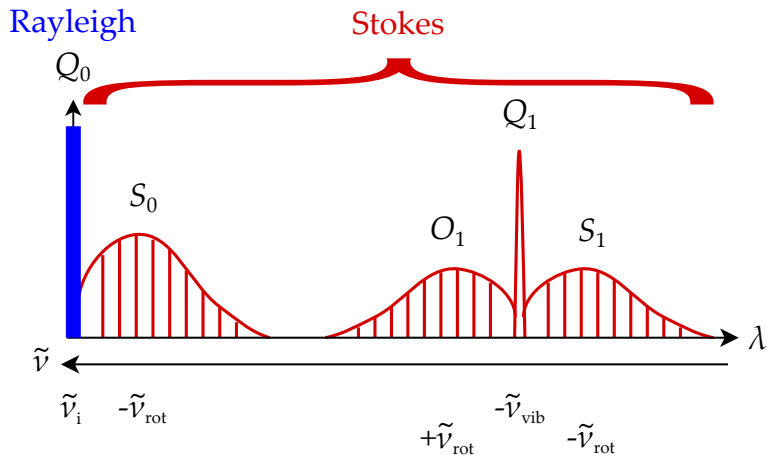


**Figure 3.2: Schematic Raman spectrum of a diatomic molecule.** The plot shows typical, qualitative line positions and intensities for Stokes Raman scattering. At the initial laser wavelength (wavenumber), the Rayleigh line is located, starting from which the Stokes Raman lines are shifted to higher wavelengths (lower wavenumbers). It can be seen that the shift due to vibrational excitation is much larger than the ones due to pure rotational excitations. A discussion of the line intensities is given in subsection 3.1.3. (According to [Hak06].)

compositional analyses as well. Different components of a gas sample can be identified by their respective peaks in a Raman spectrum, since the energy levels of molecular excitations and thus the wavelength shifts of Raman scattered light are characteristic for the molecule which is scattered off. This is illustrated in figure 3.3 using the Raman spectrum of a gas mixture of  $\text{H}_2$ , HD and  $\text{D}_2$  as an example.

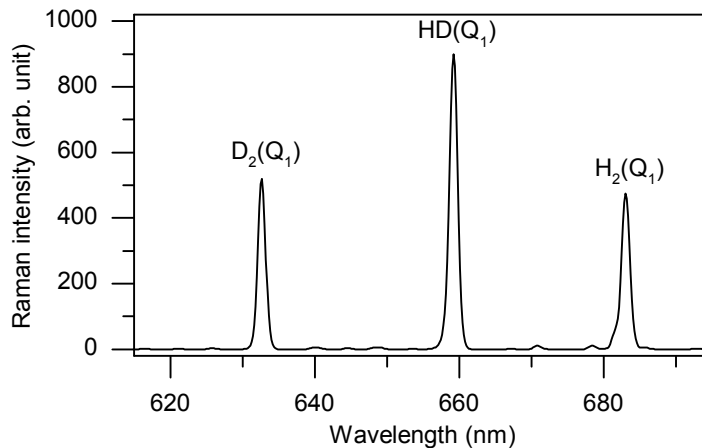


**Figure 3.3: Raman spectrum of a mixture of  $\text{H}_2$ , HD and  $\text{D}_2$  gas for an excitation wavelength of 532 nm.** The  $Q_1$ -branches of the different molecule types are clearly separated from each other and allow to identify the gas constituents by their characteristic positions on the wavelength scale. The minor, unlabeled peaks between the dominant  $Q_1$ -branches are  $S_1$ - and  $O_1$ -branch lines.

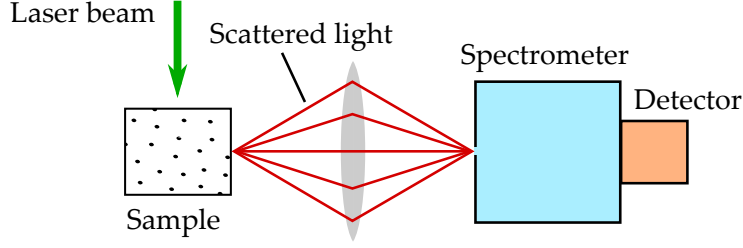


**Figure 3.4: Measurement setup for Raman spectroscopy (schematic).** The Raman scattered light is collected by optics in a  $90^\circ$  geometry and its spectrum is analyzed by a spectrometer and a detector. The observation of scattering light perpendicular to the excitation beam is advantageous for Raman spectroscopy, since the fraction of collected primary light is reduced. However, other Raman techniques exist which use a different scattering geometry [Fer94]. (According to [Hak06].)

Raman cross-sections are in general very low, with the typical scattering probability of a single photon being of the order of  $10^{-7}$  [Atk06]. For this reason, lasers with high intensities are used as excitation light sources in Raman spectroscopy. Figure 3.4 shows a typical Raman measurement setup. A description of the Raman system used for KATRIN is given in section 3.2.

The use of Raman spectroscopy for compositional sample analysis has several advantages. Multiple species can be detected simultaneously using only one excitation wavelength. Furthermore, molecules lacking a permanent electric dipole moment can also be detected, in contrast e.g. to infrared spectroscopy [Atk06]. Gaseous, liquid and solid samples with all sorts of optical properties can be investigated without special sample preparation. Moreover, the method is contact-free; in particular, it allows spatial separation of the environments of sample and optical system [Pel03].

These properties make Raman spectroscopy an excellent instrument for isotopic purity measurements for the KATRIN experiment, allowing simultaneous monitoring of all hydrogen isotopologues without directly exposing the optical system to high  $\beta$ -decay activities. The feasibility of using this technique for KATRIN has been demonstrated in several studies and test experiments, which have shown that the KATRIN requirements on sensitivity [Sch11b] and precision [Fis11] can be fulfilled. The fulfilling of the trueness requirements is discussed in this thesis and [Sch12e].

### 3.1.3 Raman intensities

The models discussed in subsection 3.1.1 allow to calculate the positions of Raman lines, but not the corresponding line intensities. The latter can be derived using quantum mechanical calculations, which are discussed in detail in the literature, e.g. in [Lon02], from which the following formula is taken.

When a population of diatomic molecules is exposed to irradiation, the intensity of the Raman scattered light is given by

$$I' = k_\lambda \cdot \lambda_s^{-4} \cdot N_i \cdot \Phi_{p^i, p^s}(\varphi, \theta, a, \gamma) \cdot \mathcal{I} . \quad (3.5)$$

The individual factors are explained below.

Note that this formula with the important wavelength-dependence  $I' \propto \lambda_s^{-4}$  applies if the scattered intensity is measured in units of power. Often, however, the number of scattered photons is measured instead. This is the case e.g. for most CCD detectors, which are employed also in the Raman system of the KATRIN experiment (see section 3.2). According to [McC06], in this case the  $\lambda_s^{-4}$  factor has to be replaced by  $\lambda_i^{-1}\lambda_s^{-3}$ , so that the intensity is now given by

$$I = k_\lambda \cdot \lambda_i^{-1} \cdot \lambda_s^{-3} \cdot N_i \cdot \Phi_{p^i, p^s}(\varphi, \theta, a, \gamma) \cdot \mathcal{I} . \quad (3.6)$$

This equation includes the following factors:

$k_\lambda$  is a constant given by

$$k_\lambda = \frac{\pi^2}{\epsilon_0^2} \approx 1.259 \cdot 10^{23} \text{ m}^2 \text{F}^{-2} . \quad (3.7)$$

$\lambda_i, \lambda_s$  are the wavelengths of incident ( $\lambda_i$ ) and scattered ( $\lambda_s$ ) light.

$N_i$  is a transition-dependent population factor. It represents the number of molecules in the initial state in thermodynamic equilibrium and is defined by a Boltzmann distribution:

$$N_i(E_i) = N \cdot \frac{g_i \cdot \exp\left(-\frac{E_i}{kT}\right)}{Z} . \quad (3.8)$$

In this expression,  $N$  is the total number of molecules exposed to irradiation,  $g_i$  the statistical weight of the initial state,  $k$  the Boltzmann constant,  $T$  the temperature of the molecules,  $E_i$  the energy of the initial state, and  $Z$  the molecular partition function:

$$Z = \sum_j g_j \cdot \exp\left(-\frac{E_j}{kT}\right) . \quad (3.9)$$

The statistical weight  $g_i = g_v \cdot g_J$  depends on the respective statistical weights of vibrational ( $g_v$ ) and rotational ( $g_J$ ) states. For diatomic molecules such as the hydrogen isotopologues considered here, the vibrational levels are non-degenerate and thus  $g_v = 1$ , while  $g_J$  depends on the rotational quantum number  $J$ :

$$g_J = g_N \cdot (2J + 1) \quad (3.10)$$

with the nuclear spin degeneracy  $g_N$ . In the case of the heteronuclear diatomic molecules HD, HT and DT  $g_N = 1$ . However, different  $J$ -dependent values are taken in the case of homonuclear molecules due to the influence of nuclear spin statistics. In the case of the molecules  $\text{H}_2$  and  $\text{T}_2$ , which consist of two fermionic nuclei,  $g_N = 1$  for even  $J$  and 3 for odd  $J$ ; for  $\text{D}_2$  with its bosonic nuclei,  $g_N = 6$  for even  $J$  and 3 for odd  $J$ .

The population of rotational levels is then given by

$$N_J(E_{v,J}) = N \cdot \frac{g_N \cdot (2J + 1) \exp\left(-\frac{E_{v,J}}{kT}\right)}{\sum_j g_N \cdot (2j + 1) \cdot \exp\left(-\frac{E_{v,j}}{kT}\right)}. \quad (3.11)$$

During the Raman measurements for KATRIN, the gas has approximately room temperature. In this case, the only vibrational level which has to be considered as initial state is the lowest vibrational state; the relative population of higher excited states is below the detection limit of the LARA system [Sch09].

$\Phi_{p^i, p^s}(\varphi, \theta, a, \gamma)$  is the molecule-dependent line strength function. It depends on the scattering geometry (defined by the scattering angles  $\varphi$  and  $\theta$ ) as well as on the polarization of incident and scattered light ( $p^i, p^s$ ). The line strength function is a function of the transition tensor invariants  $a$  and  $\gamma$ , which can be derived from quantum-mechanical calculations; this will be discussed in section 4.2.

$\mathcal{I}$  denotes the irradiance of the incident light.

According to eq. (3.6) and (3.8), the Raman line intensities of a certain type of molecule are proportional to the total number of molecules of this type present in the scattering volume:

$$I \propto N. \quad (3.12)$$

This means that in principle the composition of a sample can be obtained by the analysis of its Raman spectrum. This is the basic concept behind the determination of the composition of source gas in the WGTS (cf. section 2.3.3). It will be discussed in more detail in the following.

### 3.1.4 Quantitative analysis of Raman spectra

For the quantitative analysis of KATRIN Raman spectra, the  $Q_1$ -branches of the different hydrogen isotopologues are used. As can be seen in figure 3.5, these peaks are well separated from each other.<sup>2</sup> Furthermore, the single rotational levels of the  $Q$ -branch are, in contrast to those of the  $S$ - and  $O$ -branches, very close to each other and appear as one single, slightly distorted line for the spectral resolution employed here. This is well visible for the  $Q_1$ -branch of  $H_2$  in figure 3.5.<sup>3</sup> Integration over all the temperature-dependent rotational levels of the  $Q$ -branch (compare eq. (3.11)) leads not only to a higher peak intensity compared to the individual lines of the  $S$ - and  $O$ -branches, but makes the measured absolute signal also largely independent of temperature. Thus, instead of individual line intensities as described by eq. (3.6), the quantity used for analysis is the Raman signal amplitude  $S_x$ , which is given by the total peak area of the  $Q_1$ -branch of a certain isotopologue  $x$  ( $x=H_2, HD, D_2, HT, DT, T_2$ ).

<sup>2</sup>Minor interferences with  $S$ - and  $O$ -branch lines, as reported in [Sch09], are considered in the analysis. The procedure is described in appendix D.2.

<sup>3</sup>The distortion is maximal for the lightest of the isotopologues, because the energy shift between the individual rotational levels increases with decreasing mass of the molecule. This is discussed in detail in [Sch09].

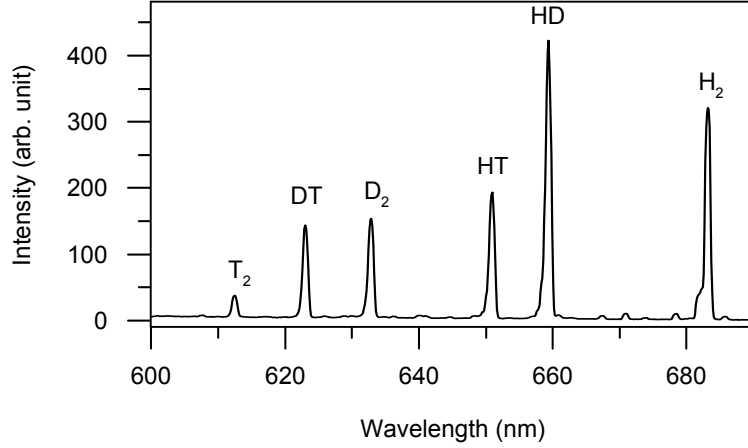


**Figure 3.5:** Typical Raman spectrum of a gas mixture containing all hydrogen isotopologues. The respective  $Q_1$ -branches are denoted in the plot. (From [Sch09].)

In general, relative Raman signal amplitudes are used rather than absolute ones: by normalizing the Raman signal amplitude of each isotopologue to the sum of all signal amplitudes,

$$S_{x,\text{rel}} = \frac{S_x}{\sum_i S_i}, \quad (3.13)$$

the results can be compared independently of fluctuations in the laser power.

The above mentioned proportionality between line intensity and number of molecules,  $I_x \propto N_x$ , translates to the relative Raman signal amplitude  $S_{x,\text{rel}}$ :

$$S_{x,\text{rel}} = R_x \cdot N_x. \quad (3.14)$$

The proportionality factor introduced here is the so-called response function  $R_x$ . Basically, it is a measure of the Raman cross-section of a specific molecule. However, as will be discussed in detail in section 3.2, each Raman system has a certain wavelength- and polarization-dependent influence on the measurement and hence on the measured Raman signals. For this reason, the actual response function depends not only on the type of molecule which the light is scattered off, but also on the Raman system employed.

In order to make the response functions independent of the absolute number of molecules  $N_x$ , relative response functions can be calculated by normalizing the absolute  $R_x$  value of each isotopologue to the mean of all response functions:

$$R_{x,\text{rel}} = \frac{R_x}{R_{\text{mean}}} = n \cdot \frac{R_x}{\sum_i R_i}. \quad (3.15)$$

For the quantitative analysis of the KATRIN Raman spectra, a determination of these response functions  $R_{x,\text{rel}}$  for all hydrogen isotopologues is necessary, i.e. an intensity calibration of the LARA system employed (see section 3.3).

### 3.2 Setup of the KATRIN laser Raman system

A sketch of a typical Raman system consisting of light source, sample and light detection system was shown in figure 3.4. The actual setup of such a Raman system for KATRIN, here referred to as LARA (Laser Raman) system, can be seen in figure 3.6. In the following, the components are briefly described. Note that multiple LARA systems (LARA 1, LARA 2, LARA 3) are currently in use with almost equal setup and components; an overview of the respective main components is given in table 3.2.

**Laser** The lasers employed in the different setups are diode-pumped solid state lasers with an output wavelength of 532 nm and a maximum power of 3 W (LARA 2) to 5 W (LARA 1, 3). For details see table 3.2.

**Mirrors** The mirrors offer a reflectivity of  $> 99.6\%$ . They guide the laser beam through the setup. In a modified setup, the laser beam is reflected back through the cell by mirror 2 (right side of the setup in figure 3.6) in order to enhance the Raman signal.

**Glan-Taylor polarizer** A Glan-Taylor polarizer (GT5-A from Thorlabs, [www.thorlabs.com](http://www.thorlabs.com), nominal extinction ratio  $10^5:1$ ) is installed in a region of collimated light before the beam is focused into the sample cell. It provides a clean linear polarization, which is important to obtain applicable calculation results of the Raman line strength functions (see section 4.2 in the following chapter). Depending on the initial laser polarization, a half-wave plate has to be additionally inserted behind the Glan-Taylor-Polarizer, which turns the laser light from horizontal to vertical polarization.

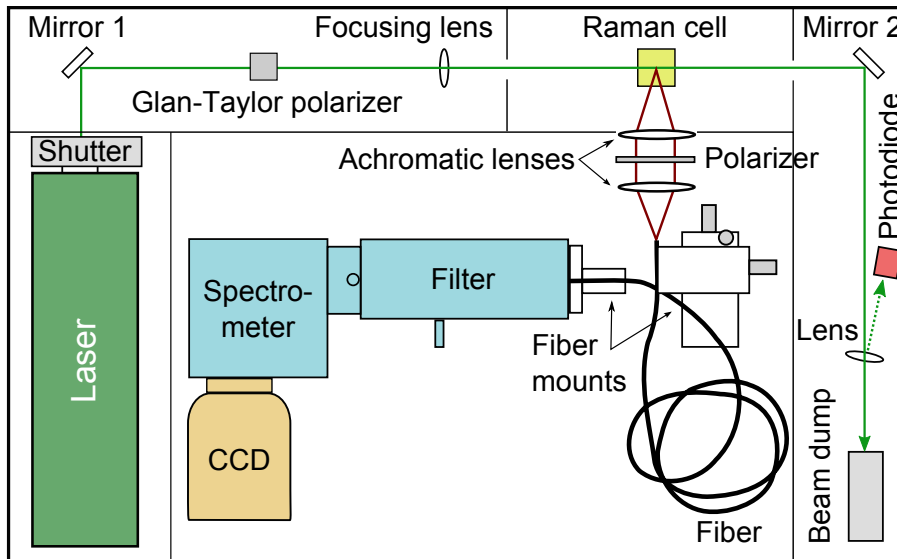


**Figure 3.6: Schematic sketch of the LARA 1 setup.** The polarized laser beam is focused into the Raman cell, where scattering takes place. Scattered light leaves the cell at an  $90^\circ$  angle to the beam direction and is collected and analyzed in the following detection system. All components are mounted on a breadboard. In operation mode, the whole system is surrounded by a light tight enclosure. (Modified from [Sch09].)

Table 3.2: Overview of the components of the different LARA systems.

	LARA 1	LARA 2	LARA 3
<b>Laser</b>			
Manufacturer	Coherent Inc. <sup>a</sup>	Laser Quantum <sup>b</sup>	Laser Quantum <sup>b</sup>
Model	Verdi V5	Opus	Finesse
Gain medium	Nd : YVO <sub>4</sub>	Nd : YAG	Nd : YAG
Power	5 W	3 W	5 W
Output polarization	vertical	horizontal	horizontal
<b>Sheet polarizer in collection optics</b>			
Manufacturer	Thorlabs Inc. <sup>c</sup>	Thorlabs Inc. <sup>c</sup>	Edmund Optics <sup>d</sup>
Model	LPVISE200-A	LPVISE200-A	NT43-787
Extinction ratio (600-700nm)	> 5000 : 1	> 5000 : 1	> 1500 : 1
Transmission (600-700nm)	> 72%	> 72%	30%
<b>Spectrometer</b>			
Manufacturer	Princeton Instruments <sup>e</sup>	Princeton Instruments <sup>e</sup>	Acton Research Corp. <sup>f</sup>
Model	SP2150	HTS Lens Spectrograph	SP500
Focal length	150 mm	300 mm	500 mm
Aperture ratio	$f/4.0$	$f/1.8$	$f/6.5$
Installed gratings	600 g mm <sup>-1</sup> , 1800 g mm <sup>-1</sup>	600 g mm <sup>-1</sup>	150 g mm <sup>-1</sup> , 600 g mm <sup>-1</sup> , 2400 g mm <sup>-1</sup>
<b>CCD</b>			
Manufacturer	Princeton Instruments <sup>e</sup>	Princeton Instruments <sup>e</sup>	Princeton Instruments <sup>e</sup>
Model	PIXIS:400B	PIXIS:2KB	PIXIS:400B
Array dimension	1340 × 400 array	2048 × 512 array	1340 × 400 array
Pixel dimension	20 × 20 μm pixel	13.5 × 13.5 μm pixel	20 × 20 μm pixel

<sup>a</sup> Coherent Inc., Santa Clara, California, USA <http://www.coherent.com><sup>b</sup> Laser Quantum Ltd., Stockport, Cheshire, UK, [www.laserquantum.com](http://www.laserquantum.com)<sup>c</sup> Thorlabs Inc., Newton, New Jersey, USA, [www.thorlabs.com](http://www.thorlabs.com)<sup>d</sup> Edmund Optics, Barrington, New Jersey, USA, [www.edmundoptics.com](http://www.edmundoptics.com)<sup>e</sup> Princeton Instruments, Trenton, New Jersey, USA, <http://www.princetoninstruments.com><sup>f</sup> Acton Research Corporation, Acton, Massachusetts, USA. Note that the follow-up models are now produced by Princeton Instruments.

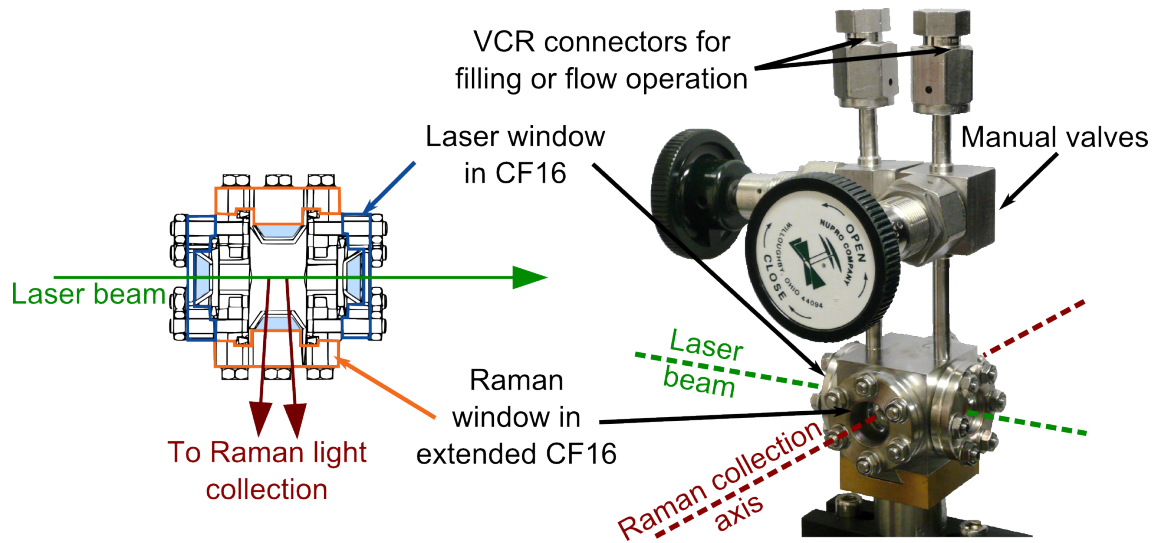


**Figure 3.7: Raman cell.** The following descriptions are based on [Tay01]. *Left:* Cross sectional view. The laser beam passes through the two laser windows, which have an anti-reflection coating optimized for 532 nm. The Raman scattered light is collected at an angle of  $90^\circ$  relative to the beam through a third window, which is coated with a broadband AR-coating providing a good transmission of the scattered light. Both types of windows are made of fused silica, which provide low internal absorption and fluorescence. They are diffusion bonded into CF16-flanges to allow for a leak-tight connection to the cell body. *Right:* Complete Raman cell. The cell is filled with gas via the manual valves connected to the cell body. (From [Sch12b].)

**Focusing lens** A lens with a focal length of 250 mm focuses the laser beam into the sample cell. The lens has an anti-reflective coating which minimizes intensity losses due to reflection to  $< 0.4\%$ .

**Raman cell** The Raman cell is the part of the Raman system which contains the gas sample. The cell design was developed by Taylor et al. [Tay01]; it is shown and described in 3.7. The valve-bearing inlets allow for either flowing or static gas samples [Stu10b].

**Safety equipment** For safety reasons, a shutter is inserted behind the laser, which is closed if the top cover of the system is opened or if the beam diverges from its reference path. To check for beam displacements, a small fraction of the laser beam is continuously monitored by a photodiode at the end of the optical path, which triggers the shutter if the measured power drops below a certain value. The rest of the laser beam is guided to a beam dump.

**Achromatic lenses** The scattered light is collected and focused onto an optical fiber by two achromatic, plano-convex 2" lenses with a focal length of 75 mm and anti-reflective coating (AC508-075-A-ML from Thorlabs, [www.thorlabs.com](http://www.thorlabs.com)). The achromatic lenses were introduced in the course of this thesis to replace the former non-achromatic lenses. This was a consequence of the results from experimental studies reported in the bachelor thesis of S. Mirz [Mir11], which showed a strong dependence

of measured Raman intensities on the focusing of the collection optics (see section 4.3.1). The introduced achromatic lenses reduce chromatic aberrations and thus the influence of the collection optics on the measured spectrum.

**Polarizer** A sheet polarizer is inserted in the region of collimated light between the two achromats, so that only vertical polarized light enters the detection system. For details see table 3.2.

**Fiber** An optical fiber bundle comprising 48 individual, adjoining fibers with core/cladding diameter  $100\ \mu\text{m}/125\ \mu\text{m}$  transfers the scattered light to the spectrometer.

**Filter** An edge filter (RazorEdge® filter LP03-532RU-25, Semrock Inc., <http://www.semrock.com>) in front of the spectrometer suppresses the Rayleigh scattered light at the laser wavelength of 532 nm by a factor of  $10^8$  to  $10^9$ . This large suppression factor is necessary since the Rayleigh scattered light is approximately a factor  $10^3$  more intense than the Raman light. A smaller suppression factor would thus induce a too high background on the CCD chip due to stray light in the spectrometer.

**Spectrometer** The spectrometer uses a grating to separate the incoming light into its spectral components. Depending on the LARA system, a transmitting optics type or a Czerny-Turner type spectrometer is used, i.e. the light is passed through the system by either lenses or mirrors. For details see table 3.2.

**CCD** A CCD (Charged Coupled Device) array is used to convert the scattered photons into electric charges. It is back-illuminated, which offers a good quantum efficiency ( $Q_e \approx 95\%$ ), and can be cooled down to  $-75\ \text{°C}$  for the reduction of dark noise.

**Spectral sensitivity of the detection system** The spectral sensitivity  $\eta(\lambda)$  is defined as the response of a device or material to monochromatic light as a function of wavelength [Par03]. All optical components in the light path, i.e. the Raman cell window, the collection optics and the following detection system comprising fiber, edge filter, spectrometer and CCD, have a certain wavelength- and polarization-dependent response and therefore contribute to the total spectral sensitivity of the system. The relevance of  $\eta(\lambda)$  for the quantitative analysis of Raman spectra for KATRIN will be discussed in section 3.3. The main contributions to the spectral sensitivity originate from the following components:

- **Edge filter.** The filter transmission is wavelength-dependent, as can be seen in the top panel of figure 3.8. The transmission factor is  $> 98\%$  over the wavelength region of the  $Q_1$ -branches of the hydrogen isotopologues, which is between approximately 600 nm and 700 nm. Nevertheless, oscillatory variations of the transmission function cause differences in the detected intensity of up to 1% over narrow wavelength ranges.
- **Spectrometer and fiber bundle.** The grating efficiency of the spectrometer is strongly wavelength-dependent, as shown in the bottom panel of figure 3.8 for the SP2150 spectrometer used in the LARA 1 setup. Additionally, the polarization of the incoming light plays a non-negligible role: according to the specifications of the SP2150 spectrometer, its efficiency differs by up to 18 percentage points in the relevant wavelength range due to different polarizations [Pri10b]. This is one reason

why a sheet polarizer was inserted between the collection lenses<sup>4</sup>. It ensures that only vertically polarized light enters the detection system, so that the measured spectrum is independent of the original polarization of the emitted light.

In this context, it should be noted that the polarization of the incoming light is not fully conserved by the fiber bundle [Ste84, Hol94]. The degree of depolarization depends on the position of the fiber. Accordingly, a movement of the fiber can result in a change of the measured Raman spectrum due to the polarization-dependence of the spectrometer. For this reason, it is important not to move the fiber bundle after an intensity calibration of the system<sup>5</sup> in order not to alter the spectral sensitivity and make the calibration invalid.

- **The CCD.** The back-illuminated chip offers a good quantum efficiency of  $> 95\%$ , which nonetheless differs depending on the wavelength of the incoming light. In case of the PIXIS:2KB as an example, the quantum efficiency differs by  $\sim 2\%$  over the wavelength range of interest, as can be seen in the bottom panel of figure 3.8.

### 3.3 Raman intensity calibration methods

In section 3.1.4 it was shown that a quantitative analysis of Raman spectra for the determination of the KATRIN source gas composition requires an intensity calibration of the LARA system.

Possible approaches to achieve such a calibration are

- the use of a reference method for cross-calibration;
- the use of accurate calibration gas samples;
- the combination of theoretical values for the Raman cross-sections and the experimentally obtained spectral sensitivity of the system.

The different methods and their respective difficulties are discussed in the following.

#### 3.3.1 Accurately known gas samples

The most straight-forward approach for a Raman intensity calibration is the use of gas samples of accurately known composition: in this case, one only has to measure the Raman spectrum of the gas sample. Then the gas composition and thus the mole fraction

$$y_x = \frac{N_x}{\sum_i N_i} . \quad (3.16)$$

---

<sup>4</sup>The sheet polarizer serves a second purpose as well: the polarizations of both incident and scattered light have to be clearly defined in order to be able to choose the right line strength function for the calculation of the response functions. This is described in more detail in section 4.2

<sup>5</sup>The intensity calibration of the LARA system is discussed in detail in section 3.3.

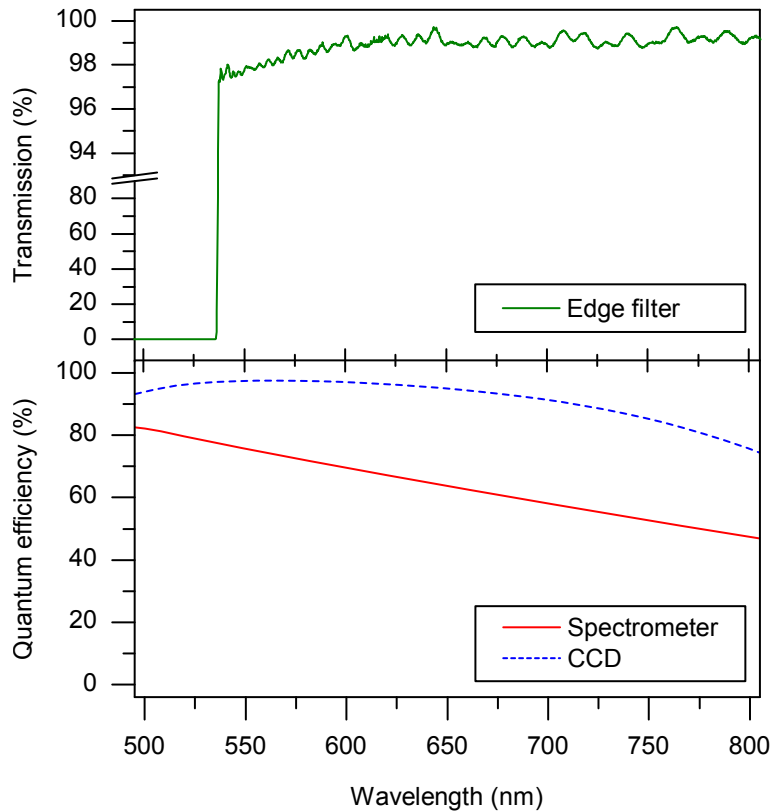


**Figure 3.8: Wavelength-dependence of edge filter transmission and spectrometer/CCD quantum efficiency.** Top panel: Edge filter transmission curve of the Semrock RazorEdge filter LP03-532RU-25 [Sem12]. The filter blocks light below the edge wavelength of 536.4 nm, but is almost transparent for longer wavelengths. However, the curve exhibits an oscillatory behaviour in the visible range. Bottom panel: Quantum efficiency curve of the SP2150 spectrometer [Pri10a] and the PIXIS:2KB CCD [Pri11], both from Princeton Instruments. In the region of interest for KATRIN, i.e. between approximately 600 nm and 700 nm, the quantum efficiency decreases for longer wavelengths in both cases. All three curves are provided by the manufacturers and represent typical curves for this instrument series.

of each molecule type  $x$  is known, and the corresponding Raman signal amplitudes  $S_{x,\text{rel}}$  are obtained from the spectrum, so that the response functions  $R_x$  for each isotopologue can be easily determined according to eq. (3.14):

$$R_x = \frac{S_{x,\text{rel}}}{N_x} \quad (3.17)$$

$$= \frac{S_{x,\text{rel}}}{y_x \cdot \sum_i N_i} . \quad (3.18)$$

The factor  $\sum_i N_i$ , which represents the unknown total number of molecules, cancels out when relative response functions are calculated.

The challenge in this method, however, is how to obtain the required knowledge of the gas composition. There are basically two methods possible, which will be discussed in the following with regard to the situation present at KATRIN:

**Use of a reference method for cross-calibration** The first possibility is to measure the gas sample composition with a reference method. If the LARA system is supposed to fulfill the KATRIN requirements of a calibration uncertainty of less than 10% (see 2.3.3), this reference method forming only an intermediate step in the calibration procedure has to provide an even better trueness than that.

For composition measurements of tritiated gas mixtures, however, there is hardly any reference method available which can fulfill these requirements (see e.g. [Nis06, Dem12]). At the Tritium Laboratory Karlsruhe (TLK), a laboratory with renowned expertise in tritium analytics, no system is available as yet which could provide the required trueness [Sch12e].

**Production of accurate gas samples** Another possibility to obtain a good knowledge of the composition of a gas sample is to produce the sample in a well-understood and controllable process. In this case, the calibration trueness depends on the reliability of the production method.

The production of accurate, homogeneous calibration gas mixtures via gravimetric or volumetric methods is described in the ISO standards 6142, 6144 and 6145 [Int01, Int03a, Int03b]. However, for a sample composed of partly tritiated hydrogen isotopologues as required for the LARA calibration, these methods cannot be employed. The main caveats are:

1. **Radioactive decays.** Although tritium can in principle be produced with relatively high purity (> 99%) via cryogenic distillation [Sou86], the produced gas is not stable. In a mixture of all hydrogen isotopologues, the gas composition changes with time due to decays of T to  $^3\text{He}$ .
2. **Radio-chemical reactions.** Interactions of the radioactive isotopologues with the gas recipient's walls, which are usually made from steel, produce impurities such as tritiated methane [Sou86]. Moreover, the  $\beta$ -decay activity of tritium induces a

self-equilibration of the calibration gas mixture [Uda92], so that the composition is changed by reactions such as



3. **Exchange reactions with the vessel walls.** Even in case of long-term bake-out of the steel vessels employed, a certain amount of atomic hydrogen H will remain in the vessel walls. Due to exchange reactions with the isotopologues in the gas mixture, the mole fractions of HT, HD and H<sub>2</sub> increase with time [Fis11].

Moreover, for reasons of safety, miscellaneous restrictions are connected with the handling of tritium and tritiated materials.

As a results, the effects connected to  $\beta$ -decay activity of tritium (items 1. and 2. from above) are the main reasons why the calibration method based on the production of accurate gas samples cannot be used for KATRIN, where tritiated gas samples would be required. Exchange reactions with the vessel walls are a challenge frequently encountered when working with gases and might be considered in a calibration procedure, if only non-radioactive gas samples were used.

### 3.3.2 Theoretical intensities and spectral sensitivity

A different approach to determine the response functions  $R_x$  is based on theoretical calculations of Raman intensities in combination with a measurement of the spectral sensitivity of the Raman system.

As mentioned earlier in this chapter (sections 3.1.4 and 3.2), the response functions depend on the wavelength- and polarization-dependent<sup>6</sup> characteristics of the Raman system employed. Hence, the measured Raman signal amplitudes differ by the spectral sensitivity  $\eta(\lambda)$  of the system from the theoretical values, which are obtained for each  $Q_1$ -branch by summing up the respective theoretical line intensities given by eq. (3.6). The basic idea for the determination of the response functions  $R_x$  by this method is thus to

- calculate the theoretical Raman intensities  $I_x$  for a unit amount ( $N_x = 1$ ) of each of the isotopologues,
- measure the spectral sensitivity  $\eta(\lambda)$  of the LARA system, and
- combine these values in order to obtain the corresponding theoretical relative Raman signal amplitudes  $S_{x,\text{rel}}$ , which are equal to  $R_x$  for  $N_x = 1$  according to eq. (3.14). The calculation of  $S_{x,\text{rel}}$  from  $I_x$  and  $\eta(\lambda)$  will be described in detail in section 4.1.

This calibration approach is in principle suitable for the calibration of the LARA system for all hydrogen isotopologues, as required. In order to apply it, a method for the determination of the spectral sensitivity of the Raman system is needed. Furthermore, the calculation of the theoretical Raman intensities  $I_x$  according to eq. (3.6) requires the knowledge of the line strength function  $\Phi_{p^i,p^s}(\varphi, \theta, a, \gamma)$ . It is a function of the transition tensor

---

<sup>6</sup>The polarization-dependence is not included in the following, since a constant incident polarization is assumed. In the LARA system, this is provided for by a sheet polarizer in the collection optics.

invariants  $a$  and  $\gamma$ , which can be derived from *ab initio* quantum-mechanical calculations and are found in the literature [Sch87]. However, these theoretically predicted values are not experimentally verified, so that their actual trueness is not known at present. Thus, they cannot be employed for the calibration without prior experimental verification.

### 3.3.3 Conclusions

The considerations presented above show that certain challenges are connected to each of the suggested calibration methods:

- The use of a reference method for cross-calibration has to be discarded, since currently no system available at TLK is able to achieve a compositional measurement of tritiated gas mixtures with the required trueness.
- The radioactivity of the required gas mixtures is a major caveat against the accurate production of gas samples. A calibration limited to the non-radioactive isotopologues is feasible, but not sufficient for KATRIN.
- A different approach makes use of theoretical values, which have been calculated but not experimentally verified yet. Thus, no information concerning the trueness of these values is available. If a verification was achieved, however, this method would be suitable for the calibration of all hydrogen isotopologues.

The reasons listed above suggest a combination of the two latter approaches:

All six response functions  $R_x$  are obtained using theoretical Raman signal amplitudes, which combine theoretically calculated line intensities and the spectral sensitivity of the measurement system. By producing and measuring calibration gas samples of accurately known composition, which contain only the stable hydrogen isotopologues  $H_2$ ,  $HD$  and  $D_2$ , three of the six response function can be obtained by a second, independent method. These three response functions can thus be directly experimentally verified in case that both methods agree within the measurement uncertainty. Moreover, a successful verification for the three isotopologues is a strong confirmation of the reliability of the *ab initio* calculations and should thus provide some confidence in the accuracy of the other response functions as well.

The implementation and the results of this combined approach for the KATRIN Raman system are presented and discussed in the following chapters: chapter 4 covers the actual calibration using theoretical Raman signal amplitudes, while the verification via gas samples is discussed in chapter 5.



## Chapter 4

# Calibration based on theoretical Raman signal amplitudes

In this chapter, a calibration method based on a combination of theoretical Raman intensities and the measurement of the spectral sensitivity of the Raman system is investigated. First, the calibration principle is explained in section 4.1. In the following section, the theoretical part of this calibration approach is addressed, before methods for the determination of the spectral sensitivity are presented in section 4.3. Section 4.4 discusses the method of choice, a so-called luminescence standard. Investigations which were carried out to test the applicability of this device to the task at hand are presented in section 4.5. In section 4.6, the results of the application of this method to the different LARA systems are compared. The chapter is summarized in section 4.7.

### 4.1 Calibration principle

In subsection 3.3.2, the calibration approach chosen for the KATRIN laser Raman system was outlined: it is based on a combination of theoretical intensity values, which are calculated according to eq. (3.6), and the spectral sensitivity of the LARA system employed, which is determined experimentally. This approach is explained in more detail in the following:

As discussed in detail in chapter 3, the goal of the calibration is to determine the response function  $R_x$  (or rather  $R_{x,\text{rel}}$ ) for all six hydrogen isotopologues  $x=\text{H}_2$ , HD, D<sub>2</sub>, HT, DT, T<sub>2</sub>. The response function is the proportionality factor which connects the number of molecules of type  $x$  to the corresponding measured Raman signal amplitude  $S_{x,\text{rel}}$  (see eq. (3.14)).

As discussed in section 3.1.4, the peak area of a  $Q_1$ -branch is used as the absolute Raman signal amplitude  $S_x$  in the analysis of a measured Raman spectrum. Note that the  $Q_1$ -branch is composed of multiple lines representing vibrational transitions from different thermally populated initial rotational states; with the given setup, they are not individually resolved. Thus, theoretically treated, the peak area corresponds to a summation of the line intensities  $I_x$  of the individual  $Q_1$ -branch lines as given in eq. (3.6). Additionally,

however, the influence of the measurement system on the resulting spectrum is taken into account, i.e. the spectral sensitivity  $\eta(\lambda)$ :

$$S_x = \sum_J (\eta(\lambda_{x,J}) \cdot I_{x,J}) \quad (4.1)$$

$$= N_x \cdot k_\lambda \lambda_i^{-1} \mathcal{I} \cdot \underbrace{\sum_J \left( \eta(\lambda_{x,J}) \cdot \lambda_{x,J}^{-3} \cdot \Phi_{x,J} \cdot g_N(2J+1) \exp\left(-\frac{E_{v,J}}{kT}\right) / Z_J \right)}_{R'_x}, \quad (4.2)$$

in which  $Z_J$  is the partition function:

$$Z_J = \sum_j \left( g_N \cdot (2j+1) \cdot \exp\left(-\frac{E_{v,j}}{kT}\right) \right). \quad (4.3)$$

Note that the wavelength of the scattered light, formerly called  $\lambda_s$ , is denoted by  $\lambda_{x,J}$  in the expression above, to emphasize the dependence of the line position on the molecule type  $x$  which is scattered from as well as on its rotational state, which is characterized by the quantum number  $J$ .

So instead of deriving the values  $S_x$  from measured spectra, in this calibration approach they are obtained from calculation using theoretical line intensity values. For this reason,  $S_x$  is referred to as the ‘theoretical Raman signal amplitude’. When taking relative Raman signals, the constant part  $k_\lambda \lambda_i^{-1} \mathcal{I}$  cancels out. According to eq. (3.13) and (3.14), the absolute response function is then given by

$$R_x = \frac{R'_x}{\sum_i S_i} \quad (4.4)$$

and the relative one by

$$R_{x,\text{rel}} = \frac{R_x}{R_{\text{mean}}} = n \cdot \frac{R_x}{\sum_i R_i} = n \cdot \frac{R'_x}{\sum_i R'_i} \quad (4.5)$$

$$= n \cdot \frac{\sum_J \left( \eta(\lambda_{x,J}) \cdot \lambda_{x,J}^{-3} \cdot \Phi_{x,J} \cdot g_N(2J+1) \exp\left(-\frac{E_{v,J}}{kT}\right) / Z_J \right)}{\sum_i \left[ \sum_J \left( \eta(\lambda_{i,J}) \cdot \lambda_{i,J}^{-3} \cdot \Phi_{i,J} \cdot g_N(2J+1) \exp\left(-\frac{E_{v,J}}{kT}\right) / Z_J \right) \right]}. \quad (4.6)$$

This is the final formula which is used for the actual calculations. The knowledge of the following quantities is needed for this purpose:

- The LARA system’s spectral sensitivity  $\eta$  as a function of wavelength.
- The properties of the individual lines of each isotopologue’s  $Q_1$ -branch which define their relative intensities: the respective wavelength positions  $\lambda$ , their line strength functions  $\Phi$  and their population factor  $g_N \cdot (2J+1) \cdot \exp\left(-\frac{E}{kT}\right) / Z_J$ .

The spectral sensitivity  $\eta$  is determined experimentally, as will be discussed in section 4.3. The line properties are obtained from theory; this is the topic of the following section.

## 4.2 Theoretical Raman intensities of hydrogen isotopologues

In the last section, the input needed for the calculation of the relative response functions was identified. In the following, the determination of the required Raman line properties from theory will be discussed:

**Line positions of the individual Q<sub>1</sub>-branch lines** The wavelength of a Raman line is calculated from the laser excitation wavelength and the molecule-dependent Raman shift. The latter depends on the energy difference between initial and final state of the Raman transition according to eq. (3.4). For this reason, the determination of the energy levels  $E_J$  of the different rotational levels is required. These values can be found in the literature, as will be addressed below.

**Population factors** Apart from  $E_J$ , also the nuclear spin degeneracies  $g_N$  in the term for the population factor,  $g_N \cdot (2J+1) \cdot \exp\left(-\frac{E_J}{kT}\right)/Z_J$ , can be found in the literature (cf. section 3.1.3). Concerning the temperature  $T$ , a value of 25 °C was chosen for the calculations used in this thesis, as the gas in the Raman cell has approximately room temperature. A more accurate knowledge of the gas temperature is not required; simulations have shown that the difference in the calculated peak area is negligible for realistic temperature variations [Sch12a].

**Line strength function** The line strength function  $\Phi_{p^i, p^s}(\varphi, \theta, a, \gamma)$  depends on the polarization of the incident and scattered beam as well as on the angles under which the light is scattered relative to the incident beam direction. In the case considered here, both incident and scattered light are vertically polarized<sup>1</sup>; the corresponding line strength function is given by [Lon02]

$$\Phi_{p^i, p^s}(\varphi, \theta, a, \gamma) = a^2 \cos^2 \varphi + b^{(2)} \frac{\gamma^2}{45} \cdot (4 - \sin^2 \varphi) , \quad (4.7)$$

where

$$b^{(2)} = \frac{J(J+1)}{(2J-1)(2J+3)} \quad (4.8)$$

is the Placzek-Teller factor for Raman transitions with  $\Delta J = 0$ . A calculation of the total line strength functions according to this formula requires an integration over  $\varphi$ ,  $\theta$  and along the z-direction to include the whole observed scattering region. This is described in detail by Schlösser et al. [Sch12f]. Apart from that, the only input values needed are the transition tensor invariants  $a$  and  $\gamma$ . They are found in the literature, as discussed in the following.

In their paper from 1987, Schwartz and Le Roy presented calculations of wave functions for the ground electronic state of all six hydrogen isotopologues based on *ab initio* potentials [Sch87]. Using these wave functions, they could determine the energy levels  $E_J$  of the individual rovibrational states as well as the transition tensor invariants  $a$  and  $\gamma$  of the corresponding Raman transitions.

---

<sup>1</sup>Actually, Raman scattered light is partly depolarized [Lon02]. In the LARA system, however, only the vertical component is selected for observation by means of a sheet polarizer.

The latter depend not only on  $J$  and the respective isotopologue, but also on the excitation wavelength. The originally published calculations were performed for an excitation wavelength of 488 nm, but were recalculated for our purposes, i.e. for an excitation wavelength of 532 nm [LeR11].

A comparison of the energy levels to experimentally obtained data by Veirs and Rosenblatt showed that the values agree within the measurement uncertainty [Vei87]. The verification of the transition tensor invariants, however, is a less straight-forward task, since a direct experimental determination of these quantities is difficult to realize.

A partial verification can be achieved using depolarization measurements [Jam12b, Sch12f]. The depolarization ratio of Raman scattered light is defined as the ratio between the parallel and the perpendicular polarization components of the scattered light [Lon02]. It depends on the polarizability, which is described by  $a$  and  $\gamma$ . For the  $Q_1$ -branch of hydrogen isotopologues and under  $90^\circ$  observation, for instance, it is given by [Lon02]

$$\frac{3b^{(2)}\gamma^2}{45a^2 + 4b^{(2)}\gamma^2} . \quad (4.9)$$

Obviously, it is not possible to obtain the transition tensor invariants  $a$  and  $\gamma$  separately by measuring depolarization ratios. Nevertheless, measurement results can be used for a comparison with the theoretical prediction of these ratios, which are obtained by using the values for  $a$  and  $\gamma$  calculated by Schwartz and Le Roy [Sch87]. The results of a recent measurement of the depolarization ratios of a number of lines of the  $Q_1$ -branches of all six hydrogen isotopologues agree with the theoretical values to within 5% [Jam12b]. Thus, the depolarization measurements represent indeed a verification of the theoretical values of the transition tensor invariants. However, it should be kept in mind that, while the particular ratio between the two values  $a$  and  $\gamma$  of each individual measured  $Q_1$ -branch line is confirmed, no information is obtained about the correctness of the predicted relative intensities of different lines. This explains the necessity for a verification of the LARA calibration for KATRIN with a second calibration method as suggested in the conclusions of the last chapter (3.3.3).

Nonetheless, the comparison of theoretical values with results from depolarization measurements is of use for the LARA calibration. It can be shown that the relative uncertainty of the measured depolarization ratios, which is  $\leq 5\%$ , represents an upper limit of the relative uncertainty of the respective line strength functions [Sch12h]. Thus, depolarization measurements provide information which in the end is important for the estimation of the LARA calibration uncertainty (see section 4.7).

## 4.3 Methods for the spectral sensitivity determination

As already discussed, the spectral sensitivity represents the wavelength- and polarization-dependent influence of the measuring system itself on the Raman spectrum. In this section, approaches for the determination of this parameter are presented and discussed.

### 4.3.1 Necessity of an experimental approach

An overview of the different LARA system components was given in section 3.2. In principle, the spectral sensitivity of the whole light detection system could be theoretically

calculated; in practice, however, this is impossible. Even if information about the spectral sensitivity was completely available for all components (from theory or given by the manufacturer) and considered as reliable and sufficiently accurate, the overall spectral sensitivity cannot be assumed to be correctly represented by a mere multiplication of the individual values: the total spectral sensitivity depends on such factors as the actual angles and positions of light emission, and effects like changes of the polarization by components or slightly imprecise adjustments can have an unpredictable influence on the resulting spectrum. This is impressively illustrated in figure 4.1, which shows the results of an investigation of the influence of the collection optics' adjustment on the measured Raman signal amplitudes. The investigation was carried out within the scope of the bachelor thesis of S. Mirz [Mir11].

The results demonstrate that the spectral sensitivity can have a large impact on the measurement results. For this reason, it is on no account acceptable to neglect this factor in the calculation of the response functions. Moreover, it becomes clear that the spectral sensitivity has to be determined experimentally for the actual system employed as it stands; even minor changes in the setup like a realignment of components might make a new determination necessary.

### 4.3.2 Principle behind the experimental determination of the spectral sensitivity

The basic principle behind the experimental determination of the spectral sensitivity is simple. The spectral sensitivity quantifies the relative difference between the Raman spectrum  $I_{\text{theo}}(\lambda)$  as produced in the Raman cell on one hand, and the spectrum  $I_{\text{meas}}(\lambda)$  which is actually measured at the end of the detection system on the other hand. So by simply comparing such a pair of spectra, the spectral sensitivity can be determined:

$$\eta(\lambda) = \frac{I_{\text{meas}}(\lambda)}{I_{\text{theo}}(\lambda)}. \quad (4.10)$$

However, this approach obviously requires the knowledge of the spectrum  $I_{\text{theo}}(\lambda)$  produced in the cell. The task is thus to find a light source whose spectrum is accurately known and which can temporarily take the place of the Raman light in the cell.

### 4.3.3 Calibration light source requirements

Possible calibration light sources<sup>2</sup> have to fulfill certain requirements. First of all, the spectral sensitivity determination and thus the light source has to cover all the Raman lines of interest, of course. The  $Q_1$ -branch lines of the six hydrogen isotopologues are found in the range from 612 nm ( $T_2, J''=0$ ) to 683 nm ( $H_2, J''=0$ ) [Sch87].

Apart from that, other aspects have to be taken into account as well. Light which enters the detection system under different initial conditions, e.g. at different angles, might encounter

---

<sup>2</sup>“Calibration light source” is the usual term for light sources used for the determination of the properties of an optical system, e.g. the measured wavelength scale or, like in the case considered here, the spectral sensitivity. For this reason, the term is adopted in the following considerations; note that the term “calibration” used in this context refers only to the spectral sensitivity determination, not to the full LARA calibration procedure.

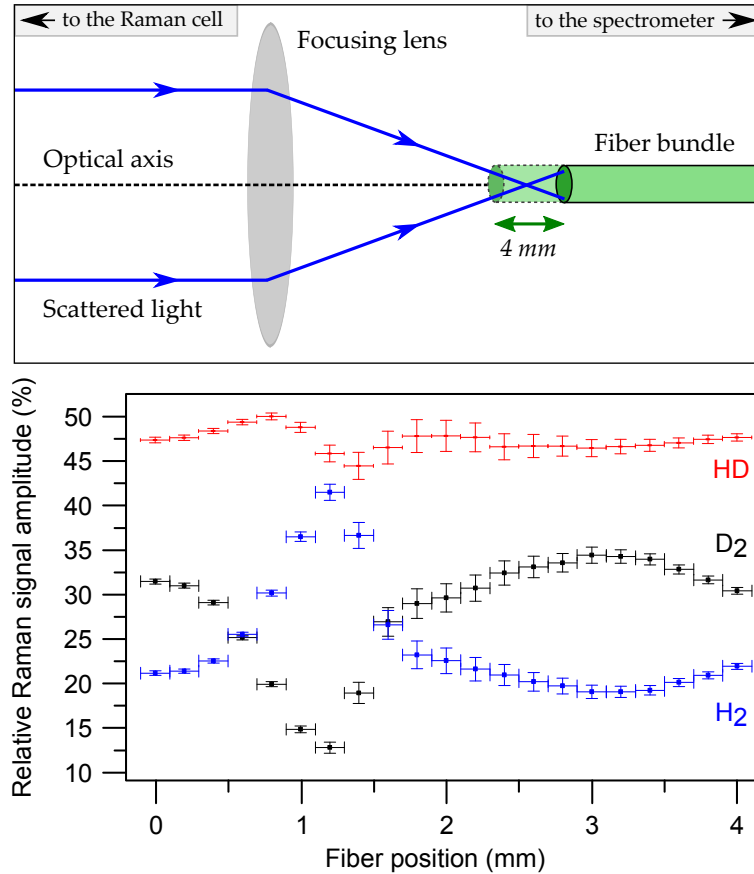


**Figure 4.1: Influence of the fiber position on measured relative Raman signal amplitudes of  $H_2$ , HD and  $D_2$ .** The top panel schematically illustrates the measurement procedure: the fiber end, onto which the Raman scattered light is focused by a lens, is moved along the optical axis in a range of 4 mm. The focal point lies inside this range. The bottom panel shows that the measured relative Raman signal amplitude of the three gases change considerably when the fiber is moved; for  $D_2$  and  $H_2$ , the relative amplitude is reduced by more than half, or doubled, respectively, within 1 mm of fiber movement. The data are taken from S. Mirz's bachelor thesis [Mir11]. As shown there, the effect can be explained by chromatic aberrations, which lead to different focal lengths for the isotopologues' different signals. Note that the measurements were conducted with a LARA setup from 2011, in which the collection lenses were not yet replaced by the achromatic lenses employed in the actual setup.

different spectral sensitivities. Thus, in order to correctly account for the influences of the detection system on the Raman scattered light, the properties of the latter have to be mimicked as closely as possible by the calibration light source with respect to the following aspects:

**Geometry of the scattering region** The Raman scattered light is produced in the Raman cell in a cylindrical volume illuminated by the laser beam, which has a diameter of around 56 to 80  $\mu\text{m}$  [Sch09]. The length of the elongated scattering region which is imaged onto the fiber bundle is 6 mm.

**Position of the scattering region** The focal point of the collection optics is adjusted to collect light coming from the scattering region. The findings discussed earlier in this section indicate that the calibration light source should reproduce the position of the Raman scattering region with submillimeter accuracy, so that the same position relative to the collection optics is achieved.

**Emission angles** Due to the numerical aperture of the fiber in the LARA system, only light emitted with an angle of max.  $12.7^\circ$  to the optical axis of the collection optics is analyzed.

**(Polarization)** Due to the sheet polarizer between the two lenses of the LARA collection optics, only the vertical component of the Raman scattered light is analyzed. For this reason, a replication of the Raman light's polarization distribution is not necessary. However, it is important to ensure that the spectrum of the vertical component indeed represents the calibration spectrum used for the spectral sensitivity determination.

To achieve the described replication of the Raman light, the light of the calibration light source has either to be produced directly at the position of the scattering region or transported there by suitable optics. In the best case, the Raman cell itself can stay in place, so that the contribution of the Raman window to the total spectral sensitivity is correctly taken into account.

#### 4.3.4 Overview of possible calibration light sources

Several possible calibration light sources were considered within the scope of this thesis. The following gives an overview over these possibilities, in which their respective advantages and disadvantages are discussed.

**Calibration light sources outside the scattering region** In most cases, light sources which provide a known spectrum have to be placed in a certain distance to the Raman cell for such reasons as their size, required electrical connections or special handling instructions. In this case, the light has to be transported into the cell by suitable optics. The use of light sources of this type is discussed in the following:

- **Commercially available calibration light sources**

Light sources which provide a spectrum certified by the manufacturer are in most

**Table 4.1: Comparison of commercially available calibration light sources.** (Data taken from [Oce12a, New12, Gam12].)

Product name	Type	$\lambda$ (nm)	Uncertainty	Price	Recalibration
Ocean optics DH-2000-CAL	Deuterium Tungsten Halogen lamp	220 - 1050	$\pm 5\%$	\$ 3925	after 50 h
Newport QTH 63978	Tungsten Ha- logen lamp	300 - 2400	$\approx 2.5\%$	4546 €	recommended after 1 y
Gamma scien- tific RS-10D	Tungsten Ha- logen lamp	300 - 1100 ( $\Delta\lambda=10$ nm)	$\pm 2.5\%$	not avai- lable	after 200 h

cases halogen lamps which are traceable to NIST standards; this is the result of internet research carried out within the scope of this work. A comparison of several such calibration light sources is given in table 4.1. It can be seen that typical uncertainties are found in a range of  $\leq 5\%$ , which is acceptable for the LARA purposes, even if better values are desirable. However, a disadvantage of such calibrated light sources is that calibration data are given for certain wavelength points in coarse intervals only, between which an interpolation is necessary. For the listed examples, the data interval is specified only in one case, where it is 10 nm; this corresponds to a total number of only around eight calibration measurement points in the wavelength range of the six hydrogen isotopologues and thus does not provide very detailed information concerning the differences between individual lines close to each other. Apart from this, calibrated light sources are comparatively expensive and require frequent recalibration, and in some cases the handling of the light source is subject to restrictions due to safety considerations because of the high operating temperature of halogen lamps.

These aspects make commercially available calibration light sources favorable only to a limited extent. Apart from this, it is clear that optics are needed for the transport of light from the source into the Raman cell as well as for the actual replication. The spectral sensitivity of these optics has to be taken into account in the calibration as well. The main difficulty with this type of light source, however, is the necessity to mimic the scattering region in the Raman cell. The question is how well such a like-for-like replication can be achieved with light coming from a source with totally different geometry (see left panel of figure 4.2 as an example for a calibration light source).

- **Stabilized LEDs**

An alternative approach based on LEDs<sup>3</sup> was investigated within the scope of this work. As a semiconductor device, an LED produces a spectrum which is almost entirely dependent on two parameters only: current and temperature [Dav12]. Both can be stabilized using appropriate control mechanisms, thus providing a reproducible spectrum. Note that in contrast to incandescent lamps, LEDs can operate at room temperature, which makes temperature stabilization easier.

---

<sup>3</sup>Light-Emitting Diodes

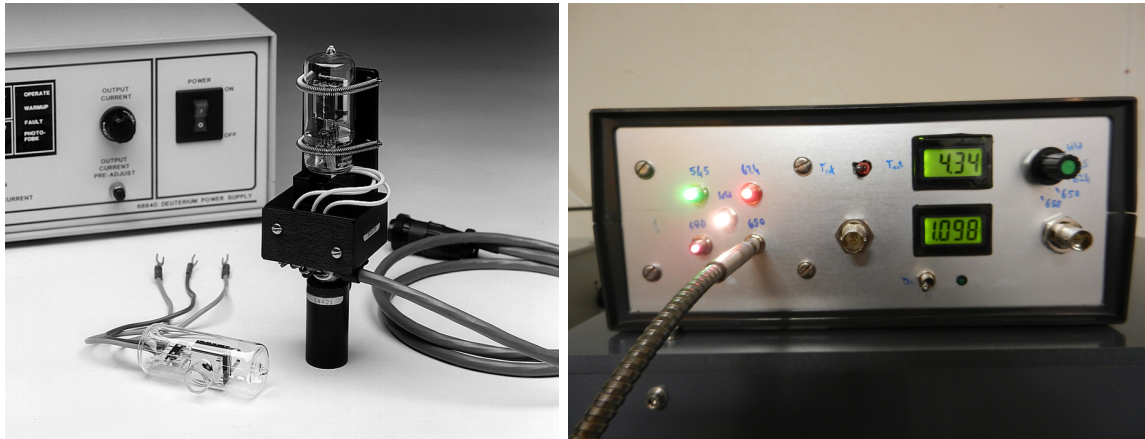


**Figure 4.2: Examples of external calibration light sources.** *Left:* Quartz tungsten halogen calibration light source from Newport, model 63978. (Picture from [New12], courtesy of Newport Corporation.) *Right:* Custom-built LED calibration light source.

The LED spectrum has to be calibrated once. The calibration method developed for this purpose, as well as details of the realization of this approach, are described in appendix C. The optics used for light transport and replication of the scattering region are included in the calibration procedure. Once calibrated itself, the stabilized LED light source can be used as a reproducible calibration light source for the spectral sensitivity determination. Such a custom-built LED light source is considerably cheaper than commercially available calibration light sources.

However, as mentioned above, the replication of the scattering region in the desired way is nontrivial for light sources located in a certain distance to the cell and exhibiting a light-emission geometry differing from the one of the scattering region. Several approaches are discussed in appendix C as well. Especially the task to bring together both the elongated geometry and the desired angular distribution turns out to be demanding. Another issue is the requested accuracy in position, which is further complicated by optics-related effects such as e.g. chromatic aberrations in lenses. The conclusion that can be drawn from these considerations is that the light sources presented above can only be employed with reservation; thus, it is reasonable to consider alternative approaches.

**Calibration light sources at the scattering region** The difficulties described above suggest the use of a light source located in the scattering region itself. Such a light source should produce light directly in the right position, i.e. along the path of the laser beam, and with the desired emission angles. Furthermore, of course, its emission spectrum has to be known. Possibilities for the realization of this approach are discussed below:

- **Black body radiation** This approach has been suggested by M. Schlösser [Sch11a]. The basic principle is the same as the one utilized for incandescent lamps: a filament is heated by a current passing through it, so that light is emitted. This filament is inserted into a Raman cell by replacing the laser windows by electrical feedthroughs, as shown in figure 4.3. Careful positioning ensures that the filament in this calibration cell corresponds accurately to the path of the laser beam in the actual Raman

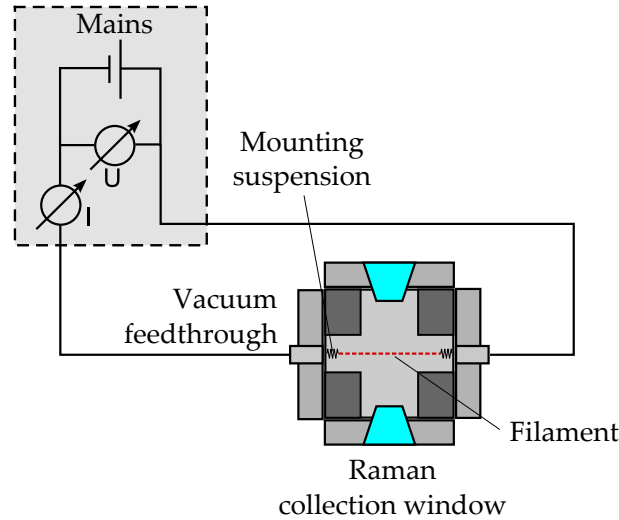


**Figure 4.3: Suggested setup for the spectral sensitivity determination using black body radiation.** (From of [Sch11a].)

cell. The interchange of both cells, which is necessary to switch between calibration and normal operation mode of the Raman system, is possible with good positional reproducibility due to the dovetail cell mounting. Furthermore, black body radiation is isotropic and tungsten filaments, for instance, are available with diameters in the range of the laser beam diameter [Goo12], so that the important parameters of the Raman scattering region, i.e. position, emission angles and position, can in principle be well mimicked. A realization of this approach would require further investigations concerning such issues as suitable filament materials or the evenness of the filament thickness.

In this approach, the knowledge of the emission spectrum is derived from theory. The filament can be described as a non-perfect black body radiator with a certain emissivity  $\epsilon < 1$ , so that according to Planck's law (see e.g. [Mes06]) the shape of its emission spectrum is only dependent on one parameter, the filament temperature. Hence, it is sufficient to control or at least to monitor this parameter in order to obtain the required known calibration spectrum.

Although simple in its functionality principle, the actual realization of this approach is rather difficult. In order to cover the desired wavelength range, the filament temperature has to be at least 2000 K. To measure (or even control) the temperature of a thin filament inside an evacuated or gas-filled cell of limited space with the required accuracy is a very demanding, if not impossible task. For this reason, another approach has been investigated:

- **Luminescent intensity standard** The use of a luminescent intensity standard for the determination of a Raman system's spectral sensitivity was suggested by K. G. Ray and R. L. McCreery in 1997 [Ray97]. Such a luminescence standard is made of a fluorescent material, which emits light when exposed to laser radiation. Thus, when implemented directly into the Raman system, the emission of fluorescence light is induced by the very same laser beam which is responsible for the emission of Raman

light in normal operation mode, by which means an almost optimal replication of the scattering region can be achieved. The output spectrum is obtained by calibrating the standard once against a known calibration light source.

The last-mentioned approach overcomes many of the difficulties encountered with other calibration light sources as discussed above. Therefore, this approach was chosen for the LARA calibration. Advantages and challenges of this approach are discussed in more detail in the following sections.

## 4.4 Use of a luminescence standard as calibration light source

### 4.4.1 Description of the luminescence standard SRM 2242

A luminescent intensity standard, as highlighted at the end of the last section, has been developed by the National Institute of Standards and Technology (NIST) and is distributed under the name Standard Reference Material (SRM) 2242. It is documented in [Cho07, NIS08], on which the following description is based.

SRM 2242 consists of a glass slide with a size of approximately 30.4 mm x 10.7 mm x 2.0 mm; it is shown in figure 4.4. The glass is a borate matrix glass, in which a MnO<sub>2</sub> doping represents the actual luminescent constituent. One surface of the glass slide is frosted in order to minimize the dependence of the luminescence light's spectral shape on the position of the standard relative to the collection optics. The standard has been developed and is certified explicitly for a laser excitation of 532 nm.

The luminescence spectrum of SRM 2242 was calibrated by NIST using (i) a neon emission pen lamp for the wavelength calibration (x-axis), and (ii) a NIST-calibrated white-light, uniform-source, integrating sphere for the relative spectral intensity calibration (y-axis). The shape of the resulting spectrum is described by a fifth-order polynomial:

$$I_{\text{SRM}}(\lambda) = \frac{10^7}{\lambda^2} \cdot \left( A_0 + A_1 Z^1 + A_2 Z^2 + A_3 Z^3 + A_4 Z^4 + A_5 Z^5 \right) \quad (4.11)$$

with

$$Z = 10^7 \cdot \left( \frac{1}{\lambda_i} - \frac{1}{\lambda} \right) . \quad (4.12)$$



**Figure 4.4:** The luminescence standard SRM 2242. The actual glass slide is delivered in an optical mount, as can be seen here. For the use in the LARA setup, this mount is replaced by a custom one.

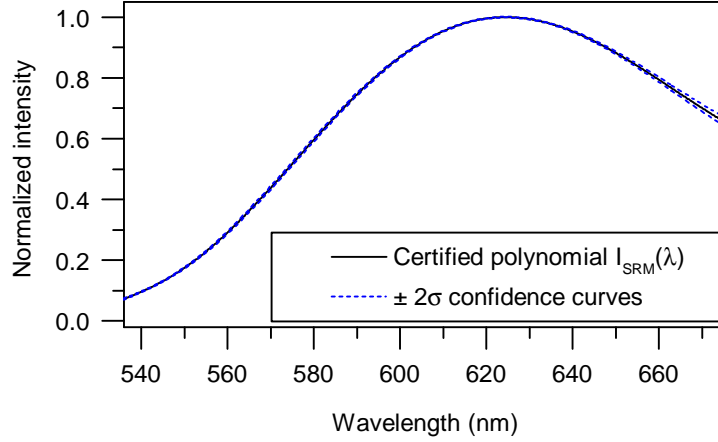


**Figure 4.5: Certified polynomial and 95% confidence curves for SRM 2242.** The x-axis represents the wavelength range for which the polynomial is certified. The y-axis is on a relative scale; it is normalized to unity with the dimension of  $\frac{\text{photons}}{\text{s}\cdot\text{cm}^{-2}\cdot\text{nm}}$ . (According to [NIS08].)

In these expressions,  $I_{\text{SRM}}(\lambda)$  is the certified relative spectral intensity of SRM 2242, the  $A_n$  are the polynomial coefficients provided by NIST,  $\lambda_i$  is the incident laser wavelength in nm and  $\lambda$  the wavelength in nm. The expression is certified for wavelengths between 536.4 to 676.1 nm and temperatures between 20 and 25 °C. The expanded uncertainty [Joi93] (95% C.L.) of the certified expression is provided by NIST as a fifth-order polynomial as well. The spectrum and the corresponding 95% confidence curves ( $2\sigma$ ) are shown in figure 4.5.

Using this luminescence standard, the spectral sensitivity of a Raman system is obtained according to eq. (4.10):

$$\eta(\lambda) = \frac{I_{\text{meas}}(\lambda)}{I_{\text{theo}}(\lambda)}. \quad (4.13)$$

In this case,  $I_{\text{theo}} = I_{\text{SRM}}$  is the certified SRM spectrum given by the polynomial from eq. (4.11), and  $I_{\text{meas}}(\lambda)$  is the luminescence spectrum which is measured by the Raman system when the standard is placed into the laser beam at the position of the Raman cell.

#### 4.4.2 Advantages of the use of SRM 2242 for LARA

For the spectral sensitivity determination of the LARA system for KATRIN, the use of SRM 2242 is an advantageous approach for several reasons:

- As briefly discussed in the overview of possible calibration light sources (4.3.4), a luminescent standard offers an almost perfect replication of the scattering region with respect to position and geometry. This is due to the fact that the luminescence light and the Raman scattered light are produced by the same laser beam at the same position, as shown in figure 4.6.

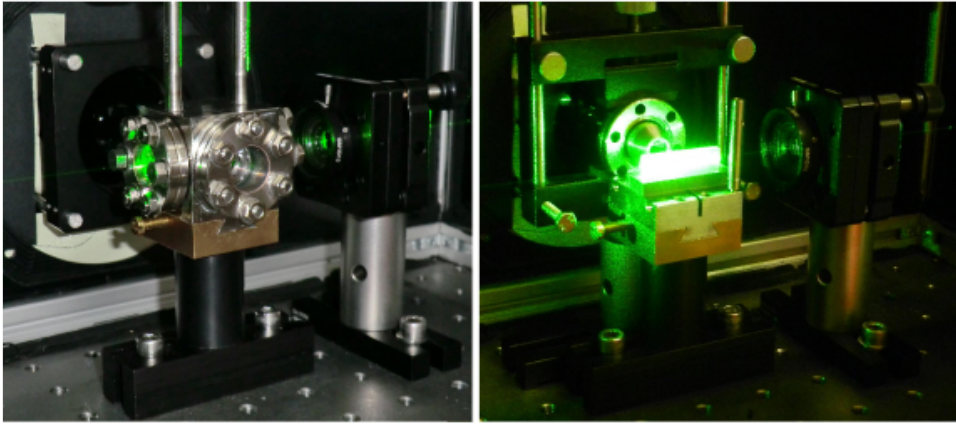


**Figure 4.6: Replication of the scattering region by SRM 2242.** *Left panel:* Raman measurement. In this case, Raman light is produced along the laser beam due to scattering of the laser light from the gas molecules in the Raman cell. *Right panel:* Calibration measurement. The cell is replaced by the luminescence standard, while the laser beam stays unchanged. Thus, luminescence light is produced in the same region as the Raman light in operation mode due to the excitation of the SRM 2242 material by the laser light. Note that the green light visible in both pictures is Rayleigh scattered light with the incident laser wavelength. Both Raman light and luminescence light are much fainter and cannot be seen here.

- In the certificate of analysis of SRM 2242, NIST states that “careful measurements of the glass have shown it to be spatially homogeneous in spectral luminescence” [NIS08]. Thus, both Raman light and luminescence light originate from an approximately isotropic medium excited by linearly polarized light, leading to emission in the form of a dipole radiation pattern in both cases [Feo61, Boy08]. For this reason, the angular distribution of the Raman scattered light and of the luminescence light can be assumed to be nearly equal.
- In contrast to other available calibration light sources, the spectral shape is given as a polynomial, i.e. as a continuous curve, and not in terms of discrete measurement points. For this reason, an interpolation which would lead to higher uncertainties is not necessary.
- The expanded relative uncertainty ( $2\sigma$ ) is better than 1% in the part of the certified range in which the  $Q_1$ -branches of T<sub>2</sub>, DT, D<sub>2</sub>, HT and HD are located<sup>4</sup> [NIS08]. This is far better than the uncertainties of most other calibration light sources available<sup>5</sup>; moreover, since SRM 2242 allows a direct determination of the spectral sensitivity without the need to employ further optics, no additional uncertainty is introduced.
- SRM 2242 is compact and simple to implement into the LARA setup. It is possible to

<sup>4</sup>The  $Q_1$ -branch of H<sub>2</sub> lies just outside the certified range. This will be discussed in detail in the next subsection (4.4.3)

<sup>5</sup>Note that the uncertainties given in table 4.1 are most likely given on the  $1\sigma$  level only, since not stated otherwise in the data sheets of the light sources.

attach its mount to a dovetail which allows to easily switch between Raman cell and SRM 2242. Thus, the spectral sensitivity measurements necessary for an occasional recalibration of the LARA system between individual KATRIN measurement runs can be carried out by a non-specialist.

- In contrast to most other calibration light sources, SRM 2242 does not require any electronics; a reliable output spectrum is produced without the need to stabilize such parameters as voltages or temperatures with much effort.
- As a simple glass slide, SRM 2242 has in principle no limited lifetime like a halogen lamp, for instance. The certification is currently stated to be valid until 01 January 2014 [NIS08]; however, there is the possibility that the certification period might be extended, as has happened before. Besides, with a price of currently below \$ 1500 [Oce12b], even a new acquisition of SRM 2242 would be comparatively inexpensive.

### 4.4.3 Challenges connected to the use of SRM 2242 for LARA

The last subsection showed that SRM 2242 has many advantages with respect to the LARA requirements. However, there are also some suboptimal properties of this device which have to be addressed.

**Limits of the certified wavelength region** The certification of the polynomial is valid between 536.4 to 676.1 nm [NIS08]. The  $Q_1$ -branch of  $H_2$ , however, is found at a wavelength  $\sim 683.3$  nm and thus lies just outside the certified range. Although it was not included in the certification, in additional studies by NIST the luminescence of SRM 2242 was measured in an extended range up to 848.1 nm. These data were provided by NIST [Cho12]; they are shown in figure 4.7 together with the certified polynomial. No uncertainty was given for these data.

In the calculation of a LARA system's spectral sensitivity, these extended range data can, though uncertified, be used as a measure for the SRM luminescence spectrum at the  $Q_1$ -branch line positions of  $H_2$ . An extrapolation of the  $2\sigma$  confidence curves allows an estimation of the associated uncertainties, as illustrated in figure 4.8. These confidence curves are connected - amongst others - to the difference between polynomial curve and actual measurement curve and accordingly start to diverge increasingly outside the certified range, where the polynomial does not any longer represent a good description of the measurement data. For this reason, the extrapolated uncertainty of the polynomial is assumed to represent a rather conservative estimate for the uncertainty of the actual measurement curve.

When evaluating spectra, it should be kept in mind that the  $H_2$  value of the thus obtained spectral sensitivity is less reliable than that of the other isotopologues due to the missing certification. For the use for KATRIN, however, this is not critical, since  $H_2$  is assumed to be just a minor constituent of the source gas ( $< 1\%$ ) [KAT05].

**Differences in the Raman setup** A second point which has to be carefully considered concerns differences between the LARA system and the Raman setup which was used for

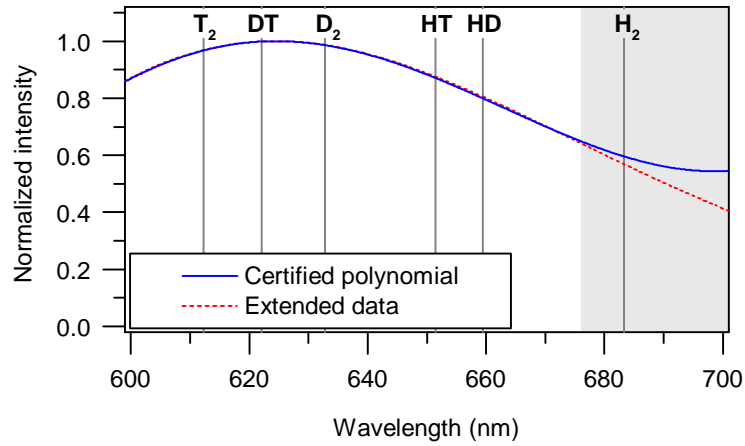


**Figure 4.7: Coverage of the  $Q_1$ -branches by the SRM 2242 certification.** The vertical lines indicate the positions of the respective  $Q_1(J'' = 0)$  lines of the individual hydrogen isotopologues. The gray area marks the extended wavelength range in which the NIST certification of the polynomial (blue solid line) is not valid. In this range, the polynomial starts to differ considerably from the measured values (extended range data, red dotted line). (According to [NIS08, Cho12].)

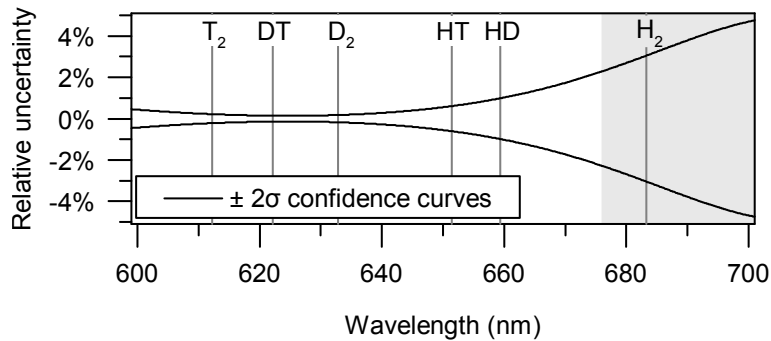


**Figure 4.8: Relative uncertainty of the SRM luminescence spectrum, extrapolated to the uncertified range.** The expanded relative uncertainty is better than 1% for the  $Q_1$ -branch lines of all isotopologues covered by the certification. The entire curves, including the parts in the gray area, i.e. outside the certified range, were calculated using the fifth-order polynomials which describe the SRM spectrum and uncertainties in the certified region. The extrapolation of the certified curves to the uncertified range serves as an estimation for the expanded uncertainty of the  $H_2$   $Q_1$ -branch. For the  $J'' = 0$  line, which is the line with the longest wavelength in this branch, a value of 3% is obtained this way. (According to [NIS08].)

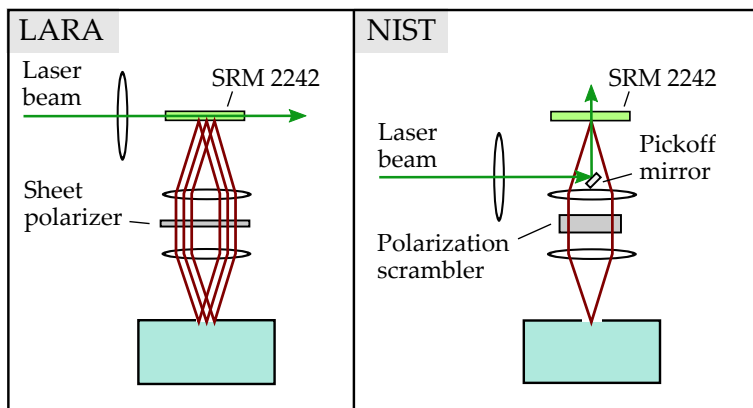


**Figure 4.9: Differences between the Raman setups (schematic).** *Left panel:* LARA setup with SRM 2242 at the Raman cell position. The luminescence light is produced along the laser beam passing through the SRM glass slide, and collected at an angle of  $90^\circ$  to the beam direction. A sheet polarizer in the collection optics allows only vertically polarized light to pass. The minimal beam diameter of the focused laser beam in the scattering region is  $56.4\text{ nm}$  [Sch09]. The length of the observed region is  $6\text{ mm}$ . *Right panel:* Setup used by NIST for the SRM certification measurements (according to [Cho07]). A  $180^\circ$  backscattering geometry is used, in which the laser beam is directed onto the luminescence standard by a small pickoff mirror. In different measurements, the laser beam is (i) focused onto SRM 2242 by a cylindrical lens to obtain a  $80\text{ }\mu\text{m} \times 4\text{ mm}$  line focus, (ii) focused by a  $300\text{ mm}$  spherical lens to obtain an approximately  $80\text{ }\mu\text{m}$  diameter spot, or (iii) left unfocused, which results in an spot of around  $2\text{ mm}$  diameter on the luminescence standard. A polarization scrambler is employed. Note that only parts relevant for the discussion are shown. Other components present in the light path are left out for reasons of clarity. The blue box represents the spectrometer and CCD-detector section.

the certification measurements by NIST. As illustrated in figure 4.9, two differences which might have an influence on the validity of the certified spectrum have been identified:

- **The scattering geometry**

As already mentioned in the description of the system in section 3.2, Raman scattered light is collected at an angle of  $90^\circ$  to the direction of the incident laser beam. In the NIST certificate of analysis, such a setup is not explicitly excluded from the certification; however, it is stated that all certification measurements were taken in a  $180^\circ$  backscattering geometry [NIS08]. That this geometry is apparently considered as the “standard” geometry is emphasized by the fact that the mount provided by NIST (see figure 4.4) is designed for backscattering experiments; it is not applicable for  $90^\circ$  measurements. Furthermore, the following instructions for use are given in the certificate:

“It is important that the laser excitation be incident only on the frosted surface of the glass. The shape of the spectral luminescence will have some sensitivity to the placement of the glass surface relative to the collection optics of the spectrometer, which is minimized by scattering from the frosted surface.” [NIS08]

In a  $90^\circ$  geometry, however, there is more than one surface involved in the scattering

process, since the surface which the laser excitation is incident on is not identical to the one the collected luminescence light comes from. Additionally, it should be noted that in the case of backscattering measurements, light emission is produced by laser light being focused onto the aforementioned frosted surface as a line or spot, while in the LARA system the light originates from the passage of the laser beam through the SRM glass slide. These are measurement conditions under which SRM 2242 was not tested by NIST. In order to use the luminescence standard for the LARA calibration, it has thus to be ensured that the certified spectrum is valid nonetheless.

- **Handling of polarization effects**

In the section about requirements of possible calibration light sources, 4.3.3, the necessity of a good replication of the scattering region was discussed: the spectral sensitivity is to some extent dependent on the state of the light entering the detection system. Concerning the polarization of the light, a sheet polarizer in the LARA system's collection optics ensures that only one polarization component can pass, regardless of the source of the light (Raman scattering or luminescence). NIST chooses a different way to handle possible differences between the polarizations of Raman and SRM luminescence light; the instructions for use given in the SRM 2242 certificate of analysis request the use of a polarization scrambler:

“Due to polarization effects that are present in Raman instrumentation, a polarization scrambler should be employed in the Raman light-collection optics, most preferably in a region of collimated light. Raman spectral bands that exhibit various degrees of polarization will not be properly intensity-corrected without the use of a scrambler.” [NIS08]

NIST used an achromatic depolarizer (DPU-25, Optics for Research, [www.ofr.com](http://www.ofr.com)) as polarization scrambler, which converts a polarized beam of light into a pseudo-random polarized beam by producing a spatial variation in the polarization [Tho12a]. The desired effect is reached with both approaches, polarization scrambler as well as sheet polarizer: the same state of polarization enters the detection system for both Raman scattered light and SRM luminescence light. However, to employ a sheet polarizer means to select only light with a certain property out of the entire emitted light; it cannot be taken for granted that the resulting spectrum still be equal to the NIST-certified one, which takes the total luminescence light into account.

Yet the use of a polarization scrambler in the LARA system is no option, since the sheet polarizer serves another purpose as well: the polarizations of both incident and scattered light have to be clearly defined in order to be able to choose the right line strength function for the calculation of the response functions (see section 4.2).

These considerations show the necessity to investigate possible changes in the shape of the luminescence spectrum due to effects related e.g. to the different scattering geometry or the use of a polarizer. This is the topic of the next section.

## 4.5 Investigation of the applicability of SRM 2242 to KATRIN

In order to use SRM 2242 for the LARA calibration, it has to be ensured that the certified spectrum is valid under the conditions present in the setup. A range of investigations was carried out for this purpose. In these investigations, initial parameters such as the laser polarization were changed and the resulting spectra compared to each other in order to find out if the spectral shape had changed. It is important to keep in mind that in case of deviating spectral shapes, these investigations cannot determine which of the spectra - if any - is the “right” one, i.e. which of the initial parameters leads to the spectrum certified by NIST; this is of course an intrinsic feature of these measurements due to the unknown spectral sensitivity of the system. Nevertheless, the measurements can give an indication if the assumption made for the spectral sensitivity determination, i.e. that the certified spectral shape is valid even under conditions differing from the ones at NIST, is reasonable; this may be concluded if no change in spectral shape is observed for different initial parameters.

**General measurement setup and treatment of spectra** All the measurements described in the following were taken with the LARA 1 system. The luminescence standard was placed in the Raman cell position using a custom-made mount, which again was placed on top of a dovetail that provides for the connection to the Raman cell mounting (see figure 4.6). The wavelength axis was calibrated with a Pb(Ne) spectral lamp. All measurements were taken with a laser power of 300 mW and the CCD-detector gain 3, unless stated otherwise; the CCD-detector read-out speed was 100 kHz in each case. The acquisition time was between 0.01 s and 3 s for each spectrum. For each parameter setting, a number of spectra (5 – 150) were taken.

The acquired spectra were treated using the open-source spectral analysis software described in [Jam12a]. In this process, dead pixels and cosmic rays were removed and the spectra were corrected for astigmatism. The background was removed<sup>6</sup> by subtracting the mean value of 100 dark spectra taken for each measurement series with the same acquisition settings as the SRM spectra.

For each individual parameter setting, the respective set of spectra was averaged to minimize the influence of random fluctuations. Then a Savitzky-Golay smoothing filter (polynomial order 2, 20 side-points) was employed for further noise reduction, unless stated otherwise. This was done to obtain a better estimation of the maximum intensity value of each curve: in order to make a comparison possible, all spectra were normalized by dividing them by their respective maximum intensity. In this way, differences in the spectral shape become visible. The term ‘relative intensity difference’, which is frequently used in the following, therefore always refers to the relative difference between two normalized spectra and is used as a measure for deviations in the spectral shape; the difference between absolute intensities is of no interest for this feasibility study.

---

<sup>6</sup>Note that a correct background removal is crucial for measurements in which relative intensities are of interest. For each pixel, the background adds a certain additional intensity value to the actual Raman or luminescence intensity value and thus changes the spectral shape, i.e. the relative intensities of the different points.

### 4.5.1 Influence of the incident position of the laser beam on the spectral shape

The different scattering geometries of the NIST and the LARA setup were discussed in section 4.4.3. In order to mimic the Raman scattering region along the laser beam in the LARA system, the laser beam is intended to pass longitudinally through SRM 2242, as illustrated in figure 4.10(a). Thus, compared to the NIST setup, the laser beam is incident onto a different surface, and the luminescence light is observed under a different angle relative to the laser beam. For this reason, the dependence of the measured spectral shape on different positions and angles of the incident laser beam was investigated experimentally.

The main goal was to find out if there are reasons against the use of said parallel alignment to achieve a good replication of the scattering region, e.g. indications that the spectrum is not reproducible under these conditions. Alternatively, a replication of the Raman scattering region could be achieved by sending the laser beam under a shallow angle<sup>7</sup> onto the front or back side of the luminescence standard (cf. figure 4.10(b<sub>2</sub>), (b<sub>3</sub>)).

**Measurement setup** During the measurements, the entire LARA system remained unchanged; in particular, the position of the laser beam was always the same. The only thing which was varied was the position of the luminescence standard. By this means, different incident positions of the laser beam with respect to the SRM surfaces could be tested for their influence on the measured spectral shape. Measurements were taken with the following settings:

1. **Parallel beam:** In a first series of measurements, the luminescence standard was aligned parallel to the laser beam with the frosted side facing the collection optics, as shown in figure 4.10(b<sub>1</sub>). By carefully translating the standard perpendicular to the laser beam, three different positions for the point of incidence on the side surface were chosen: a position close to the frosted front surface, a position in the center of the side surface and a position close to the back surface or the approximately 2 mm thick glass slide (see figure 4.10(c)). For each position setting, 100 spectra were taken with an acquisition time of 1 s each.
2. **Incidence on the front:** In a second test series, the luminescence standard was rotated counterclockwise around the vertical axis going through its center, in angles of  $\alpha = 5^\circ, 10^\circ, 20^\circ, 30^\circ, 45^\circ$  and  $60^\circ$  to the laser beam (see figure 4.10(b<sub>2</sub>)). The beam was thus incident on the frosted front surface. For each angular setting, 30 spectra were taken with an acquisition time of 0.1 s each.
3. **Incidence on the back:** Afterwards, the luminescence standard was rotated clockwise around the same axis, in angles of  $\beta = 5^\circ, 10^\circ, 20^\circ, 30^\circ, 45^\circ$  and  $60^\circ$  to the laser beam (see figure 4.10(b<sub>3</sub>)). The beam was thus incident on the back surface. For each angular setting, 30 spectra were taken with an acquisition time of 0.1 s each.

---

<sup>7</sup>The part of the scattering region from which light is collected in LARA measurements is 6 mm long. In order to obtain light emission over this length in the 2 mm thick luminescence standard, the laser has to be incident on the glass slide in an angle of  $20^\circ$  or less (cf. figure 4.10(b<sub>2</sub>), (b<sub>3</sub>)).

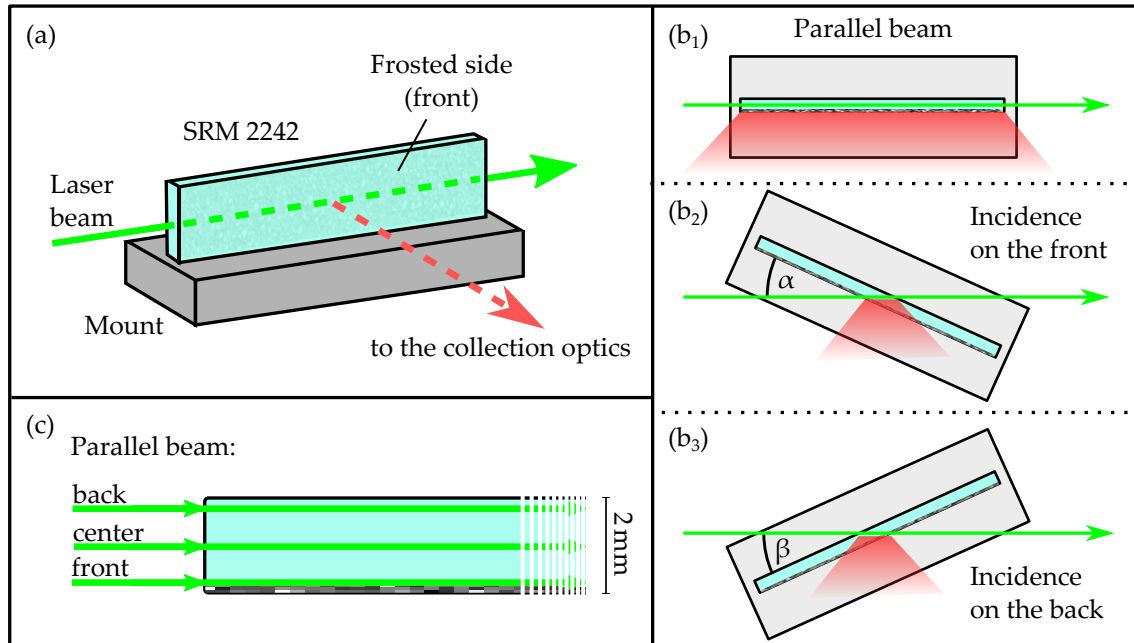


**Figure 4.10: Different incident positions of the laser beam on SRM 2242.** (a) Setup planned for the calibration measurements: SRM 2242 is aligned parallel to the laser beam. The laser beam is incident on the small side of SRM 2242, hence passing through the full length of the glass slide. (b<sub>*i*</sub>) Different incident angles of the laser beam (top view). Note that  $\alpha$  and  $\beta$  denote the respective smallest angle between laser beam and luminescence standard. (c) Different incident positions of the parallel beam (top view).

Note that in configurations 2. and 3., the intersection of laser beam and luminescence standard and hence the size of the light emission region decreased with increasing angle of rotation.

**Results** The resulting averaged and normalized spectra for the different settings are shown in figure 4.11. Two features are noticeable:

- (1) In the wavelength region below approximately 575 nm, the spectra obtained for scattering from the front surface exhibit peak-like structures which are not present in the other spectra. These structures were identified as Raman peaks of  $\text{SiO}_2$  (cf. [Sch09]), arising probably from Raman scattering of diffusely reflected laser light in the LARA system's fiber bundle. In the cases where the laser is not incident on the front surface, this is strongly suppressed because almost no directly reflected light reaches the fiber. These features are irrelevant for the spectral sensitivity determination since they lie outside the wavelength range of the  $Q_1$ -branches of the hydrogen isotopologues.
- (2) A zoom shows that most curves are close to each other, but a certain gap is observable between the spectra obtained for small angles ( $\alpha = 5^\circ\text{--}30^\circ$ ) at front incidence (shaded area) and the other spectra.

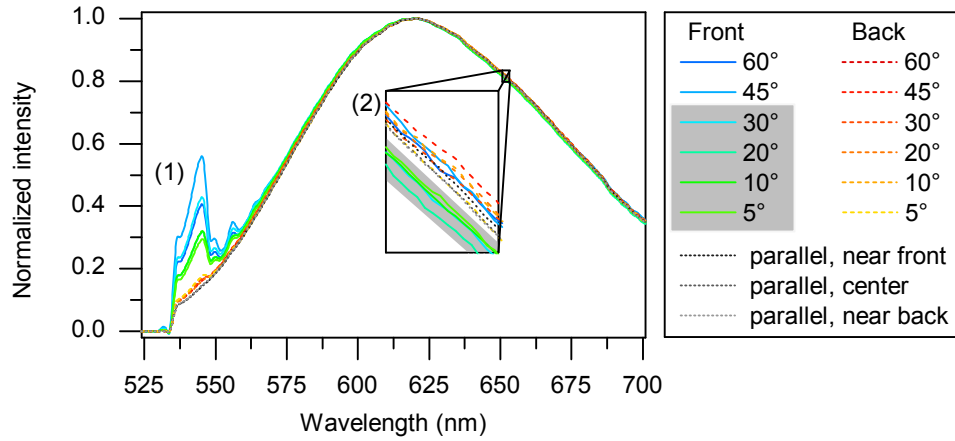


**Figure 4.11: Measured spectra for all incident laser positions and angles.** The features denoted with (1) and (2) are discussed in the main text. The sudden intensity drop at around 536 nm is due to the edge filter. The zoom at (2) shows a wavelength range of 2 nm around the HT peak position at approximately 651 nm. The shaded area is discussed in the main text.

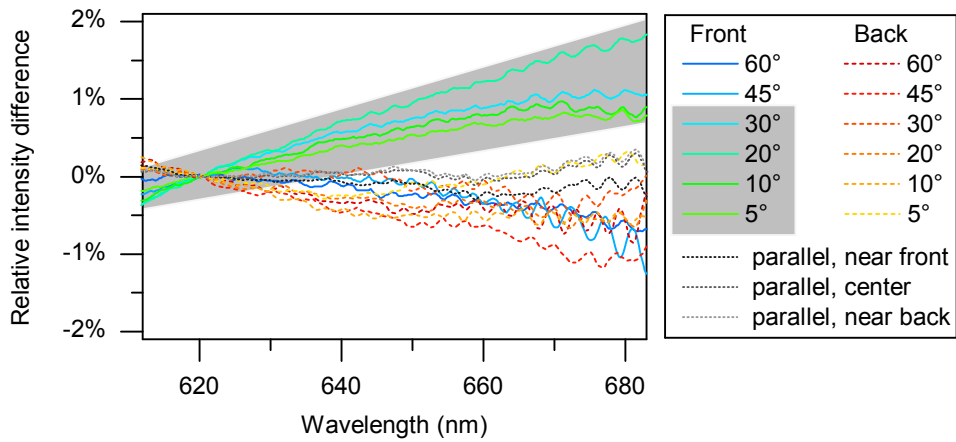


**Figure 4.12: Comparison of the spectral shapes for all incident laser positions and angles.** The plot shows the relative intensity differences between the individual spectra shown in figure 4.11 and their average spectrum. The shaded areas mark the spectra obtained for a shallow angle of incidence on the front surface, which exhibit a different trend than the other curves (see also main text).

Figure 4.12 shows a comparison of the spectral shapes of all measurements for the whole wavelength range of relevance. Here, the relative difference of each spectrum to the average of all spectra is used as a measure for differences in spectral shape. The effect observed in (2) manifests itself in form of a clear difference between the trend of the shapes of the ‘shallow front incidence’ spectra (shaded in the plot) on the one hand, and the remaining spectra on the other hand. In the range between 612 nm and 683 nm, in which the  $Q_1$ -branches of the hydrogen isotopologues are located, the maximum difference observed between two measured curves is around 3.1%, while all curves outside the shaded area agree within 1.5%.

**Discussion** With respect to the measurement setup used by NIST, the measurement with incidence on the frosted front surface at  $60^\circ$  is closest to the original conditions, i.e. incidence on the frosted surface at an angle of  $90^\circ$ . The fact that almost all measurements exhibit a trend similar to this one, despite their different incident positions and angles, is an indication that these spectra can be considered as ‘reliable’. This means that the NIST-certified spectrum can be applied in these cases with reasonable confidence. According to the discussions from section 4.3.3, deviations in spectral sensitivity are expected for light entering the detection system under differing conditions, as is the case here; this is the most probable reason for the observed variations in the measured spectral shape.

In contrast, the deviation of the spectra obtained for small angles ( $\leq 30^\circ$ ) and incidence on the front surface (shaded in the plots) supposedly originates from an unfavorable effect related to the comparatively shallow incidence on the frosting; this is suggested by the fact that no such deviation is observed for the same angles when the laser is incident on the non-frosted back surface instead. For this reason, it is not considered advisable to use the spectrum obtained for a shallow incidence on the front surface for the determination of the spectral sensitivity.

A comparison of the spectra obtained for parallel alignment and those obtained for an incidence of  $\leq 20^\circ$  on the back surface can show if the scattering region is comparably well mimicked in both cases. In this case, no difference in spectral shape should be observed. In figure 4.13, the maximum deviation between the respective spectral shapes is shown. It can be seen that the difference exceeds the confidence curves given by NIST in parts of the wavelength range, which indicates a systematic effect rather than a random fluctuation. This suggests that the replication of the scattering region is not equally good in both cases. Differences might be due to the following aspects:

1. In the case of parallel alignment, the laser beam enters and exits the glass slide at the small side at an angle of  $90^\circ$  to the surface. In the case of incidence on the back, in contrast, two transitions between air and glass slide close to the observed scattering region occur: the entrance of the beam into the glass slide on the unfrosted back surface as well as the exit on the frosted front surface, both at shallow angles (cf. figure 4.10(b<sub>3</sub>)).

In the first case, i.e. for parallel alignment, the beam is generally back-reflected to the same path. For non-parallel alignment, however, the shallow exit angle might lead to reflections of the laser beam in different directions inside the glass slide. These reflections might produce additional luminescence light at positions other than along the laser beam path and thus outside the actual Raman scattering region.

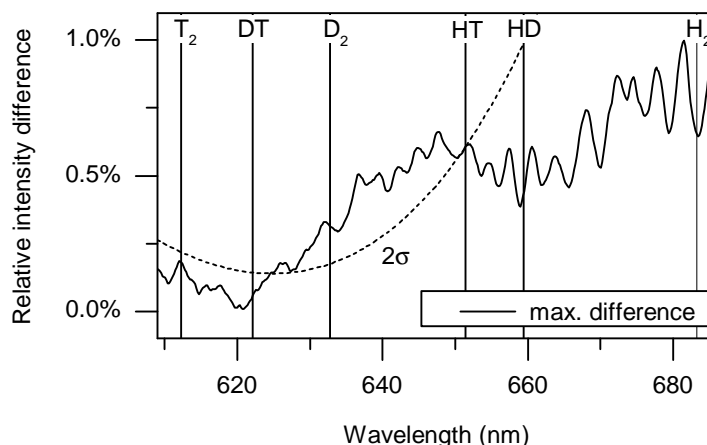


**Figure 4.13:** Maximum relative intensity difference between the spectra obtained for parallel alignment and the ones obtained for incidence on the back surface. The maximum deviation was calculated for each point by subtracting the respective smallest from the largest value among the six curves (parallel incidence: front, center, back; back incidence: 5°, 10°, 20°).

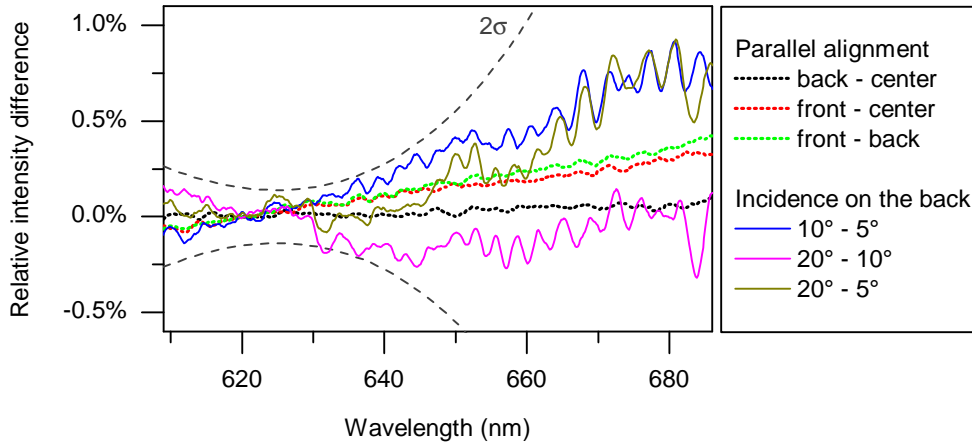
2. In the case of parallel alignment, the front surface of the luminescence standard is symmetrical with respect to the collection optics. In the case of incidence on the back, however, this is not the case: according to figure 4.10(b), bottom panel, luminescence light produced left (right) from the center leaves the glass slide at a position in a smaller (greater) distance to the collection optics.

Figure 4.14 shows the relative intensity differences between the individual measurements within each of the two measurement sets (parallel alignment and incidence on the back). It can be seen that the differences in spectral shape between the measurements with different ‘back incidence’ angles are much larger and more irregular than the ones obtained for the different ‘parallel alignment’ settings. This indicates a better reproducibility of the latter spectra.

**Conclusions** From these considerations concerning possible reflections, symmetry and reproducibility, it is suggestive that the parallel alignment provides the best replication of the scattering region. In this case, the laser beam passes through always the same uniform medium over a length comparable to the length of a Raman cell. Thus, the situation is very similar to the one present in Raman measurements, where the laser beam passes through a uniform gas volume.

For these reasons, the setting with parallel alignment is chosen for the actual measurements for the spectral sensitivity determination. From the results shown in figure 4.14, where the deviations between the individual positions of incidence at parallel alignment are very well within the  $2\sigma$  confidence curve, it can be concluded that an exact positioning of the parallel SRM 2242 is not critical.

A final confirmation that the results for the spectral sensitivity obtained under these conditions are correct, despite the differences in geometry compared to the one used by



**Figure 4.14: Relative intensity differences within the respective measurement sets of parallel alignment and incidence on the back.** The broad lines show the relative intensity differences between each two of the three position settings for parallel alignment (cf. figure 4.10(c)). The thin lines represent the corresponding curves for incidence on the back, where the different positions are defined by their angle of incidence ( $5^\circ$ ,  $10^\circ$ ,  $20^\circ$ ).

NIST, can be obtained by cross-checks and verification measurements. These are described in section 4.6 and in the following chapter.

#### 4.5.2 Influence of polarization on the spectral shape

**Measurement setup** Two sets of measurements were performed in order to investigate polarization-related effects on the spectral shape.

In the first measurement, a half-wave plate was used to change the polarization of the laser beam incident on the luminescence standard. The half-wave plate was inserted into the LARA system in the region of collimated light behind the Glan-Taylor polarizer (see figure 3.6 in section 3.2). It was rotated<sup>8</sup> from  $0^\circ$  to  $360^\circ$  in steps of  $1^\circ$ . For each angular setting, five spectra were taken with an acquisition time of 1 s each. During the measurement, the sheet polarizer in the collection optics was employed in normal LARA operation mode, i.e. only vertically polarized light could enter the detection system.

In the second measurement, the sheet polarizer in the collection optics was rotated to change the polarization component which enters the detection system. It was rotated from  $0^\circ$  to  $360^\circ$  in steps of  $2.5^\circ$ , again with five spectra per step and  $t_{\text{acq}}=1$  s. The incident laser beam was vertically polarized during this measurement.

**Results** The dependence of the measured spectra on the incident laser polarization and the detected polarization component is shown in figure 4.15. The two measurements exhibit individual characteristics; the change in relative intensity difference with wavelength as well as with polarization is much more regular for the case in which the laser polarization

<sup>8</sup>Note that the rotation of a half-wave plate by a certain angle  $\phi$  rotates the polarization by an angle of  $2\phi$ . Thus, a change in laser polarization from vertical to horizontal is achieved by a  $45^\circ$  rotation of the half-wave plate.

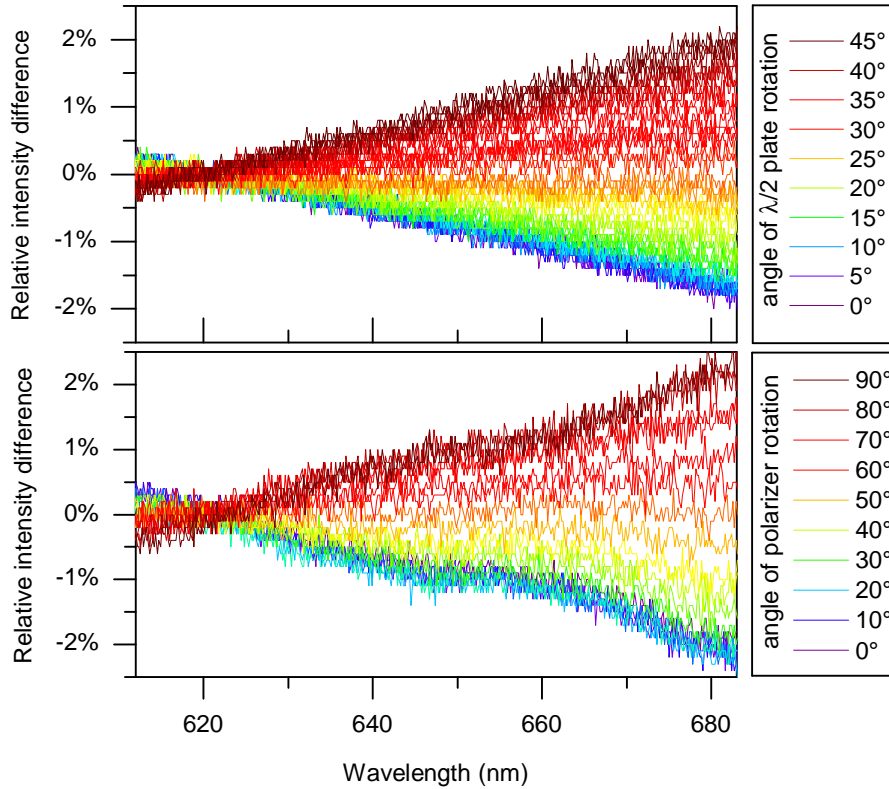


**Figure 4.15: Comparison of spectral shapes for different polarizations.** The plots show the relative deviation of the spectra obtained for the individual polarization settings from the respective average spectrum. *Top panel:* Rotation of the half-wave plate, i.e. change of the incident laser polarization. For reasons of clarity, the plot was limited to angles of rotation between  $0^\circ$  and  $45^\circ$ , which corresponds to one rotation from vertical to horizontal laser polarization. *Bottom panel:* Rotation of the sheet polarizer in the collection optics, i.e. change of the polarization entering the detection system. Again, only one rotation from vertical to horizontal polarization is shown. Note that no Savitzky-Golay smoothing filter was employed on the underlying spectra in this case, so that the relative intensity difference curves are relatively noisy.

is changed. This is in line with expectations: a rotation of the sheet polarizer changes the polarization component which enters the detection system, so that in this case the influence of the spectral polarization dependence of the components in the light collection pass become noticeable (specifically the spectrometer grating).

Nevertheless, the overall trend is the same in both cases. It can be clearly seen that the largest deviations from the average spectrum occur for vertical polarization ( $0^\circ$ ) and horizontal polarization (half-wave plate rotated by  $45^\circ$ , sheet polarizer by  $90^\circ$ ); at 683 nm, the relative difference between the two sums up to 4% or 5%, respectively.

This correlation extends to absolute measured intensities as well, as shown exemplarily for one of the cases in figure 4.16: for vertical polarization, the absolute intensity is at its maximum, but decreases by around 30% with rotating polarization, until it reaches its minimum when the laser beam is horizontally polarized.

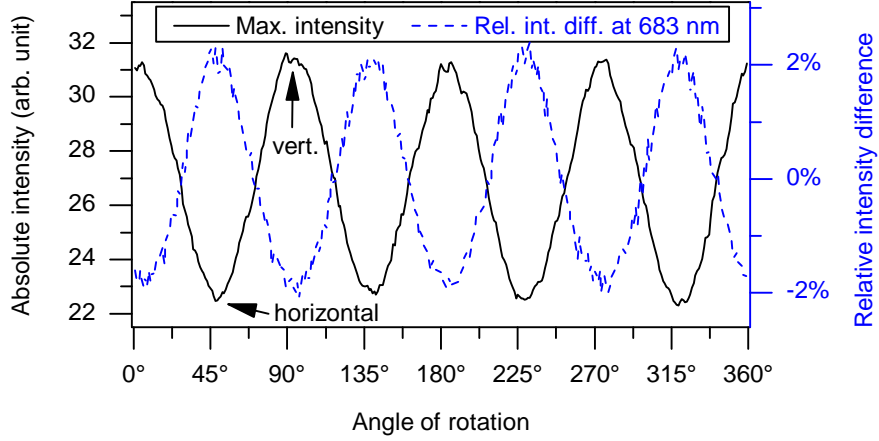


**Figure 4.16: Influence of the laser polarization on the measured spectra.** The plot shows the dependence of the measured luminescence spectra on the half-wave plate with respect to (1) the maximum intensity of the non-normalized spectra and (2) the respective relative intensity difference to the average spectrum at a selected wavelength of 683 nm. The latter serves as an approximate value for the largest deviation in spectral shape in the wavelength range of interest. The positions of vertical and horizontal laser polarization are indicated by the arrows; they recur in intervals of 90°. At these positions, the extrema of both curves coincide. The same qualitative behaviour is observed for the second measurement as well (not included in this plot).

**Discussion** The observed changes in absolute intensity indicate that the luminescence light is partially polarized. According to [Feo61], a luminescent medium excited by polarized light can emit light which is partly unpolarized and partly maintains the polarization of the excitation light source, even if the medium itself is isotropic. In the case considered here, this explains why the maximum absolute intensity is reached for the setting in which the incident laser polarization and the polarization component which passes the sheet polarizer match; as soon as one of these is changed, the polarization component which is detected in the end decreases.

Along with the absolute intensity, however, the spectral shape varies: the correlation in the polarization-dependence of both parameters is clearly visible in figure 4.16. This suggests a different spectral shape of luminescence light emitted with different polarizations. Since the SRM glass was confirmed by NIST to be homogeneous [Cho07], the effect is assumed to be due to the LARA system’s asymmetry with respect to the different polarization directions rather than due to an asymmetry in the actual light emission for vertical or horizontal incident polarization. This will be explained in more detail below:

In the following, the model of elementary electric dipoles as luminescence light emitters is used, as described in [Feo61]. The polarized light emission can then be approximated by an ideal dipole radiation pattern, with the time-averaged intensity [Dem06]

$$I(\vartheta) = \langle I(t, \vartheta) \rangle \propto \lambda^{-4} \cdot \sin^2 \vartheta, \quad (4.14)$$

where  $\vartheta$  is the angle between the emitted light and the axis of oscillation. The radiation pattern is illustrated in figure 4.17: no light is emitted in the direction of the oscillating electric field ( $\vartheta = 0^\circ$ ), while a maximum amount of energy is radiated in the plane perpendicular to it. Figure 4.18 shows the implications of the radiation pattern for the respective

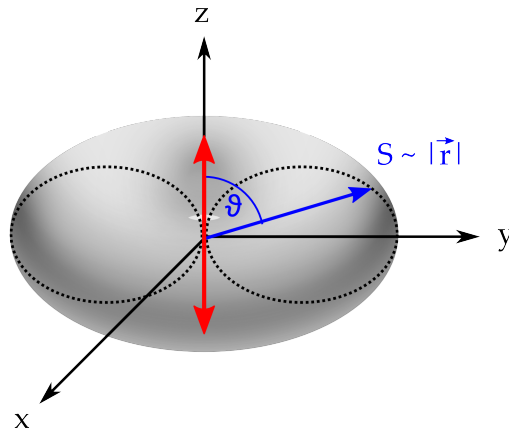


**Figure 4.17: Radiation pattern of an oscillating dipole.** The distance  $r(\vartheta)$  is proportional to the energy flux  $S(\vartheta) = I(t, \vartheta)$  radiated by the oscillating dipole (red arrow). The two ellipses show the pattern in the two-dimensional view; they represent the intersection between 3D pattern and  $y$ - $z$ -plane. The pattern is rotational symmetric. (According to [Dem06].)

Raman geometries employed by NIST and in the LARA setup. It can be seen that the incident polarization does not play a role when the NIST setup is used; the intensity of the polarized light is in each case given by the same value  $I(\vartheta = 90^\circ)$ . In contrast, in the LARA system a different part of the radiation pattern is observed depending on the incident polarization.

According to eq. (4.14), in this simple model the only difference between spectra obtained for different angles of observation  $\vartheta$  is the observed intensity. It changes by the same factor for all wavelengths, so that the spectral shape is not affected. However, the real process which leads to the emission of a broadband luminescence spectrum is more complex than that; it is quite possible that the spectral shape differs as well for different angles of observation.

This assumption is supported by the measurement results, as will be shown in the following. Based on above considerations, namely (i) the assumption of partially polarized light according to [Feo61], which was motivated at the beginning of the ‘Discussion’ paragraph, and (ii) the just mentioned assumption of different spectral shapes for different angles of observation, the spectrum observed for a certain incident polarization should consist of two components. The first component is unpolarized and has the spectrum  $I_{\text{unpol}}(\lambda)$ . The second, polarized component exhibits the spectral shape  $I(\lambda, \vartheta)$  if observed at a certain angle  $\vartheta$  to the polarization direction. Using ordinary vector algebra, each polarization direction, i.e. each orientation of the electric field vector, can be described as a linear combination of linearly independent electric field vectors. In the case considered here, the electric field vectors of vertical and horizontal polarization are linearly independent and can thus serve as a basis for the vector space of all polarization directions considered. Due to the proportionality  $I \propto E^2$  between intensity and squared electric field strength [Dem06], it is thus possible to describe the spectrum  $I(\lambda, \vartheta)$  of the polarized component for a certain angle of observation  $\vartheta$  as a superposition of the spectra obtained for  $\vartheta = 0^\circ$  and  $\vartheta = 90^\circ$ , i.e. horizontal and vertical incident polarization. For a polarization rotated by  $45^\circ$ , for instance, one should find from vector addition of the corresponding electric

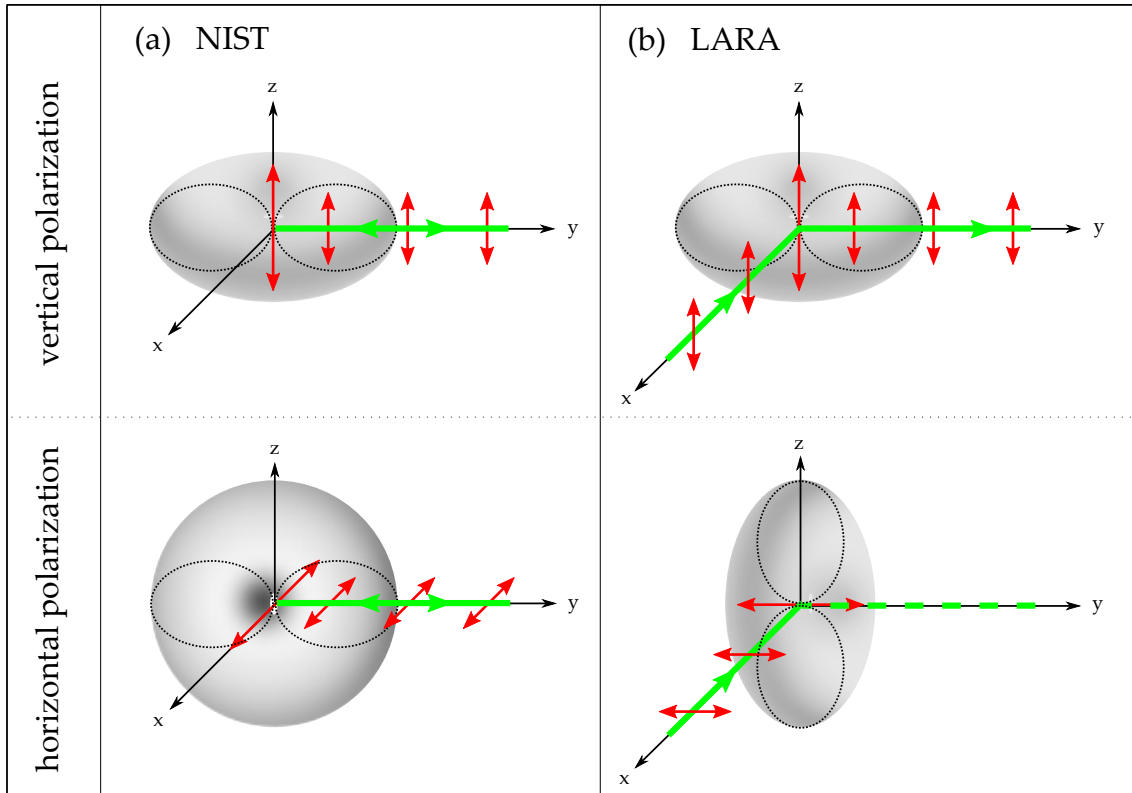


**Figure 4.18: Differences in the observed radiation for vertical and horizontal laser polarization.** To make the argumentation clearer, only those dipoles are considered which are aligned with the direction of polarization, so that the direction of the incident polarization defines the axis of oscillation. The green arrows indicate the incident and emitted polarized light, the red arrows the direction of polarization and accordingly the dipole's axis of oscillation. The polarized luminescence light is observed in the direction of the y-axis. (a) NIST setup. In the  $180^\circ$  backscattering geometry, light is observed in the direction of the laser beam, i.e. always perpendicular to the incident polarization. The observed energy flux is thus at its maximum, independent of the incident polarization. (b) LARA setup. Light is observed in a direction perpendicular to the laser beam. In case of vertical polarization, the polarization is perpendicular to the directions of both incident and observed light. Thus, a maximum amount of light is emitted in the direction of observation. In case of horizontal incident polarization, however, the dipole oscillates in the direction of observation, so that no light is emitted along this axis. In the ideal case, i.e. for an infinitely small collection angle, no polarized light is observed.

fields the following relation:

$$I_{\text{measured}}(\lambda, \vartheta = 45^\circ) = I_{\text{unpol}}(\lambda) + I(\lambda, \vartheta = 45^\circ) \quad (4.15)$$

$$= I_{\text{unpol}}(\lambda) + \frac{1}{2} \cdot (I(\lambda, \vartheta = 0^\circ) + I(\lambda, \vartheta = 90^\circ)) \quad (4.16)$$

$$= \frac{1}{2} \cdot ((I_{\text{unpol}}(\lambda) + I(\lambda, \vartheta = 0^\circ)) + (I_{\text{unpol}}(\lambda) + I(\lambda, \vartheta = 90^\circ))) \quad (4.17)$$

$$= \frac{1}{2} \cdot (I_{\text{measured}}(\lambda, \vartheta = 0^\circ) + I_{\text{measured}}(\lambda, \vartheta = 90^\circ)) . \quad (4.18)$$

This is indeed observed: when averaging the measured spectra obtained for vertical laser polarization and the ones obtained for horizontal laser polarization, the resulting mean spectrum deviates by less than 0.5% from the spectra obtained for an incident polarization rotated by 45° (i.e. for half-wave plate angles of rotation of  $\alpha=22.5^\circ$ ,  $67.5^\circ$  etc.). The same results were obtained in a measurement run with the LARA 2 system, in which the incident polarizations were varied accordingly.

**Conclusion** The considerations above have shown that the measurement results can be explained by the assumption that each measured spectrum represents a spectrum of partially polarized light, in which the unpolarized component as well as the respective polarized component exhibits its own spectral shape. From these considerations, a conclusion has to be drawn for the calibration procedure. The first question is under which polarization configuration NIST has obtained the certified spectral shape. The second question is then which polarization configuration has to be chosen to obtain the same spectral shape at the LARA setup, taking into account not only the different geometry, but also the influence of the sheet polarizer.

The spectrum observed by NIST consists of a superposition of a completely unpolarized component with spectral shape  $I_{\text{unpol}}(\lambda)$ , and a completely polarized component  $I(\lambda, \vartheta = 90^\circ)$ , which is independent of the incident direction of polarization:

$$I_{\text{NIST}}(\lambda) = I_{\text{unpol}}(\lambda) + I(\lambda, \vartheta = 90^\circ) . \quad (4.19)$$

The polarization scrambler in the collection optics changes the polarization of this spectrum, but not its shape.

In the case of the LARA system, it is more complicated. Before passing the sheet polarizer, the spectrum consists of the same completely unpolarized component as in the NIST case, while the polarized component  $I(\lambda, \vartheta)$  is dependent on the incident laser polarization via the angle  $\vartheta$ . Only parts of the complete spectrum can pass the sheet polarizer<sup>9</sup>:

- As stated above, the polarized component can be described by a superposition of vertically and horizontally polarized light. Only the vertical component can pass the polarizer.

---

<sup>9</sup>Without loss of generality, a transmission of 100% for the vertical component is assumed for the following argument. In reality, the transmission is less than unity, but equally affects the incident light components (polarized or unpolarized), so that the relative intensity of the transmitted components is not changed.

- Unpolarized light can be described by a superposition of linearly polarized components with polarization directions that are uniformly distributed in the plane perpendicular to the direction of propagation [Feo61]. Thus, the intensity of the unpolarized part will be reduced by half when passing the sheet polarizer, while the spectral shape stays the same.

Due to the bisection of the unpolarized component, the polarized component has to be reduced by half as well in order to achieve the same relative contributions to the total observed intensity as in the NIST case. This can be achieved by sending in an incident polarization rotated by  $45^\circ$  to the vertical or horizontal case:

$$I_{\text{LARA}}(\lambda) = [I_{\text{unpol}}(\lambda) + I(\lambda, \vartheta = 45^\circ)]_{\text{vertical}} \quad (4.20)$$

$$= \left[ I_{\text{unpol}}(\lambda) + \frac{1}{2} \cdot (I(\lambda, \vartheta = 0^\circ) + I(\lambda, \vartheta = 90^\circ)) \right]_{\text{vertical}} \quad (4.21)$$

$$= \frac{1}{2} \cdot (I_{\text{unpol}}(\lambda) + I(\lambda, \vartheta = 90^\circ)) \quad (4.22)$$

$$= \frac{1}{2} \cdot I_{\text{NIST}}(\lambda) . \quad (4.23)$$

In the step from (4.21) to (4.22), only those components were kept which can pass the sheet polarizer.

According to these considerations, the same spectral shape can thus be achieved in the  $90^\circ$  geometry with a sheet polarizer (LARA setup) as in  $180^\circ$  backscattering geometry with a polarization scrambler (NIST setup). This means that the certified spectrum can be applied for the determination of the spectral sensitivity despite the different setups. The condition is that an incident polarization which is rotated by  $45^\circ$  to the vertical or horizontal case is chosen for the calibration measurements.

### 4.5.3 Influence of the Raman cell window on the spectral shape

For the calibration, the Raman cell is removed and replaced by a dovetail mount onto which the luminescence standard is placed, as it was shown in figure 4.6. For this reason, the luminescence light takes the same path and is thus subject to the same influences by components in the path as the Raman scattered light. There is only one difference: the Raman light has to pass the Raman cell window first. The light properties might be affected in different ways by the window, e.g. by its aperture or by a shift of the focal point due the refractive index of the glass. Thus, the influence of such a Raman window on the measured spectral shape was investigated in order to find out if it is necessary to use a Raman window in the calibration procedure as well.

**Measurement setup** The Raman cell window employed was of the same type as the one facing the collection optics in the actual Raman cell. The window was firmly held by a mount which was attached to a XYZ travel translation stage. This is shown in figure 4.19 (a). In order to closely reproduce the position of the actual cell window, a Raman cell body was employed for the alignment of the window, as illustrated in figure 4.19 (b). After the alignment, the cell body was removed with the window staying in place, and the

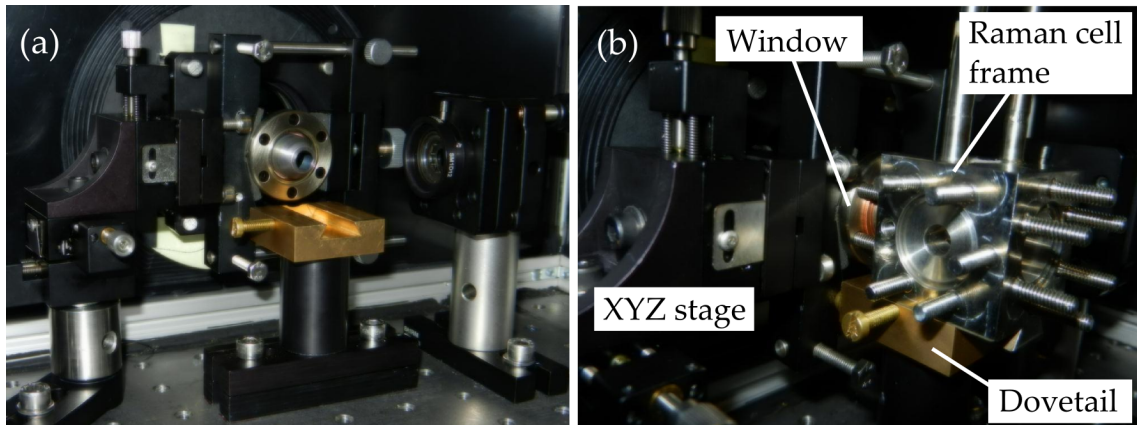


**Figure 4.19: Measurement setup.** (a) Mounting of the cell. The window was positioned in front of the dovetail mount with a XYZ stage, which allows for a translation in all three dimensions. (b) Alignment of the window. A Raman cell body was mounted to the dovetail for the alignment. Using the XYZ stage, the window could then be adjusted to the cell body in order to reproduce the position of the window in the actual Raman cell. Accordingly, a CF copper gasket was included between window and cell body to obtain the right distance of the window to the dovetail. The position of the window was adjusted until the cell body could be retracted almost without friction between the bolts and the window's mounting holes. Note that the cell body is partly retracted in the picture.

dovetail with the luminescence standard was inserted instead. A clamp was used to fix the luminescence standard to its position on the dovetail in order to allow for reproducible positioning.

**Measurements and results** In a first series of measurements, spectra were obtained with and without window in order to be able to compare both cases. For each setting, 150 spectra were taken with an acquisition time of 0.7 s each. The relative intensity difference of the respective mean spectra is plotted in figure 4.20.

It can be seen that the difference is non-negligible, amounting to up to 3% in the wavelength region of the  $\text{H}_2$   $Q_1$ -branch. For this reason, the insertion of a cell window for the calibration is necessary.

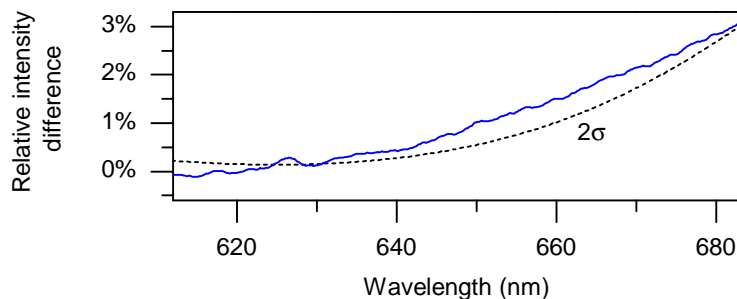


**Figure 4.20: Difference in the spectral shape for measurements with and without Raman window.** For comparison, the  $2\sigma$  confidence curve provided by NIST is plotted as well (gray, dashed line).

In a second series of measurements, the influence of the window position was investigated in order to find out how important the accurate alignment of the window is. The window was translated step-by-step in all three dimensions consecutively: parallel to the path of the laser beam (x-direction), parallel to the direction of observation (y-direction) and vertical (z-direction). In each case, the window started from the center position obtained with the alignment described above. For each revolution of the XYZ mount's fine-adjustment screw, which corresponds to a translation by approximately  $250\ \mu\text{m}$ , five spectra were taken with an acquisition time of 1 s each.

The results can be summarized as following (plots not shown here):

1. In the x-direction, an increasing difference in spectral shape is observed with increasing distance from the center position. The difference is smaller than 0.5% over the whole wavelength range of interest in a range of  $\pm 0.5\ \text{mm}$  left and right of the center.
2. In the y-direction, no relative intensity difference  $> 0.4\%$  is observed for the full measurement range, i.e. up to a distance of 4 mm from the center position.
3. In the z-direction, a window movement of  $\pm 1.5\ \text{mm}$  is possible without exceeding a maximum deviation of 0.5%.

**Conclusion** Especially the results obtained for the x-direction show that an accurate positioning of the window is important in order to obtain the correct spectral sensitivity. For this reason, the described alignment procedure using the Raman cell body was applied in all calibration measurements. In the x- and z-direction, the tolerance in position is smaller than 0.5 mm.

In a future step, the luminescence standard could be employed in an improved custom-built mount into which the window is already integrated (see outlook in chapter 6).

#### 4.5.4 Difference between double-pass and single-pass mode

As briefly mentioned in the description of the LARA system in section 3.2, a modification of the setup shown there is possible. In this setup, the laser beam is reflected by a mirror behind the Raman cell, so that it passes the cell a second time ("double-pass mode"). By this means, the Raman signal is enhanced. This mode can currently be used in the LARA systems 1 and 3 and is intended to be employed in the final Raman setup for KATRIN. For this reason, the applicability of the luminescence standard to double-pass mode instead of single-pass mode was investigated.

**Measurement setup** The principle setup is shown in figure 4.21. It can be seen that the luminescence standard was not aligned parallel to the laser beam; this was necessary due to the displacement between incident and reflected beam. A beam dump was used to switch to single-pass mode without changing the SRM alignment. In both double- and single-pass mode, 50 spectra were taken with an acquisition time of 3 s each.

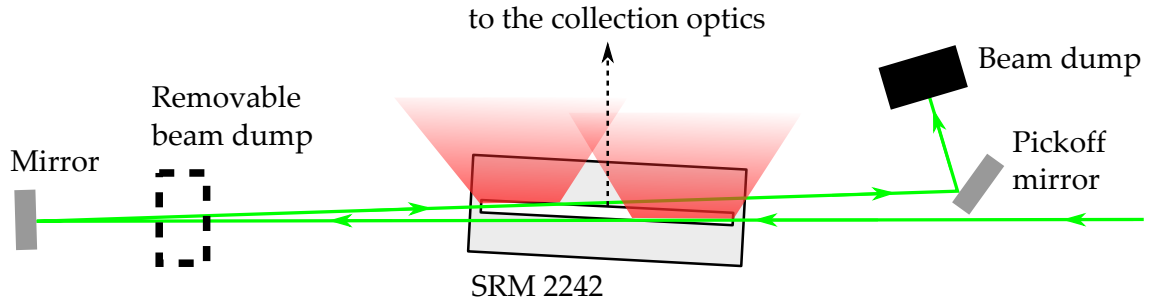


**Figure 4.21: Use of the luminescence standard in double-pass mode.** In double-pass mode, the laser beam coming from the right is reflected by a mirror in order to pass the Raman cell (here replaced by the luminescence standard) twice. The reflection angle deviates from zero to avoid a back-reflection into the laser. The mode can be changed between double-pass to single-pass by inserting a beam dump in front of the mirror. In order to allow both the incident and the reflected beam to pass through the thin SRM glass slide in double-pass mode, the luminescence standard has to be rotated by a certain angle. By this, however, the replication of the Raman scattering region becomes worse; light is emitted from the outer regions of the Raman rather than from the center or from all along the slide length.

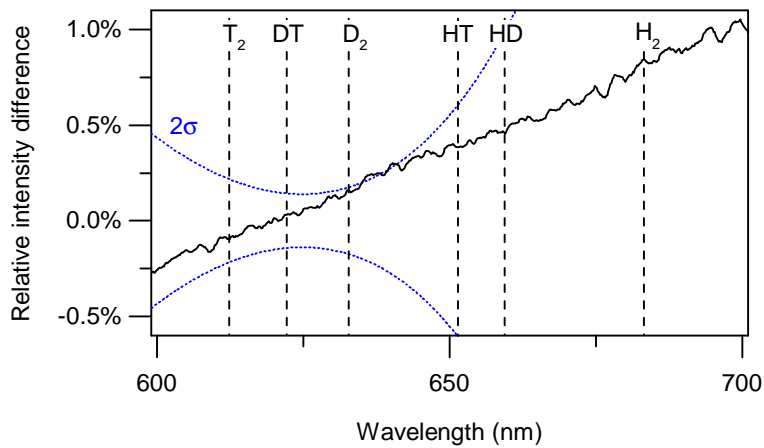


**Figure 4.22: Difference in spectral shape between double- and single-pass mode.** The vertical, dashed lines indicate the wavelength positions of the  $Q_1(J'' = 0)$  lines of the hydrogen isotopologues.

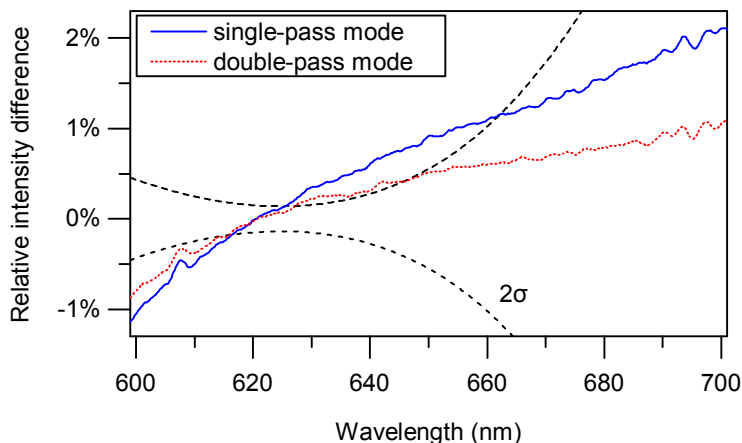


**Figure 4.23: Difference to parallel alignment.** The plot shows the relative intensity difference between a standard spectrum obtained for parallel alignment (cf. subsection 4.5.1) and the respective spectra obtained for double- and single-pass mode with non-parallel luminescence standard, as shown in figure 4.21.

**Results** The relative intensity difference of the average spectra of both measurements is shown in figure 4.22. Apart from the region between 635 nm and 641 nm, in which none of the relevant hydrogen lines are located, the difference is within the  $2\sigma$  confidence curves provided by NIST. However, a comparison with the spectrum obtained for parallel alignment yields a larger difference, as can be seen in figure 4.23.

**Discussion and conclusions** The aforementioned deviations can probably be traced back to the non-parallel alignment of the luminescence standard. This is in line with the results of the investigation concerning the position of the luminescence standard (see subsection 4.5.1). The observed deviation is even larger for single-pass mode than for double-pass mode, which is probably due to the fact that the regions of light emissions are not centered with respect to the collection optics, as shown in figure 4.21. In single-pass mode, the luminescence light comes from a position right from the center only, while contributions from both sides enter the detection system in double-pass mode; thus, differences in spectral sensitivity of light coming from different positions along the laser beam are better accounted for in the latter case.

Due to the inadequate replication of the scattering region, it is not recommended to use the luminescence standard in the way described above. Instead, it is suggested to use it in parallel alignment only, even in double-pass mode. With a very careful alignment of the backreflecting mirror and the pickoff mirror, it can be tried to achieve a smaller angle between the two beams, so that both beams might pass the luminescence standard in full length. Otherwise, the calibration can be done in single-pass mode only and the results used for the correction of the double-pass mode as well. Under the conditions described above, the difference between both modes was within the NIST confidence curve.

A strong evidence for the legitimacy of this approach is the comparison of Raman measurements of  $\text{H}_2\text{-HD-D}_2$  gas mixtures in both double- and single-pass mode, which are described in detail in the following chapter (see especially section 5.4 and 5.5). The average deviation between the individual relative Raman signal amplitudes measured in the

two modes is  $< 0.2\%$ , so that it can be confidently assumed that the difference in spectral sensitivity between both modes is negligible.

#### 4.5.5 Influence of temperature and laser power on the spectral shape

The influence of varying temperatures and laser powers was already investigated by NIST. According to the SRM 2242 Certificate of Analysis, SRM 2242 is certified for a temperature range between  $20\text{ }^{\circ}\text{C}$  and  $25\text{ }^{\circ}\text{C}$ , and it is stated that “no significant changes in the shape of the luminescence spectrum occur over the range of laser power densities commonly used in Raman instruments” [NIS08]. It can be assumed that heating of the luminescence standard due to the laser exposure was minimal in the NIST setup, since the laser path through the luminescence standard is very short in a  $180^{\circ}$  backscattering setup; however, this is not the case in the LARA setup, where the laser beam passes through the whole length of the glass slide. Thus, investigations concerning the influence of laser power and temperature were carried out, as described in the following.

**Measurement setup** Two different series of measurements were conducted:

##### 1. Heating by the laser beam

It was tested how much the SRM was heated by a laser beam with a power of 300 mW in normal calibration mode, i.e. with the beam being incident on the side surface and passing parallelly through the glass slide. Simultaneously, the effect on the luminescence spectrum was examined. For this measurement, a CrNi thermocouple was clamped to the top surface of the luminescence standard in its mount, as shown in figure 4.24. The temperature data were recorded by a multimeter with an accuracy of 1 K. Spectra were taken continuously with an acquisition time of 0.02 s while the luminescence standard was exposed to the laser beam. The measurement was terminated when the temperature did not increase any further over a period of over 10 min.

Note that the setup employed does not allow to measure the glass temperature directly at the interaction region. The measurement point was in a distance of around 4 mm to the laser beam on the glass surface, with a possible slight isolation due to thin tissue employed. Also, the thermal conductivity of the glass is not expected to be very high. For this reason, the actual temperatures in the region of light emission might be higher than the measured ones. Nevertheless, it should be noted that NIST states that the “temperature of the SRM glass” was controlled by a custom-built temperature cell in their measurements [Cho07]. This indicates that the temperature of the glass slide in total was approximately stabilized, which might have led to a more uniform temperature distribution compared to the setup used here due to a smaller temperature gradient to the surroundings; however, it does not seem as if a special focus had been put on the determination of the temperature directly in the interaction region in their case either.

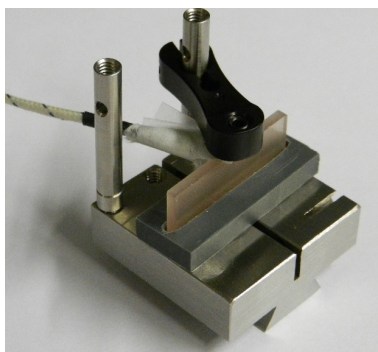


**Figure 4.24: Measurement of the luminescence standard temperature.** The CrNi thermocouple was fixed to the surface of the glass slide by a clamp. In order not to damage the standard, a thin tissue was used between the glass surface and the probe.

## 2. Laser power

In another test series, the influence of the laser power on the luminescence spectrum was investigated. The luminescence standard was exposed to laser powers of 50, 100, 150, 200, 250 and 300 mW. For each setting, 30 spectra were taken with an acquisition time of 1.5 s each. Between each two measurements, the laser beam was interrupted for 1 to 2 min, so that the luminescence standard could cool down again. The glass temperature was not recorded in this measurement.

**Results and discussion** Starting at room temperature, the measured luminescence standard temperature increased by 5 K within 6 min when exposed to a laser power of 300 mW. In the SRM 2242 Certificate of Analysis, an “overall shift of the luminescence to lower Raman shifts with increasing temperature” is reported: while the actual spectral shape is unaffected, the peak center shifts by  $-1.9 \text{ cm}^{-1}/^{\circ}\text{C}$  according to NIST. In the measurement taken here, such a shift was observed in the stated order of magnitude.

In the measurement with varying laser power, a similar shift was observed, as illustrated in figure 4.25. Taking the above value given by NIST as a basis, however, the observed shift corresponds to a temperature difference of approximately 9 K between the measurement with 50 mW and the one with 300 mW laser power. It is noticeable that this shift due to varying laser power is larger than the one purely due to heating of the glass. Nevertheless, the observed deviations from the mean spectrum lie inside the confidence curves given by NIST and are thus tolerable.

**Conclusion** The measurements show that the influence by laser power is tolerable in the range investigated here. In order to stay within the certified temperature range of  $20^{\circ}\text{C}$  to  $25^{\circ}\text{C}$ , power values  $> 300 \text{ mW}$  are not recommended due to the heating of the luminescence standard, as long as no extra cooling is employed.

According to [Cho07], NIST used a 200 mW laser for their measurements. As mentioned above, it can be assumed that the heating due to laser exposure was less in their case due to the shorter laser path through the luminescence standard in their setup. For this reason, it is suggested to employ a laser power of around 100 mW to 150 mW to reduce heating by the laser without deviating too much from the laser power employed by NIST.

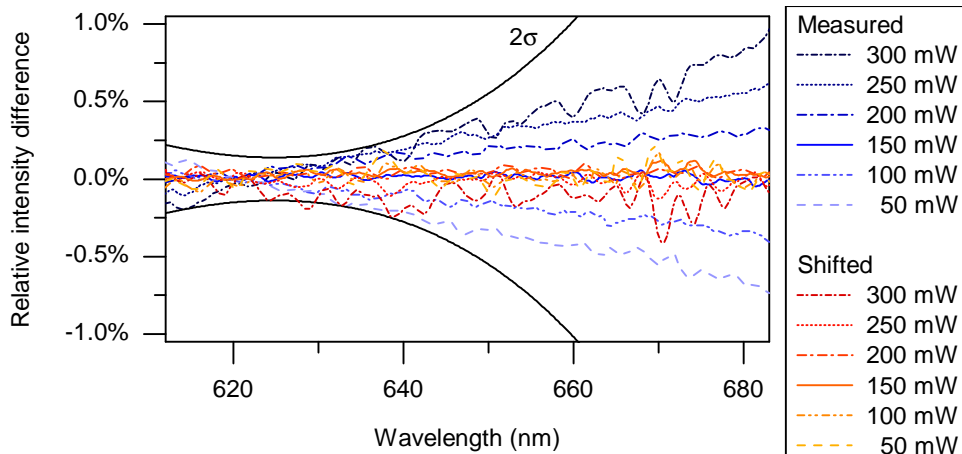


**Figure 4.25: Shift of the luminescence spectrum with laser power.** The blue curves (measured) show the relative intensity difference of the spectra measured for different laser powers to their average spectrum. The observed differences can be explained under the assumption that the actual shape of each spectrum is the same, but that the spectra are shifted to longer wavelengths with increasing power. This can be confirmed by applying a power-dependent shift to the wavelength scale of each measured spectrum, which just compensates the temperature-induced shift. This was done for the individual NIST spectra, using the relationship between temperature and shift which was provided by NIST [NIS08]. A linear increase in temperature with increasing laser power was assumed. All spectra could be approximately brought to agreement by applying a shift corresponding to a temperature difference of 9 K between the 50 mW and the 300 mW measurement. The relative intensity differences of the shifted spectra to their average spectrum are represented by the orange curves. By and large, the difference curves fluctuate around zero.

#### 4.5.6 Conclusions for the measurement procedure

The investigations show that the luminescence standard SRM 2242 can be employed for the determination of the spectral sensitivity of the LARA setup. However, several points need to be considered in the calibration procedure. The suggested measurement settings are the following:

- The luminescence standard should be positioned as shown in figure 4.10(a): parallel to the laser beam, with the laser being incident on the small surface of the glass slide and with the frosted surface facing the collection optics.
- In contrast to the actual Raman measurements, in which the incident laser beam has to be vertically polarized, the calibration measurement requires a polarization which is rotated by  $45^\circ$  to the vertical case. This is achieved by a rotation of  $22.5^\circ$  of a half-wave plate which is positioned in the region of collimated light before the laser beam is focused onto the sample. Note that this half-wave plate should be a permanent part of the LARA system and not only be inserted for the calibration measurements due to a possible, small displacement of the laser beam by the half-wave plate.
- To account for a possible inaccuracies in the adjustment of the half-wave plate, it is advisable to carry out multiple measurement runs with different rotations which

all lead to the desired  $45^\circ$  rotation of polarization ( $22.5^\circ$ ,  $67.5^\circ$ ,  $112.5^\circ$  etc.), and to average over the results.

- A Raman window has to be placed between the luminescence standard and the collection optics. It has to accurately reproduce the position of the window of the actual cell employed for the Raman measurements. The use of a Raman cell body for the positioning as described in subsection 4.5.3 is strongly recommended.
- The spectrum of the luminescence standard is certified for a temperature range of  $20^\circ\text{C}$  to  $25^\circ\text{C}$ . The ambient temperature has to be kept in this range. Apart from that, a heating of the luminescence standard by the laser beam should also be kept low. The laser power should thus not be higher than 300 mW; a lower power of around 100 mW to 150 mW is suggested.

If this measurement procedure is followed, it is expected that the luminescence standard can be employed for the determination of the spectral sensitivity within the given confidence level. Cross-checks of the validity of the obtained results are presented in the following section.

## 4.6 Validity cross-check of the spectral sensitivity determination

The investigations presented above provide valuable information about conditions necessary for a correct determination of the spectral sensitivity as well as about conditions which have to be avoided for the same purpose. However, as discussed at the beginning of the previous chapter, they do not allow to finally conclude whether the obtained spectral sensitivity is really the correct one. The NIST-certified spectrum and thus the obtained spectral sensitivity curve might not be valid if any systematic effect connected to the differences to the NIST setup was not regarded or the measurement results incorrectly interpreted. For this reason, cross-checks were carried out to test if spectra can be successfully intensity-corrected with the measured spectral sensitivity curve.

The idea behind the cross-check is simple: the spectrum of the same light source is measured with different Raman systems. These systems naturally exhibit different spectral sensitivities, which are determined using the luminescence standard. Each spectrum is then corrected with the respective spectral sensitivity curve. If the spectral sensitivity was correctly determined, all curves should agree after the correction.

**Determination of the spectral sensitivity** The luminescence spectrum of SRM 2242 was measured using all three LARA systems according to the procedure described in the previous section. The laser power was in each case 300 mW and thus higher than the suggested optimal value, but still within the acceptable range. The treatment of the raw spectra comprised the following steps: dead pixel removal, cosmic ray removal, astigmatism correction, background removal, normalization, averaging (cf. beginning of section 4.5). The thus obtained spectrum was divided by the NIST-certified curve in order to calculate the spectral sensitivity curve according to eq. (4.10).

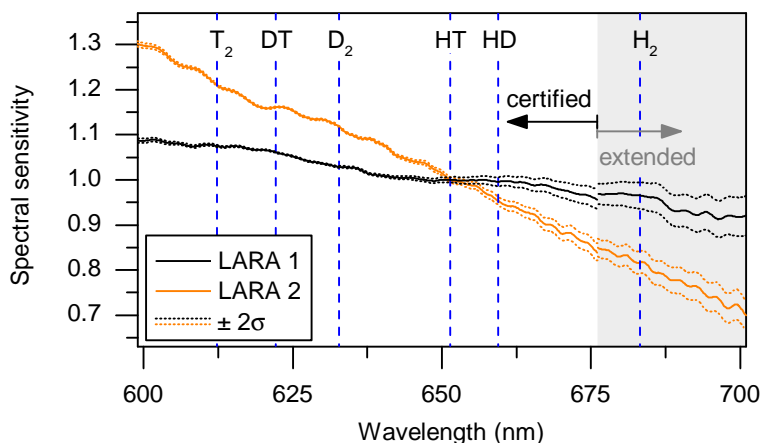


**Figure 4.26: Spectral sensitivity of two different LARA systems.** Both curves were normalized to the position of the  $Q_1(J''=0)$  line of HT (651.4 nm) for easier comparison. The corresponding line positions of all isotopologues are indicated by the blue, dashed lines. The gray area marks the wavelength range in which the NIST-certified polynomial is not valid. In this area, the extended range data provided by NIST [Cho12] were used for the calculation of the spectral sensitivity curve; the  $2\sigma$  curves were obtained by extrapolation, as described in 4.4.3.

The result is plotted for the LARA 1 and the LARA 2 system in figure 4.26; the corresponding LARA 3 curve is very similar to the obtained for LARA 1 and is not shown here for reasons of clarity. In all three cases, a decrease in sensitivity with increasing wavelength is observed in the wavelength range considered here. This decrease is by far largest in the LARA 2 system: while the spectral sensitivity at the  $Q_1(J''=0)$  position of  $H_2$  is still at 90% (86%) of the value at the position of  $T_2$  in the case of LARA 1 (LARA 3), it drops to 67% in the case of LARA 2.

**Comparison of LED spectra** The spectrum of a white light LED was measured at both the LARA 1 and the LARA 2 system. In the LARA 1 (LARA 2) system, 100 (30) spectra were taken with an acquisition time of 0.2s (0.5s) each and treated according to the description in the previous paragraph. The measurement setup is shown in figure 4.27: in order to roughly reproduce the region of light emission from Raman and SRM 2242 measurements and to achieve a comparability of both systems, a microscope slide with frosted front surface was placed into the laser beam path and illuminated with the LED light. In figure 4.28, the spectra measured at both systems are shown before and after the intensity correction. The difference between the two measured spectra prior to correction is clearly visible: they neither agree in the position of the maximum nor in the steepness of their flanks, and a wave-like modulation of the LARA 2 curve is observed towards shorter wavelengths. After the correction with the respective spectral sensitivity, however, both curves agree quite well. The relative intensity difference in the region of the hydrogen  $Q_1$ -branches lies between 0.8% ( $T_2$ ) and -1.8% ( $H_2$ ). Considering the character of the measurement as a rough cross-check, especially with respect to the imperfect reproduction of the Raman scattering region in both systems and the fact that no Raman window was employed, this is an acceptable result, which shows that the correction works in principle.

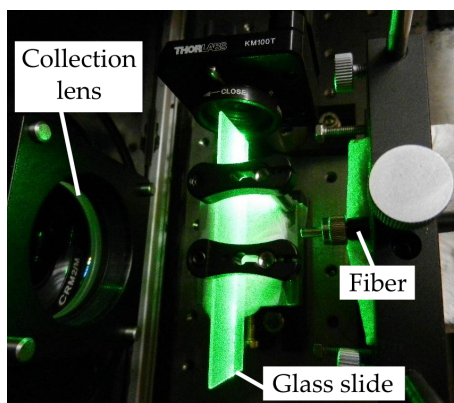


**Figure 4.27: Measurement of the spectrum of a white light LED with the LARA 1 system.** An optical fiber was used to transport the LED light to the Raman measurement region. It illuminated a glass slide, which was aligned along the laser path. Note that the laser is activated in this picture to demonstrate the alignment; for the actual LED measurements, the laser was deactivated.

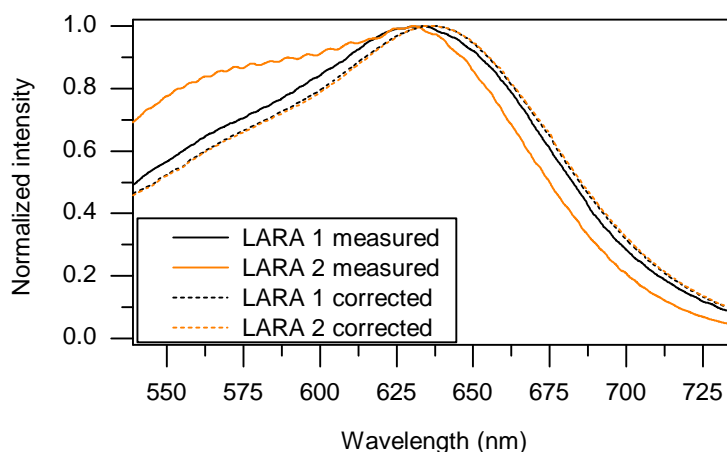


**Figure 4.28: Measured and corrected white light LED spectra.**

**Comparison of the Raman measurement of a hydrogen gas mixture** To obtain more quantitative results and to prove the eligibility of the luminescence standard for the task at hand, the Raman spectra of a gas mixture of  $H_2$ , HD and  $D_2$  taken at the LARA 1 and the LARA 3 system were compared. Both spectra are shown in figure 4.29. An additional measurement at the LARA 2 system was discarded due to considerable deviations of the measurement results, which were discovered at a later date and are in all likelihood due to a misalignment of the Raman cell caused by a loosening of the cell mount.

For each of the isotopologues  $x$ , the absolute Raman signal amplitude  $S_x$  was obtained by determining the area of the respective  $Q_1$ -branch. The relative response functions  $R_{x,rel}$  were calculated according to eq. (4.6), using the spectral sensitivity  $\eta$  as obtained from the measurement with the luminescence standard. Thus, the mole fraction  $y_x$  of each

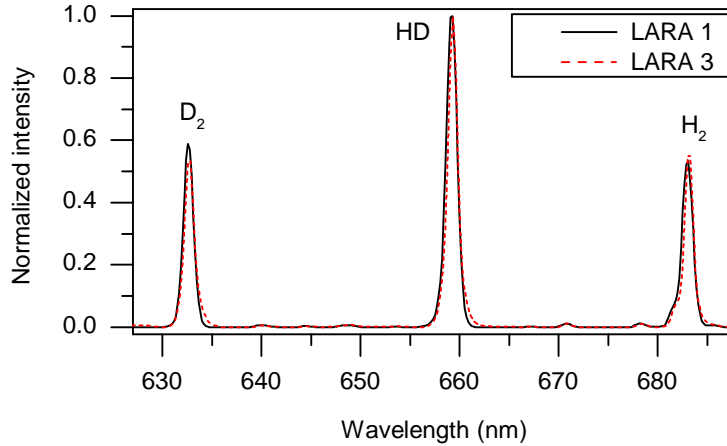


**Figure 4.29: Uncorrected spectrum of the same gas-filled cell measured at two different LARA systems.** In both cases, the laser power was 3 W. The LARA 1 spectrum is an average over 50 spectra, which were taken with an acquisition time of 7.5 s each. In the LARA 3 system, 38 spectra were taken with an acquisition time of 100 s each.

isotopologue could be determined:

$$y_x = \frac{S_x}{R_{x,\text{rel}}} / \left( \sum_i \frac{S_i}{R_{i,\text{rel}}} \right). \quad (4.24)$$

In table 4.2, the results obtained at both LARA systems are compared. It can be seen that the mole fractions differ by up to 3.2% if the measured Raman signals are not corrected for the respective response, i.e. if all  $R_{x,\text{rel}}$  are set to 1 in eq. (4.24); after the correction, however, the results agree to better than 0.7%. In the case of  $\text{D}_2$ , for which the certified relative uncertainty of the SRM 2242 is the smallest with a value of around 0.2%, the agreement is the best: here, the relative difference amounts to only 0.02%. This demonstrates the success of the correction. Thus, it can be concluded that the procedure for the spectral sensitivity determination described in subsection 4.5.6 leads to the correct results. A final confirmation of this assumption can be obtained by probing the calibration results with an independent calibration method. This will be described in chapter 5.

**Table 4.2: Comparison of the results obtained with the two LARA systems.** The table shows the results for the gas composition obtained for each LARA system if (i) the uncorrected Raman signal amplitudes are used for the calculation, and (ii) the Raman signal amplitudes are corrected with the response functions  $R_{x,\text{rel}}$ . The last two columns show the relative difference between the results obtained with LARA 1 and the ones obtained with LARA 3 for both cases.

Isotopologue $x$	Uncorrected $y_x$ (%)		Corrected $y_x$ (%)		$\Delta y_x / y_x$ (%)	
	LARA 1	LARA 3	LARA 1	LARA 3	Uncorrected	Corrected
$\text{H}_2$	26.43	25.78	25.66	25.51	2.45	0.62
HD	48.20	48.03	47.69	47.86	0.34	-0.34
$\text{D}_2$	25.38	26.19	26.64	26.64	-3.20	0.02

## 4.7 Summary and conclusions

The investigations presented in this chapter show that the use of the luminescence standard SRM 2242 is a suitable method for the determination of the spectral sensitivity of the LARA systems for KATRIN. Its greatest advantages are a very good replication of the Raman scattering region, and low uncertainties. Apart from that, it is uncomplicated to employ, relatively low in cost and has a long lifetime.

It could be shown that the challenges connected to the use of this standard can be successfully counteracted, both with respect to its limited range of certification and the use in a setup which differs from the one it was certified for. Based on a range of investigations of systematic effects influencing the measured spectrum, a measurement procedure for the spectral sensitivity was developed. By following this procedure, it should be ensured that the NIST-certified spectral curve can be employed for the spectral sensitivity determination. The results of first cross-checks to test the validity of the obtained results were promising.

Using the obtained spectral sensitivity data, the response functions of all hydrogen isotopologues could be determined according to eq. (4.4) and (4.2). The results and the corresponding systematic uncertainties are shown exemplarily for the LARA 1 system in table 4.3. It can be seen that the total uncertainty in the response function is well below 5%.

However, it was also discussed in this chapter that the use of theoretically derived input values for the calculation of the response functions requires experimental verification of the calibration results. Such a verification measurement will at the same time probe the spectral sensitivity used for the calibration and can thus confirm the applicability of the suggested measurement procedure.

The implementation of the verification approach is described and analyzed in the following chapter.

**Table 4.3: Raman response functions obtained by the calibration method based on theoretical Raman signal amplitudes.** The values were normalized so that  $R_{\text{H}_2} = 1$ .  $\Delta R_{\text{theo}}$  represents the uncertainty which is associated with the confidence placed in the theoretical values. They were obtained by depolarization measurements, as described in section 4.2.  $\Delta R_{\text{sens}}$  is the uncertainty contribution by the spectral sensitivity, which is defined by the  $2\sigma$  confidence curves provided for SRM2242. The total uncertainty  $\Delta R_{\text{tot}}$  is given by the quadratic sum of the two contributions. This table was already published in [Sch12e].

Isotopologue	$R_x$	$\Delta R_{\text{theo}}$ (%)	$\Delta R_{\text{sens}}$ (%)	$\Delta R_{\text{tot}}$ (%)
H <sub>2</sub>	1.000	2.9	3.0	4.2
HD	0.981	3.0	1.0	3.1
HT	0.960	3.1	0.6	3.2
D <sub>2</sub>	0.925	3.4	0.2	3.4
DT	0.914	3.7	0.1	3.7
T <sub>2</sub>	0.866	3.9	0.2	3.9

## Chapter 5

# Verification of the calibration via Raman measurements of gas samples

This chapter describes a second calibration method based on the production of accurate gas samples. It can be applied for the non-tritiated hydrogen isotopologues only and is used for the verification of the calibration results obtained by the calibration approach based on theoretical Raman signal amplitudes. The motivation for the choice of the approach employed is briefly summarized in 5.1, before the measurement principle is explained in section 5.2. Section 5.3 gives a description of the gas mixing loop used for the measurements. The actual measurement procedure is described in section 5.4. In the following section, the analysis procedure is explained and the obtained results are discussed. The comparison of the final calibration results with the ones of the theoretical Raman signal approach is given in section 5.6. The resulting conclusions for the KATRIN calibration are presented in section 5.7.

The method and the gas mixing device presented in this chapter were developed in the course of the PhD thesis of M. Schlösser [Sch12b]. A first version of the mixing loop used was characterized within the diploma thesis of Ph. Herwig [Her11]. In the course of the bachelor thesis of H. Seitz [Sei11], the mixing loop was upgraded to its current state and the calibration procedure was developed. Both theses were supervised in the frame of the aforementioned PhD thesis.

In this work, the existing measurement setup and procedure were employed to perform the measurements necessary for a direct verification of the calibration results discussed in chapter 4. Contents from the publications mentioned above were included if important for the understanding of this work; for a more detailed account, the reader is referenced to the individual theses.

The content of this chapter is partly subject to a publication submitted to Analytical Chemistry [Sch12g].

## 5.1 Motivation of measurements with well-known H-D-mixtures

The discussions in the previous chapter emphasize the necessity of verifying the calibration results obtained via theoretical Raman signal amplitudes. In the section about possible Raman intensity calibration methods (3.3), it was shown that such a verification can be achieved with a second calibration method based on accurately known gas samples. Since a sufficiently accurate reference method for cross-calibration is currently not available at TLK, these calibration gas mixtures have to be produced in a well-understood and controllable process (cf. section 3.3.1). In this context, the difficulties connected to the radioactivity of tritiated gas mixtures were pointed out and a restriction to the non-radioactive hydrogen isotopologues H<sub>2</sub>, HD and D<sub>2</sub> for the verification was proposed.

Even without the additional difficulties due to radioactivity, however, the preparation of accurate gas samples consisting of these three isotopologues is a non-trivial task. The straight-forward approach would be to mix defined amounts of the individual gases in pure form to obtain a gas sample with the desired composition, which can be achieved e.g. via gravimetric [Int01] or volumetric methods [Int03a, Int03b]. However, HD gas is not commercially available in high purity [Oht12]; furthermore, due to the dissociation process  $2\text{HD} \leftrightarrow \text{H}_2 + \text{D}_2$ , the purity decreases gradually when the gas is stored [Oht11]. For this reason, the method presented in the following is based on the controlled production of HD from well-known amounts of H<sub>2</sub> and D<sub>2</sub> directly within the mixing device.

## 5.2 Measurement principle

In the gas mixing loop employed, which will be described in section 5.3, HD is catalytically produced from accurately known gas mixtures of H<sub>2</sub> and D<sub>2</sub> via the isotopic exchange reaction



By using such equilibrated gas mixtures, the response functions  $R_x$  for the three isotopologues  $x = \text{H}_2, \text{D}_2, \text{HD}$  can be determined according to eq. (3.14),

$$S_{x,\text{rel}} = R_x \cdot N_x , \quad (5.2)$$

with the method presented in the following.

The mixing loop provides the possibility to produce a gas mixture of H<sub>2</sub> and D<sub>2</sub> in a certain, accurately known ratio by using a volumetric method (see section 5.3). For this reason, the mole fractions

$$y_x^i = \frac{N_x^i}{\sum_j N_j^i} \quad (5.3)$$

of the hydrogen isotopologues  $x = \text{H}_2, \text{D}_2, \text{HD}$ <sup>1</sup> with initial absolute quantities  $N_x^i$  are known. This gas mixture is then equilibrated.

---

<sup>1</sup>There is a certain initial quantity of HD due to small impurities in the D<sub>2</sub> gas (0.3% HD). This is accounted for in the analysis (cf. section 5.5)

The final quantities  $N_x^{\text{eq}}$  can be calculated from the reaction equations [Sou86], where  $\xi$  is the extent of reaction:

$$N_{\text{H}_2}^{\text{eq}} = N_{\text{H}_2}^{\text{i}} - \xi \quad (5.4)$$

$$N_{\text{D}_2}^{\text{eq}} = N_{\text{D}_2}^{\text{i}} - \xi \quad (5.5)$$

$$N_{\text{HD}}^{\text{eq}} = N_{\text{HD}}^{\text{i}} + 2\xi \quad (5.6)$$

The law of mass action describes the concentrations of educts and products at equilibrium; they are connected by the reaction constant  $K$ :

$$K = \frac{[\text{HD}]^2}{[\text{H}_2] \cdot [\text{D}_2]} . \quad (5.7)$$

By inserting eq. (5.4) to (5.6), this equation becomes

$$K = \frac{(N_{\text{HD}}^{\text{eq}})^2}{N_{\text{H}_2}^{\text{eq}} \cdot N_{\text{D}_2}^{\text{eq}}} \quad (5.8)$$

$$= \frac{(N_{\text{HD}}^{\text{i}} + 2\xi)^2}{(N_{\text{H}_2}^{\text{i}} - \xi)(N_{\text{D}_2}^{\text{i}} - \xi)} , \quad (5.9)$$

which can be solved for  $\xi$  (for  $K \neq 4$ ):

$$\xi_{\pm}(K) = \frac{b \pm \sqrt{b^2 - 4(K - 4)(K \cdot N_{\text{H}_2}^{\text{i}} \cdot N_{\text{D}_2}^{\text{i}} - (N_{\text{HD}}^{\text{i}})^2)}}{2(K - 4)} \quad (5.10)$$

with

$$b = K(N_{\text{H}_2}^{\text{i}} + N_{\text{D}_2}^{\text{i}}) + 4N_{\text{HD}}^{\text{i}} . \quad (5.11)$$

Here, only  $\xi_-$  is a physical solution. It can be inserted into eq. (5.4) to (5.6) in order to obtain an expression for the quantities of the hydrogen isotopologues in thermodynamical equilibrium,  $N_x^{\text{eq}}$ , which is dependent only on the initial quantities  $N_x^{\text{i}}$  and the reaction constant  $K$ .

Thus, in order to accurately obtain the gas composition after the equilibration, an accurate knowledge of the reaction constant  $K$  is important. This reaction constant, which describes the gas composition in thermal equilibrium (see eq. (5.7)), is of course temperature-dependent; its values  $K(T)$  can be calculated from statistical mechanics [McQ00, Atk06]. This means that the knowledge of the reaction temperature in the equilibration process is required. An experimental determination of this parameter, however, is limited in truthness, due to the limitations of the thermocouple itself as well as due to the difficulty to measure the mean reaction temperature inside a catalyst pebble-bed with potentially inhomogeneous temperature profile. The uncertainty of the measured temperature propagates into  $K(T)$  and thus also into the calculated gas quantities. For this reason, a method is needed which allows to calculate the gas composition even without reliably knowing the true measurement temperature.

Such a method was developed by M. Schlösser in the course of his PhD thesis [Sch12b]. It makes use of two points:

1. The reaction temperature can be precisely ( $\pm 2$  K) reproduced in different measurements.<sup>2</sup>
2. The reaction constant  $K(T)$  is only dependent on the reaction temperature, but not on the number of H and D atoms present in the gas mixture as molecules.

This means that measurements can be taken with varying gas compositions, but at the same - though not well known - reaction temperature  $T_0$ . In this case, the same reaction constant value  $K(T_0)$  applies for all the individual combinations of quantities  $N_x^{\text{eq}}$  in the different measurements.

After equilibration, the relative Raman signal amplitudes as defined in eq. (3.14) can thus be expressed in terms of the initial quantities  $N_x^i$ , the reaction constant  $K(T_0)$  and the response functions  $R_x$  by using the expressions for  $N_x^{\text{eq}}$  from eq. (5.4) to (5.6) (exemplarily shown for  $\text{H}_2$ ):

$$S_{\text{H}_2,\text{rel}} = \frac{R'_{\text{H}_2} N_{\text{H}_2}^{\text{eq}}}{R'_{\text{H}_2} N_{\text{H}_2}^{\text{eq}} + R'_{\text{D}_2} N_{\text{D}_2}^{\text{eq}} + R'_{\text{HD}} N_{\text{HD}}^{\text{eq}}} \quad (5.12)$$

$$= \frac{R'_{\text{H}_2} (N_{\text{H}_2}^i - \xi_-)}{R'_{\text{H}_2} (N_{\text{H}_2}^i - \xi_-) + R'_{\text{D}_2} (N_{\text{D}_2}^i - \xi_-) + R'_{\text{HD}} (N_{\text{HD}}^i + 2\xi_-)}, \quad (5.13)$$

where the extent of reaction  $\xi_-$  is a function of  $K(T_0)$ ,  $N_{\text{H}_2}^i$ ,  $N_{\text{D}_2}^i$  and  $N_{\text{HD}}^i$  according to eq. (5.10), and where  $R'_x = R_x \cdot \sum S_i$  represents a modification<sup>3</sup> of the response function  $R_x$  as introduced in section 3.1.4.

The relative Raman signal amplitudes  $S_{x,\text{rel}}^{\text{eq}}$  are obtained from the Raman measurement of the individual gas mixtures, the respective  $N_x^i$  are proportional to the known mole fractions  $y_x^i$ , and  $K(T_0)$  is an unknown, but constant value for all measurements. Both  $K(T_0)$  and the actual parameters of interest, the modified response functions  $R'_x$ , can thus be obtained by a simultaneous fit of the measured Raman signal amplitudes to the respective initial mole fractions for the different gas compositions.

### 5.3 Setup of the Hydrogen Deuterium Equilibration loop

The gas mixing device used for the production and equilibration of accurately known  $\text{H}_2$ - $\text{D}_2$ -mixtures is called Hydrogen Deuterium Equilibration loop (HYDE). A sketch of its setup is shown in figure 5.1. In the following, important components and their respective task are shortly described. Further details about the individual components are given in [Her11, Sei11].

<sup>2</sup>Note that the limitations in measurement trueness in general do not impose any restrictions on the precision of a measurement, i.e. its reproducibility.

<sup>3</sup>The modified response functions  $R'_x$  are more convenient for the discussion of the HYDE measurements than the response functions  $R_x$  as introduced in section 3.1.4. The two functions differ only by a constant factor, which cancels out when relative response functions are calculated.

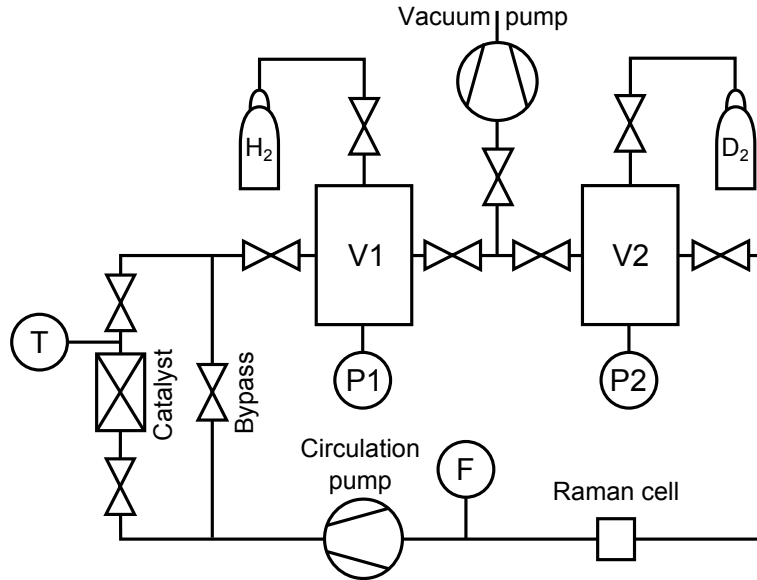


Figure 5.1: Setup of the HYDE loop (schematic). (From [Sch12b].)

**Vacuum pump** A turbo pumping station from Pfeiffer Vacuum (HiCube 80) is used to evacuate the loop.

**Vessels V1, V2 and pressure gauges** The evacuated<sup>4</sup> vessels V1 and V2 can be filled with H<sub>2</sub> and D<sub>2</sub> from the respective gas bottles. Both vessels have the same volume<sup>5</sup>, so that according to the ideal gas law, a certain ratio of H<sub>2</sub> to D<sub>2</sub> molecules can be achieved by adjusting the respective gas pressures to the same ratio. The pressures in the gas vessels are measured with the pressure gauges P1 and P2. They are from MKS (type 626AX13MBD) and measure in a range of 0 to 1000 mbar with an accuracy of 0.3 mbar.

**Circulation pump and flow controller** A metal bellows pump (Metal Bellows MB601) is used to send the gas around the loop; a uniform gas flow is provided by the a flow controller (F) from MKS.

**Catalyst** The gas can be sent through a heated catalyst in order to equilibrate the gas mixture. The catalyst from Alfa Aesar consists of pebbles made of 0.5% Pt on 1/16" Al<sub>2</sub>O<sub>3</sub>. They are located in a stainless steel tube with an inner diameter of 10 mm and a total length of about 180 mm, which is filled up to 130 mm.

The thermal equilibrium state and thus the amount of HD produced is defined by the catalyst temperature. It is regulated by a GEFTRAN 401 temperature controller, which is connected to a heating tape surrounding the catalyst tube. The approximate reaction temperature is measured with a NiCr-Ni thermocouple which is integrated into into the catalyst tube.

<sup>4</sup> $p \ll 10^{-2}$  mbar

<sup>5</sup>Using a method described in [Köll11], the volumes were determined to be  $V1=(1665 \pm 9)$  cm<sup>3</sup> and  $V2=(1655 \pm 8)$  cm<sup>3</sup>.

**Bypass** The circulating gas can be bypassed around the catalyst in order to mix gases without equilibrating them.

The Raman cell, which is connected to the whole LARA system, is integrated in the loop. The circulation of the gas mixture through the cell allows a continuous monitoring of the equilibration progress.

## 5.4 Measurement procedure

**Preparatory steps** Prior to the first measurements with the loop, a leak test was performed. The integral leak rate was found to be  $< 10^{-9}$  mbar  $\ell/s$ . Additionally, residual moisture in the system was removed by heating dry neon gas to 300 °C in the catalyst and sending it through a cold trap at LN<sub>2</sub> temperature. This step is necessary in order to avoid an isotope exchange between water molecules and the calibration gas sample via the reaction  $\text{H}_2\text{O} + \text{D}_2 \rightleftharpoons \text{HD} + \text{HDO}$ , which would influence the gas composition.

**Performed measurements** In total, 13 measurement runs were taken with different initial ratios of H<sub>2</sub> and D<sub>2</sub>. Table 5.1 gives an overview of the performed measurements. Two mixtures (H<sub>2</sub>:D<sub>2</sub> = 80:20, 20:80) were performed twice to test the reproducibility of the method.

**Table 5.1: Overview of the measurements performed with the HYDE loop.** The table shows the ratio of the initial amounts of H<sub>2</sub> and D<sub>2</sub> intended for each measurement as well as the pressure values which were actually achieved in the vessels V1 and V2.

Run	H <sub>2</sub> :D <sub>2</sub> ratio	H <sub>2</sub> pressure (mbar)	D <sub>2</sub> pressure (mbar)
1	5:95	40.0	760.0
2	10:90	80.0	719.9
3	20:80 (#1)	159.9	640.1
4	20:80 (#2)	160.0	639.5
5	30:70	240.4	559.9
6	40:60	320.0	479.8
7	50:50	399.8	400.5
8	60:40	480.0	320.1
9	70:30	560.0	240.2
10	80:20 (#1)	639.9	160.0
11	80:20 (#2)	640.1	160.1
12	90:10	719.4	80.2
13	95:5	760.0	40.0

**Measurement procedure** Each measurement was performed in the same way, following a slightly modified<sup>6</sup> version of the measurement procedure developed by H. Seitz [Sei11]. The full procedure including every individual step is given in appendix D.1. In the following, the basic steps are described.

1. **Preparation of the system:** Before the start of each measurement, the loop was evacuated for at least 12 h. During evacuation, the catalyst was baked out at 300 °C for at least 3 h. Both steps were performed in order to reduce changes of the gas composition due to outgassing from the walls or the catalyst during the actual measurement.
2. **Pre-run:** In a pre-run, a gas mixture with the H<sub>2</sub>:D<sub>2</sub> ratio intended for this measurement was produced and circulated through the HYDE loop for 30 min at a catalyst set temperature of 300 °C. Afterwards, the catalyst was cooled down to 25 °C and the whole system was evacuated again for at least 1 h. The purpose of this pre-run was to enforce an isotope exchange in the catalyst and its reactor walls. The influence of memory effects in the catalyst can be reduced by loading the catalyst surfaces with gas of the intended composition.
3. **Main run:** The actual verification measurements were taken during the main run. First of all, the vessels V1 and V2 were filled with H<sub>2</sub> and D<sub>2</sub>, respectively, in the desired ratio. The gas was then alternately circulated through the loop and blocked in order to achieve a good mixing. Afterwards, the actual measurements were performed in five steps in which the catalyst temperature was increased each time. The temperature setpoints were 25 °C, 50 °C, 75 °C, 100 °C and 125 °C. For each of these, the gas was circulated through the loop for 30 min in double-pass mode, i.e. the laser beam passed through the Raman cell two times, and for 10 min in single-pass mode.

Raman measurements were taken not only in the phases with stable gas composition, which are of interest for the analysis, but during the whole pre- and main run to allow a continuous monitoring of the gas mixing and equilibration processes. The standard laser mode was double-pass mode. The Raman system settings used are listed in table 5.2.

The gases used were from Air Liquide ([www.airliquide.com](http://www.airliquide.com)), according to which the H<sub>2</sub> gas had a purity of 99.9999% and the D<sub>2</sub> gas a purity of 99.7%. A Raman measurement of the D<sub>2</sub> gas confirmed this purity and showed that the impurity consisted of HD. As briefly mentioned above, this initial HD concentration was included in the analysis.

---

<sup>6</sup>The main modifications were: (1) Only the catalyst was used for equilibration, but not a permeator which had previously been employed as well. In his bachelor thesis, H. Seitz showed that the use of a permeator changes the hydrogen gas composition, so that it is not recommended for the production of accurate hydrogen mixtures [Sei11]. (2) The Raman measurements of the equilibrated mixture were performed in two steps for each temperature, with the laser beam passing through the cell two times (double-pass mode) in the first step and then only once (single-pass mode).

**Table 5.2: Settings of the Raman system during HYDE measurements**

Parameter	Value
Laser power	5 W
CCD temperature	-73 °C
CCD gain	3
CCD readout speed	100 kHz
Acquisition time	10 s per spectrum

## 5.5 Analysis and discussion

### 5.5.1 Analysis procedure

**Treatment of the spectra** Of all the Raman spectra taken during each HYDE measurement run, only those from the main run in which the gas mixture is stable are needed for the analysis, i.e. the mixture of pure H<sub>2</sub> and D<sub>2</sub> before the equilibration (in the following referred to as ‘binary mixture’) and the equilibrated H<sub>2</sub>-D<sub>2</sub>-HD gas (ternary mixture).

For this reason, 50 spectra from the end of the gas mixing phase were used for the analysis of the binary mixture for each measurement run. Concerning the ternary mixture, thermodynamic equilibrium is reached only gradually after the setting of a new temperature. Thus, from the 30 min of double-pass measurements, the first 10 min were not used for the analysis. Additionally, 1 min between double-pass and single-pass mode measurements was not considered since the laser had to be turned off for several seconds in order to switch between the modes. Thus, sets of 98 and 46 spectra for double- and single-pass mode, respectively, were used for each temperature setting.

Using the Spectral Analysis software described in [Jam12a], the acquired spectra were treated in several steps: dead pixels and cosmic rays were removed, the spectra were corrected for astigmatism, and the background was removed by a technique called “Savitzky-Golay Coupled Rolling Circle Filter” (SCARF) followed by a median baseline correction. After this treatment, the spectra of each individual set were averaged, so that eleven mean spectra were obtained for each measurement run: one for the binary gas mixture and two spectra (double-/single-pass) for each of the five temperature settings for the ternary mixture.

From these spectra, the absolute Raman signal amplitudes  $S_x$  of the individual isotopologues  $x = \text{H}_2$ , HD and D<sub>2</sub> were obtained by determining the peak area of each  $Q_1$ -branch (cf. section 3.1.4). In this context, it has to be considered that in some cases  $S_1$ - and  $O_1$ -branch lines of one isotopologue overlap with the  $Q_1$ -branch of another. This was accounted for in the area determination; the procedure is described in appendix D.2. An alternative approach to determine Raman signal amplitudes without the need of such a correction is based on a fit of the spectra of the pure gases; it is described in appendix D.3.

**Fitting of the data** The basic principle of the data analysis was explained in section 5.2: for each temperature  $T_0$ , the three response functions  $R'_x$  and the equilibrium constant  $K(T_0)$  can be obtained by a simultaneous fit of the three individual curves for  $S_{\text{H}_2,\text{rel}}$ ,  $S_{\text{HD},\text{rel}}$  and  $S_{\text{D}_2,\text{rel}}$  (according to eq. (5.13)) to the measured data sets. Input variables are the initial mole fractions  $y_x^i$  and the respective measured relative Raman signal amplitudes  $S_{x,\text{rel}}$ .

The initial mole fractions  $y_x^i$  of each measurement run were calculated from the measured inlet pressures of the  $\text{H}_2$  and  $\text{D}_2$  gas in the vessels V1 and V2 (cf. table 5.1), the respective vessel volumes and the gas purities. The fits were performed with a least-square regression using the MINUIT routine of ROOT [Bru97]. The uncertainties of the individual measurement points, which were calculated via error propagation from the respective uncertainties in Raman intensity, pressure and volume, were considered in the fit.

Apart from the fits for the equilibrated gas mixture at different temperatures, another fit was carried out for the  $\text{H}_2$ - $\text{D}_2$ -mixture before equilibration ('binary fit'). Since no catalytic operation is involved in the binary mixture, the gas composition is expected to be less affected by systematic effects than in the case of equilibrated mixtures, so that the fit results are considered as the more reliable ones of both fits.

**Uncertainties** Due to the strong correlation of the fitting parameters, the standard deviation of the least-square fit is in the range of around 40% to 70%. An example for a correlation matrix obtained in such a fit is given in appendix D.4. A more reliable estimation of the statistical uncertainty can be obtained by using resampling methods like the so-called bootstrap method, which is suitable for the statistical analysis of samples even with a small sample size (13 runs in the case considered here) [Efr94, Ade08]. For more information about this method, the reader is referred to [Efr83, Efr94]. All the statistical uncertainty values given in the following section were obtained with this method.

Systematic influences of the analysis method were investigated by comparing the results of three different fit scenarios, in which different parameters were fixed to certain values:

**Scenario 'All free':** None of the values of the fit parameters  $R'_{\text{H}_2}$ ,  $R'_{\text{HD}}$ ,  $R'_{\text{D}_2}$  and  $K(T_0)$  is fixed.

**Scenario 'Binary fixed':** The modified response functions  $R'_{\text{H}_2}$  and  $R'_{\text{D}_2}$  are fixed to the respective values obtained by the binary fit. As explained above, these values are expected to exhibit lower systematic uncertainties than the ones obtained from the equilibrated mixtures.

**Scenario 'K fixed'** The reaction constant  $K(T)$  is fixed to the value  $K_{\text{theo}}(T_{\text{meas}})$  which is calculated from theory for the temperature measured inside the catalyst tube. These temperatures measured for each setpoint as well as the corresponding  $K(T)$  values are shown in table 5.3.

**Table 5.3: Measured catalyst temperatures and corresponding reaction constants.** The measured temperatures are averaged over the different measurement runs. It can be seen that the difference between setpoint and measured value increases with increasing temperature.

$T_{\text{set}}$ (°C)	$T_{\text{meas}}$ (°C)	$K(T)$
25	25.1	3.26
50	52.7	3.34
75	82.4	3.40
100	112.9	3.46
125	143.9	3.52

## 5.5.2 Results and discussion

A comparison of the relative Raman signal amplitudes obtained in double- and single-pass mode shows the difference to be negligible<sup>7</sup>. For this reason, in the following only the results for double-pass mode are considered, which provide better statistics due to the longer measurement time.

Figure 5.2 shows the data points as well as the fit curves for the gas mixtures before and after equilibration. The results of the parameters  $R_{x,\text{rel}}$  and  $K(T)$ , which were obtained for the three fit scenarios and at the different measured catalyst temperatures, are shown in figure 5.3 ( $R_{x,\text{rel}}$ ) and in figure 5.4 ( $K(T)$ ). Several observations can be made:

**Temperature-dependence of the uncertainties** It can be seen that the error bars become increasingly larger with higher catalyst temperatures; the uncertainty values at the lowest and the highest temperature setpoint differ by a factor of more than two. The reason might be found in temperature-related effects which influence the gas composition. In this case, the gas composition after equilibration differs from what would be theoretically expected for the respective initial amounts of H<sub>2</sub> and D<sub>2</sub> (which are not exposed to high temperatures before equilibration), leading to shifts in the measured relative Raman signal amplitudes. If the relative change in gas composition was the same for all measurement runs, biased results for the response functions would emerge from this fit. Realistically, however, the relative change fluctuates from measurement to measurement. Since the data are randomly resampled in the bootstrapping method, these fluctuations can lead to varying shifts of the fit results in one or the other direction for different resampled sets. This leads to a broader statistical distribution of the fit results and thus to an increase in the bootstrap uncertainty.

Possible effects leading to such a behaviour are:

- An increased exchange rate of atoms or molecules with the stainless steel walls or the catalyst material at higher temperatures [Miz94, Chr76]. This leads to a dependence of the change in gas composition on the gas mixture used in the previous measurement run.

<sup>7</sup>On average, the observed deviation is 0.16%. However, this value is heavily influenced by relative differences in the measured peak areas of very small peaks (like the H<sub>2</sub> peak in the H<sub>2</sub>:D<sub>2</sub>=5:95 run), where the influence of random fluctuations is comparatively high. Not considering the measurement runs with ratios of 95:5 and 5:95 yields an average deviation of 0.09%.

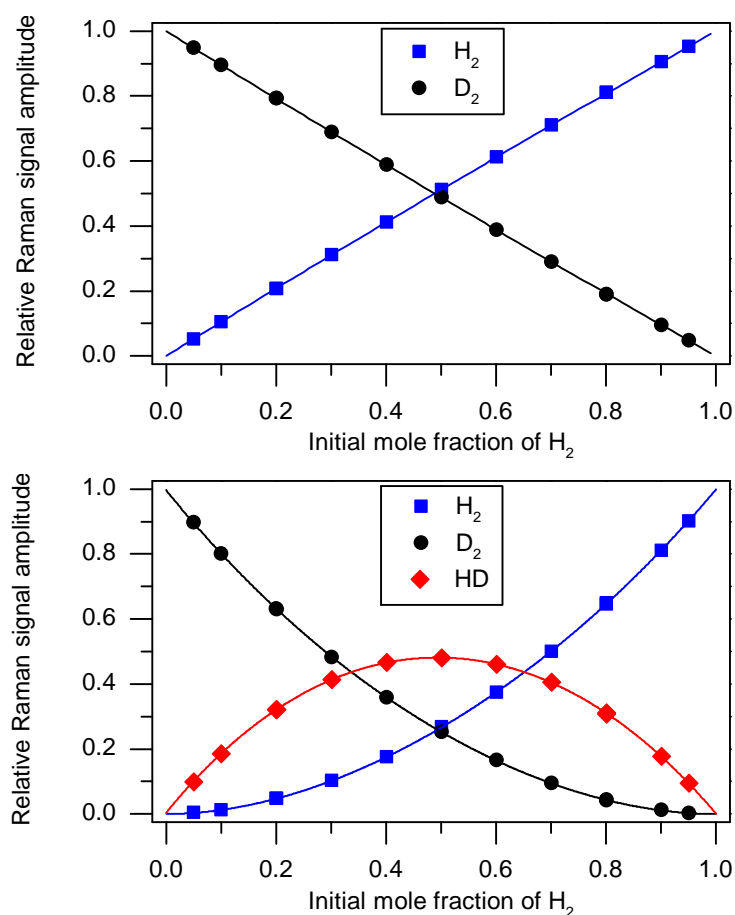


**Figure 5.2: HYDE data and fit curves.** The measured relative Raman signal amplitudes  $S_{x,\text{rel}}$  of the individual isotopologues  $x$  are plotted against the mole fraction  $y_{H_2}^i$  of H<sub>2</sub> before the equilibration of the mixture. The symbols represent the measurement points, the lines are the respective fit curves. Since the calculated uncertainties of the individual measurement points are  $< 0.002$ , the error bars are smaller than the size of the symbols. *Top panel:* H<sub>2</sub>-D<sub>2</sub>-mixture before the equilibration. *Bottom panel:* Equilibrated gas mixture at a catalyst set temperature of 25 °C. The fit curves were obtained using the ‘binary fixed’ fit scenario. Figure already published in [Sch12e].

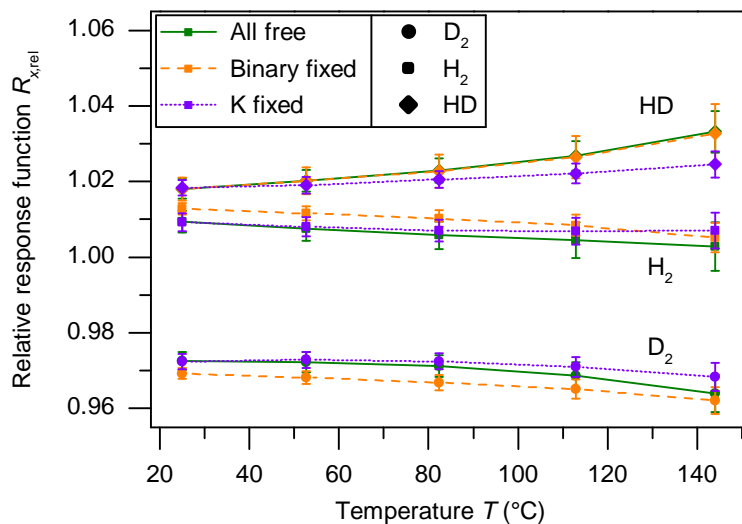


**Figure 5.3: Fit results of the relative response functions.** The plot shows the values of  $R_{x,rel}$  obtained with all three fit scenarios (*color, line style*) for the three types of isotopologues (*symbol*) at each measured catalyst temperature. The error bars represent the statistical uncertainties as obtained by the bootstrapping method. Figure already published in [Sch12e].

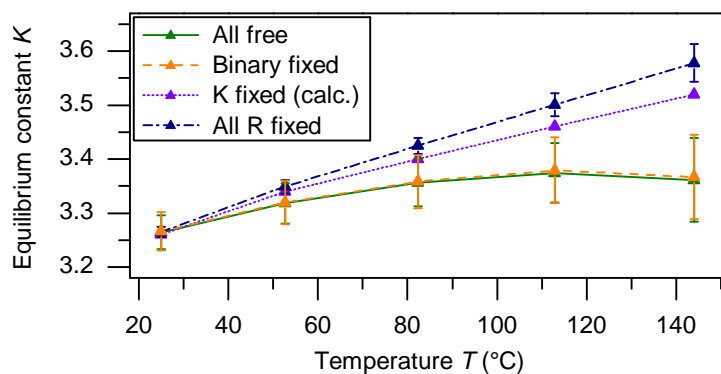


**Figure 5.4: Comparison of fit results and calculated values of the equilibrium constant  $K(T)$ .** The plot shows the values of  $K(T)$  as obtained by the different fit scenarios. The additional fit scenario ‘all R fixed’ is explained in the main text. Note that the  $K$  values of the ‘ $K$  fixed’ scenario are not fitted, but calculated from statistical mechanics, so that no error bars are given in this case. Figure already published in [Sch12e].

- Differences in the permeation of gas constituents through the stainless steel walls [Kat81]. The permeation constant differs for the different isotopes due to the isotope effect, which is relatively strong for hydrogen compared to other elements. Since permeation increases with temperature, the effect is larger for high temperatures [Kat81].

For this reason, the values obtained at a set temperature of 25 °C are considered as the most reliable ones in the following discussion.

**Differences between the  $R_{x,\text{rel}}$  results for different fit scenarios** Figure 5.3 shows that the fit results obtained with free parameters  $R'_x$  (scenarios ‘all free’, ‘ $K$  fixed’) are almost identical at temperatures  $< 85$  °C, while the values from the ‘binary fixed’ scenario exhibit a certain offset in the case of  $\text{H}_2$  and  $\text{D}_2$ . Since the latter values are derived from the binary fit, i.e. from the gas mixture before equilibration, the offset suggests an influence on the H:D ratio connected to the use of the catalyst. Again, this could be due to exchange reactions with the walls or the catalyst material. However, the observed offset is  $< 0.5\%$  and thus of the order of the statistical uncertainty.

**Temperature-dependence of the fit parameters** In figure 5.3, a certain temperature-dependence of the fit results is observed. In the ‘all free’ and ‘binary fixed’ scenario, the values at the lowest and the ones at the highest temperature setpoint differ by around 0.6 to 0.9% in case of  $\text{H}_2$  and  $\text{D}_2$  and by up to 1.5% in case of HD. This, of course, does not reflect a physical fact; the real response functions should not be dependent on temperature. The overall trend, a seeming increase of  $R_{\text{HD,rel}}$  and decrease of  $R_{\text{H}_2,\text{rel}}$  and  $R_{\text{D}_2,\text{rel}}$  with temperature, indicates that  $K(T)$  is slightly underestimated in the fit. The fit results of  $K(T)$  shown in figure 5.4 confirm this assumption: the fitted values obtained by the fits scenarios with free  $K(T)$ , ‘all free’ and ‘binary fixed’, do not increase as much as the calculated values at higher temperatures. Nevertheless, a similar trend of the relative response functions is observed, though in a weaker form, when the reaction constant  $K(T)$  is fixed in the fit; this suggests that also the measured temperature values and thus the calculated  $K(T)$  are smaller than the real reaction parameters. This is confirmed by an additional fit, in which all three  $R'_x$  parameters were fixed to the values obtained by the ‘all free’ fit at 25 °C. It is also shown in figure 5.4 (scenario ‘all R fixed’): obviously, the trend is the same as the one of the calculated values, but the values are 1 to 2% higher for temperatures  $\geq 50$  °C. However, it is noteworthy that all  $K(T)$  values agree to better than 0.3% at a setpoint temperature of 25 °C:

$$K(25\text{ °C}) = 3.264 \pm 0.004 . \quad (5.14)$$

Based on these considerations, the fit conditions can be identified which are assumed to provide the highest trueness. A brief summary:

1. The ‘binary fit’ scenario makes use of two  $R'_x$  values from the unequilibrated gas mixture, which is not influenced by systematic effects due to the equilibration process. Thus, it is assumed to exhibit the highest trueness of the different scenarios.

2. Several considerations indicate that the values obtained for equilibration at approx. room temperature (25 °C) lead to a higher trueness than those obtained at higher temperatures:
  - (a) The statistical uncertainties obtained by the bootstrapping method are smallest at this temperature.
  - (b) Effects such as exchange reactions with the walls or the catalyst material are smaller at lower temperatures.
  - (c) The confidence in the reaction constant  $K(T)$  is very high due to the agreement of all fit scenarios.
  - (d) Additionally, it can be assumed that the equilibration constant is the same in the whole gas system, since there is only a minimal temperature gradient between the catalyst and the remaining system.

Thus, the results from the ‘binary fixed’ scenario at a setpoint temperature of 25 °C are regarded as the most reliable values and were chosen as the final results for the response function  $R_{x,\text{rel}}$ . The values and corresponding uncertainties are listed in table 5.4, as well as a comparison to the corresponding fit results obtained by the other fit scenarios. The systematic shift due to the fixing of different input parameters is in a similar range for both scenarios. The discussion above shows that this spread can be used as a measure for the systematic uncertainty;  $\Delta_x^{K\text{-fixed}}$  is used for this purpose since the shift is slightly larger. The final result can be obtained by adding the (total) statistical and systematic uncertainties in quadrature according to

$$\Delta_{\text{final}}^{\text{tot}} = \sqrt{\left(\sigma_{R_{x,\text{rel}}}^{\text{tot}}\right)^2 + \left(\Delta_x^{K\text{-fixed,tot}}\right)^2} \quad (5.15)$$

$$= \sqrt{\left(\sigma_{R_{x,\text{rel}}} \cdot R_{x,\text{rel}}\right)^2 + \left(\Delta_x^{K\text{-fixed}} \cdot R_{x,\text{rel}}\right)^2} . \quad (5.16)$$

Thus, the final results of the relative response functions valid for the LARA 1 system in the state as it were during the HYDE measurements are the following:

$$R_{\text{H}_2,\text{rel}} = 1.0128 \pm 0.0039 \quad (5.17)$$

$$R_{\text{HD},\text{rel}} = 1.0180 \pm 0.0035 \quad (5.18)$$

$$R_{\text{D}_2,\text{rel}} = 0.9692 \pm 0.0030 \quad (5.19)$$

The calibration uncertainty is better than 0.4%. This result shows that the HYDE method is well suitable for the production of accurate gas samples.

## 5.6 Comparison of the measurement results

After the HYDE measurements, the calibration was performed with the method based on theoretical Raman signal amplitudes as well, using the same Raman system (LARA 1) and taking care that no changes such as realignments occurred. The calibration procedure was described in detail in chapter 4. In the previous section, it was demonstrated that

**Table 5.4: Fit results of the relative response functions for 25 °C and ‘binary fixed’ scenario.** The values  $R_{x,\text{rel}}$  and their corresponding uncertainties  $\sigma_{R_{x,\text{rel}}}$  were obtained using the bootstrapping method. The table also shows the relative differences  $\Delta_x$  between the fit results obtained by the ‘binary fixed’ scenario and those obtained by the ‘all free’ and ‘ $K$  fixed’ scenarios. A complete tabulation of the results of all fit scenarios and at all catalyst temperature setpoints is given in appendix D.5.

x	$R_{x,\text{rel}}$	$\sigma_{R_{x,\text{rel}}} (\%)$	$\Delta_x^{\text{All-free}} (\%)$	$\Delta_x^{K\text{-fixed}} (\%)$
H <sub>2</sub>	1.0128	0.15	0.33	-0.35
HD	1.0180	0.29	-0.01	0.03
D <sub>2</sub>	0.9692	0.14	-0.33	0.33

**Table 5.5: Comparison of the results of the two calibration methods.** A comparison of both the relative values and the ratios of the response functions is given. The respective uncertainties were obtained by error propagation. The contribution of the spectral sensitivity uncertainty,  $\Delta_{\text{sens}}$ , to the total uncertainty of the corresponding approach was included to illustrate the effect of the comparatively high uncertainty for H<sub>2</sub> (cf. table 4.3 in section 4.7): due to the presence of  $R_{\text{H}_2}$  in the denominator of all relative response functions as well as in the first of the two ratios, the high uncertainty propagates into the uncertainties of all these values and dominates them.

	Theoretical Raman signals			HYDE		Difference (%)
	Value	$\Delta_{\text{sens}} (\%)$	$\Delta_{\text{tot}} (\%)$	Value	$\Delta_{\text{tot}} (\%)$	
$R_{\text{H}_2,\text{rel}}$	1.032	2.1	3.1	1.013	0.4	1.9
$R_{\text{HD},\text{rel}}$	1.013	2.1	2.8	1.018	0.3	-0.5
$R_{\text{D}_2,\text{rel}}$	0.955	2.2	2.9	0.969	0.3	-1.5
$R_{\text{H}_2}/R_{\text{D}_2}$	1.081	3.0	5.4	1.045	0.7	3.4
$R_{\text{HD}}/R_{\text{D}_2}$	1.061	1.0	4.9	1.050	0.3	1.0

the HYDE method can provide an accurate calibration of the Laser Raman system for the three inactive isotopologues H<sub>2</sub>, HD and D<sub>2</sub>. A comparison of the results of both approaches can thus be used to verify or falsify the calibration obtained by the theoretical Raman signal method for these molecules.

The results of both methods are shown in table 5.5. All relative response functions as well as the ratio  $R_{\text{HD}}/R_{\text{D}_2}$  agree to better than 2%; the only larger difference with a value of 3.4% is found for the ratio  $R_{\text{H}_2}/R_{\text{D}_2}$ . This is probably a consequence of the H<sub>2</sub>  $Q_1$ -branch lying outside the NIST-certified range for the determination of the spectral sensitivity with SRM 2242. Nevertheless, the results of both approaches agree well within the uncertainty of the values obtained by the method based on theoretical Raman signal amplitudes.

## 5.7 Conclusion

It was shown that the results obtained by the two independent calibration methods described in this and the previous chapter agree within the measurement uncertainty. This result represents a successful verification of the calibration based on theoretical Raman signal amplitudes for the non-tritiated hydrogen isotopologues. It provides confidence in

the underlying calculations as well as in the procedure for the spectral sensitivity determination, and thus in all calibration results obtained with the theoretical Raman signal method.

For this reason, a calibration of the laser Raman system for KATRIN based on named method is considered as feasible. Moreover, with an estimated calibration uncertainty of  $\leq 3.1\%$  for the relative response functions and  $\leq 5.4\%$  for the ratios, this approach is able to exceed the KATRIN trueness requirements of 10%.

## Chapter 6

# Summary and outlook

In the KATRIN experiment, laser Raman spectroscopy is used for the continuous monitoring of the tritium source gas composition. In order to reach the aimed sensitivity of 200 meV on the neutrino mass, systematic uncertainties have to be minimized in all areas of the experiment. With respect to the composition measurements, a precision of at least 0.1% and a trueness of at least 10% have to be achieved. The latter requires an accurate calibration of the Raman system for all hydrogen isotopologues.

A possible method for the calibration of the laser Raman system is based on theoretical Raman signal amplitudes, i.e. on a combination of calculated Raman intensities and the spectral sensitivity of the Raman system. The experimental determination of this spectral sensitivity was investigated within the scope of this thesis.

The eligibility of different calibration light sources for this task was examined. A comparison clearly showed the advantages of a NIST-certified luminescence standard (SRM 2242), especially with respect to the required replication of the Raman scattering region and the low calibration uncertainty, but also with respect to handling, price and lifetime.

However, the conditions under which the luminescence standard has to be employed in the LARA system differ from the ones which were used for the certification measurements by NIST. For this reason, the applicability of the standard to the KATRIN laser Raman setup was investigated in detail. Measurements were carried out to examine the influence of such factors as the positioning of the luminescence standard, the incident laser polarization and the laser power on the measurement results. The investigations showed that the challenges connected to the non-standard use of SRM 2242 can be successfully counteracted. Moreover, a measurement procedure for the correct determination of the spectral sensitivity was developed based on the results of these investigations. The validity of the results obtained by this procedure was confirmed by cross-checks, in which spectra of the same light source were taken at different Raman systems and compared before and after correction with the respective spectral sensitivity.

The calibration factors, the so-called response functions  $R$ , could be determined for all six hydrogen isotopologues by combining the obtained spectral sensitivity curve with calculated values for the respective theoretical Raman intensities. A second, independent calibration method based on the accurate production of calibration gas samples was used for cross-calibration. The relative response functions of the three non-radioactive hydrogen

isotopologues determined by both methods agree to better than 2% and thus well within the measurement uncertainty of  $< 3.1\%$ . For this reason, the calibration of the laser Raman system by the method based on theoretical Raman signal amplitudes is considered as feasible. Moreover, the KATRIN trueness requirements can be exceeded by this method. This result is an important step towards the determination of the neutrino mass with the design sensitivity of 200 meV.

**Outlook** This thesis presented a proof of concept of above-mentioned calibration method. For the use of the luminescence standard in the final LARA setup for KATRIN, several further steps should be considered:

- The final aim is to make the calibration procedure as uncomplicated as possible, so that occasional recalibrations of the LARA system between individual KATRIN measurement runs can be carried out by a non-specialist if necessary. The minimalistic custom-built mount of the luminescence standard (see e.g. figure 4.24 or the schematic sketch in figure 4.10(a)) was advantageous for a flexible use of SRM 2242 in the test measurements reported in this thesis; however, a more sophisticated, permanent mount should be developed for the use at KATRIN. The following features are suggested:
  1. The luminescence standard should be firmly connected to a dovetail mount. It should be aligned in such a way that it is automatically at the right position in the laser beam when the dovetail is inserted into its counterpart mount.
  2. A carefully aligned Raman window should be directly incorporated into the mount. Again, the dovetail would provide a fast and reproducible positioning without the need for a time-consuming alignment with a Raman cell body as described in 4.5.3.
  3. The mount should be stable and easy to handle. It should enclose the luminescence standard in such a way that there is no risk of the operator accidentally touching the glass slide itself.
  4. The Raman cell for KATRIN is located in the glove box which contains the parts of the KATRIN inner tritium loop (see figure 2.4 in the overview of the KATRIN experiment, section 2.2). For this reason, a closed, air-tight enclosure of the luminescence standard should be considered in order to avoid a contamination.<sup>1</sup>

A slightly modified Raman cell into which the luminescence standard can be inserted in the desired way is a promising option to fulfill these criteria.

- A KATRIN measurement run is planned to last about 60 days [KAT05]. In the following maintenance period, a recalibration of the Raman system is possible. A long-term investigation should be carried out to show if and how much the spectral sensitivity of an unaltered Raman system can be expected to change with time. From this, it can be judged if the required trueness of at least 10% can be assumed to be valid over the length of one measurement period. Furthermore, a recommendation of how frequently the LARA system should be recalibrated can be derived.

---

<sup>1</sup>From the NIST Certificate of Analysis: “The certification is nullified if the SRM is damaged, contaminated, or otherwise modified.” [NIS08]

- The certification of SRM 2242 is only valid until 01 January 2014 [NIS08]. This is not long enough to cover the whole measurement time of KATRIN. It is possible that the certification period will be extended or that a new luminescence standard with extended certification date will be available until then. However, if this should not be the case, it is suggested to continue to use SRM 2242 for the determination of the spectral sensitivity, and to additionally verify the validity of the obtained results by the methods presented in section 4.6 and chapter 5.
- In section 4.5.2, investigations of the influence of polarization on the measured SRM spectrum were presented. Interpretations of measurement results and theoretical considerations led to a conclusion concerning the laser polarization to be used in LARA calibration measurements: if a sheet polarizer is employed in the collection optics, the laser polarization has to be rotated by  $45^\circ$  to the polarization direction of the sheet polarizer. By this means, unequal transmission of the polarized and the unpolarized component of the luminescence light is compensated for.

A cross-check of this conclusion might be interesting. A possible investigation in this context could be a direct comparison of scrambler and polarizer in different polarization scenarios.

- The calibration method based on the controlled production of gas samples of accurately known composition provides a high calibration accuracy of better than 0.5%, as shown in chapter 5. However, it can up to now only be applied for the non-tritiated isotopologues  $H_2$  and  $D_2$  and their equilibration product HD. A future project is the extension of this method to all hydrogen isotopologues, using a suitable equilibration loop. The desired high accuracy requires thorough investigations of the effect of tritium's radioactivity on the gas mixing and equilibration process as well as on the performance of loop components such as the catalyst. If the method is proven to be successful, the tritium-containing gas samples may further improve the LARA calibration accuracy. Furthermore, this device may be used to calibrate or cross-check other KATRIN monitoring systems (e.g. the activity monitoring of the tritium source) as well.



## Appendix A

# Terminology of ‘accuracy’, ‘precision’ and ‘trueness’

The terms ‘accuracy’, ‘precision’ and ‘trueness’ are defined in the *International Vocabulary of Basic and General Terms in Metrology* (VIM) by the Joint Committee for Guides in Metrology as follows [Joi08]:

1. **Measurement accuracy** is the “closeness of agreement between a measured quantity value and a true quantity value of a measurand.”
2. **Measurement trueness** is the “closeness of agreement between the average of an infinite number of replicate measured quantity values and a reference quantity value.”
3. **Measurement precision** is the “closeness of agreement between indications or measured quantity values obtained by replicate measurements on the same or similar objects under specified conditions.”

For easier understanding, these terms are illustrated in figure A.1.

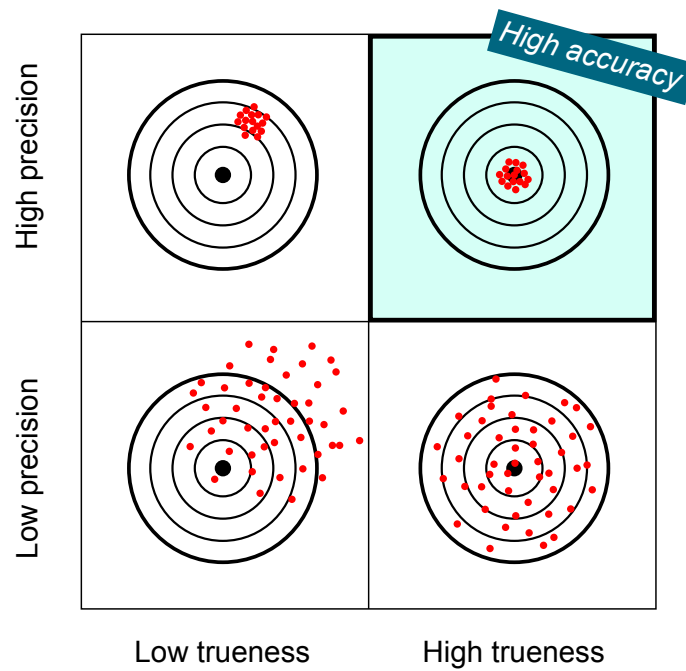


**Figure A.1: Precision, trueness and accuracy of a measurement.** In a precise measurement (*top*), the spread of single measurement values around the mean value is small. In a measurement with high trueness (*right*), the mean value of the measurement results is close to the true value. Precision and trueness are independent: a precise measurement is not necessarily true, and vice versa (*upper left, lower right*). The accuracy represents the degree of agreement between a single measurement value and the true value. Thus, in order for a measurement to be accurate, it has to be both precise and true (*upper right*).

## Appendix B

# Excited states of diatomic molecules

Excited states in molecules can arise from electronic, rotational and vibrational excitations. In the case of non-resonant Raman scattering, which is the case considered in this work, only rotational and vibrational excitations are of relevance. In the following, a theoretical treatment of these two excitations is given based on [Hak06] and [Lon02]. Since the focus in this thesis is on Raman spectroscopy of hydrogen isotopologues, the theory given here is restricted to the special case of diatomic molecules.

To understand the excitations of diatomic molecules, it is helpful to use semi-classical models of rotating and vibrating two-body systems. For the rotation of diatomic molecules, a rigid rotator is a simple model, while an oscillator serves as a first approximation for molecular vibration. Both models can be combined to the model of a non-rigid, oscillating rotator in order to describe rovibrational excitations. Figure B.1 illustrates the different models.

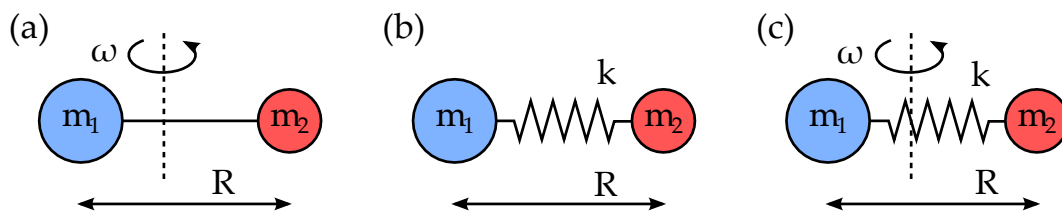


**Figure B.1: Models of excited diatomic molecules.** (a) Rigid rotator. In this model, the two atoms with masses  $m_1$  and  $m_2$  are located in a fixed distance  $R$  to each other and rotate around the molecule's center of mass with the angular frequency  $\omega$ . (b) Oscillator. The two atoms oscillate with the spring constant  $k$ . (c) Rotating oscillator. In this case, the molecule rotates and oscillates at the same time. (According to [Hak06].)

**Rotational excitation states** In the classical description, a simple rigid rotator as shown in figure B.1 (a), which rotates with an angular frequency  $\omega$ , has a rotational energy of

$$E_{\text{rot}} = \frac{1}{2}\Theta\omega^2 = \frac{L^2}{2\Theta} \quad (\text{B.1})$$

with the molecule's moment of inertia  $\Theta$  and the angular momentum  $L = \Theta\omega$ . In quantum mechanics, this angular momentum is quantized. The quantization conditions for such a rotating system are the same as the well-known ones for the electron-nucleus system of the hydrogen atom (see e.g. [Coh09]):

$$L = \hbar\sqrt{J(J+1)}, \quad J = 0, 1, 2, \dots \quad (\text{B.2})$$

with the rotational quantum number  $J$ . Thus, the quantized energy levels of rotational eigenstates are given by

$$E_{\text{rot}} = \frac{\hbar^2}{2\Theta}J(J+1). \quad (\text{B.3})$$

Due to the spin of the photon and the conservation of angular momentum, optical transitions are subject to the selection rule  $\Delta J = \pm 1$ . Accordingly, in case of Raman scattering the selection rule is  $\Delta J = 0, \pm 2$ , since two photons are involved. However, to illustrate the basic principle the more general one-photon case will be considered in the following.

The energy difference between the two states of such an optical transition corresponds to the energy of the involved photon and is thus connected to its frequency  $\nu$ :

$$E_{J+1} - E_J = h\nu. \quad (\text{B.4})$$

Instead of the frequency, the wavenumber  $\tilde{\nu} = \frac{\nu}{c}$  is the quantity commonly used in spectroscopy. Hence, the wavenumber shift between two rotational states with  $\Delta J = \pm 1$  is

$$\tilde{\nu}_{J \rightarrow J+1} = 2B(J+1) \quad \text{with} \quad B = \frac{h}{8\pi^2c\Theta}. \quad (\text{B.5})$$

The rotational constant  $B$  depends on the moment of inertia of the molecule and is thus characteristic for the type of molecule involved.

According to this equation, the rotational levels are evenly spaced. However, this is not experimentally observed; in reality, the lines move closer together with increasing  $J$ . The non-rigid rotator represents an improved model of diatomic rotation which takes centrifugal stretching of the molecule into account. Due to this stretching, the moment of inertia increases progressively with increasing  $J$ . Eq. (B.5) is modified to

$$\tilde{\nu}_{J \rightarrow J+1} = 2B(J+1) - 4D(j+1)^3 \quad (\text{B.6})$$

with the centrifugal stretching constant  $D > 0$ . Since the ratio  $\frac{D}{B}$  is typically in the order of  $10^{-4}$ , the corrections are relatively small. However, in high resolution spectroscopy, additional correction terms might be necessary in order to achieve a good description of the spectra.

**Vibrational excitation states** A simple model for diatomic vibration is the oscillation of two masses connected by a spring (see figure B.1 (b)). If the potential is approximated as quadratic,

$$V(R) = \frac{k}{2}(R - R_e)^2 \quad (\text{B.7})$$

with the internuclear distance  $R$ , the equilibrium distance  $R_e$ , and the spring constant  $k$ , then the oscillation is harmonic and the energy levels are given by (e.g. [Coh09])

$$E_{\text{vib,harmonic}} = \hbar\omega \left( v + \frac{1}{2} \right) = hc\tilde{\nu}_e \left( v + \frac{1}{2} \right), \quad v = 0, 1, 2, \dots \quad (\text{B.8})$$

with the quantum number  $v$ . For optical transitions between different vibrational states, the selection rule is  $\Delta v = \pm 1$ . Thus, the energy levels are equidistant:

$$E_{v+1} - E_v = hc\tilde{\nu}_e. \quad (\text{B.9})$$

The wavenumber  $\tilde{\nu}_e$  which corresponds to the eigenfrequency  $\nu_e$  of the harmonic oscillator is given by

$$\tilde{\nu}_e = \frac{1}{2\pi c} \sqrt{\frac{k}{\mu}}, \quad (\text{B.10})$$

where  $\mu = \frac{m_1 \cdot m_2}{m_1 + m_2}$  is the reduced mass of the molecule.

As an approximation, the quadratic potential is acceptable for small  $v$ . With increasing internuclear distance  $R$ , however, the atomic bond is weakened to the point of dissociation of the molecule, which is not accounted for by this approximation. A better approximation for the resulting anharmonic oscillator is the empirical potential function called Morse potential:

$$V(R) = D_e \cdot \left( 1 - e^{-a(R-R_e)} \right)^2 \quad \text{with} \quad a = \tilde{\nu}_e \cdot \sqrt{\frac{\mu}{2D_e}}. \quad (\text{B.11})$$

$D_e$  denotes the dissociation energy. The energy levels are in this case given by

$$E_{\text{vib,anharmonic}} = E_{\text{vib,harmonic}} \cdot \left( 1 - x_e \left( v + \frac{1}{2} \right) \right), \quad (\text{B.12})$$

where  $x_e > 0$  is the anharmonicity constant. It is typically of the order of 0.01. Like in the rotational case, higher order correction terms can be added in order to describe the observed energy levels even more accurately. Additionally, it should be noted that for anharmonic oscillation, the selection rule  $\Delta v = \pm 1$  of the harmonic oscillator is modified due to the possibility of exciting overtones:

$$\Delta v = \pm 1, \pm 2, \pm 3, \dots \quad (\text{B.13})$$

However, the probability of exciting such transitions with  $|\Delta v| > 1$  is very low compared to the probability of the main transition with  $\Delta v = \pm 1$ .

Figure B.2 shows the potential curves and energy levels for both the quadratic and the Morse potential.

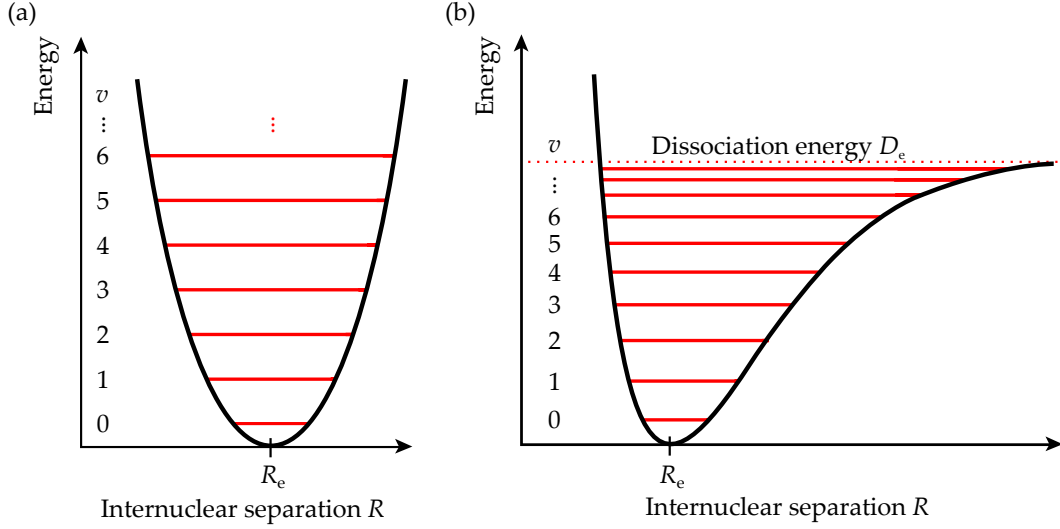


**Figure B.2: Potential curves and energy levels of oscillating systems.** (a) Quadratic potential (harmonic oscillation); (b) Morse potential (anharmonic oscillation). In the anharmonic case, the energy levels move closer together with increasing quantum number  $v$ . (According to [Hak06].)

**Rovibrational excitation states** The two types of excitation, rotation and vibration, are not independent of each other. Since the mean internuclear separation  $R$  increases with increasing vibrational excitation, the resulting increase in the molecule's moment of inertia  $\Theta$  leads to a decrease in the rotational constant  $B$  (see eq. (B.5)). Thus, apart from the centrifugal stretching mentioned above, so-called vibrational stretching has to be taken into account in the description of rovibrational excitation. The dependence of the rotational constant  $B$  and the stretching constant  $D$  on the vibrational quantum number  $v$  is considered by the modifications

$$B_v = B - \alpha \left( v + \frac{1}{2} \right) , \quad (\text{B.14})$$

$$D_v = D - \beta \left( v + \frac{1}{2} \right) , \quad (\text{B.15})$$

where  $\alpha, \beta$  are numbers which are characteristic for the molecule. Using the Morse potential (eq. (B.11)), the rovibrational energy levels are now given by

$$E(v, J) = \hbar\omega_e \left( v + \frac{1}{2} \right) - x_e \hbar\omega_e \left( v + \frac{1}{2} \right)^2 + hcB_v J(J+1) - hcD_v J^2(J+1)^2 . \quad (\text{B.16})$$

In high resolution spectroscopy, further influences have to be considered which add minor correction terms to these energy levels. For ordinary spectroscopic systems as the one used for KATRIN, however, the approximation given above provides a sufficiently good description of the obtained spectra.

## Appendix C

# Determination of the spectral sensitivity by using a stabilized, calibrated LED light source

An approach for the determination of the spectral sensitivity based on stabilized LEDs was investigated within the scope of this work and the master's thesis of S. Napoli [Nap12]. The approach was suggested by H. H. Telle [Tel11]. The basic principle as well as details of the realization are presented in the following section.

Furthermore, different ideas for the reproduction of the Raman scattering region with light from the LED source were considered within the frame of this work. They are presented and discussed in section C.2.

### C.1 Stabilization and calibration of the LED light source

#### C.1.1 Basic principle

As a semiconductor device, an LED produces a spectrum which is almost entirely dependent on two parameters only: current and temperature [Dav12]. By stabilizing these parameters, a stable and reproducible spectrum can be achieved. Once calibrated itself, the stabilized LED light source can be used as a reproducible calibration light source for the spectral sensitivity determination.

#### C.1.2 The LED source

Several LEDs are necessary to cover the  $Q_1$ -branches of all hydrogen isotopologues.<sup>1</sup> The spectra of the three LEDs chosen for this purpose are shown in figure C.1. A schematic sketch of the LED source and a description of the main components is found in figure C.2.

---

<sup>1</sup>A white light LED would be able to cover the full wavelength region. However, investigations show that the reliability of such LEDs based on phosphor conversion is limited due to aging processes, which effect both the total intensity and the spectral distribution (see e.g. [Men10]).

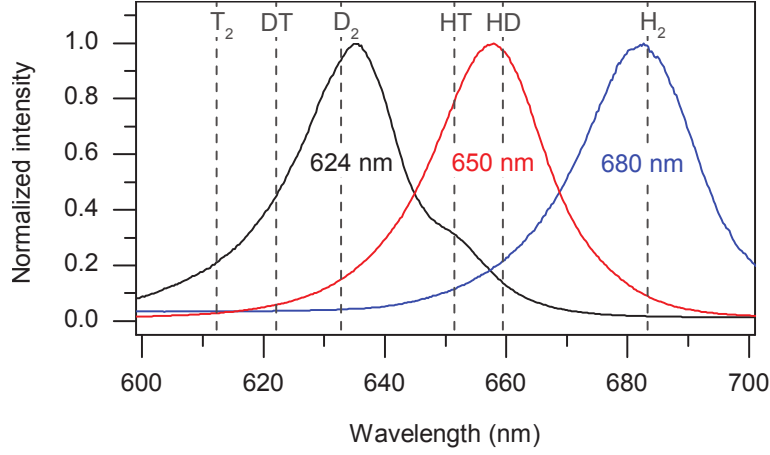


**Figure C.1: Coverage of the  $Q_1$ -branches of all hydrogen isotopologues by three LEDs.** The LEDs used are the models OPE5T62UO ( $\lambda_p=624$  nm), ELD-650-523 (650 nm) and LED-680-02AU (680 nm) from Roithner Lasertechnik GmbH ([www.roithner-laser.com](http://www.roithner-laser.com)). Note that the peak wavelengths of the shown measurements curves differ by several nanometers from the peak wavelengths  $\lambda_p$  given in the data sheets.

### C.1.3 Calibration of the LED source

Two methods were proposed for the calibration of the LED source. They are briefly presented in the following; a detailed description and discussion is found in the master's thesis of S. Napoli [Nap12].

Both methods are based on the use of a calibrated photodiode. The idea is in principle to scan through the LED spectrum step by step, exposing the photodiode to light of an only narrow wavelength region out of the total spectrum in each step. By this means, the LED spectrum can be obtained. In order to derive the actual calibration spectrum from the measured values, the influence of the measurement system on the spectrum has to be considered, i.e. the influence of the photodiode as well as the one coming from the mechanism which allows to scan through the spectrum. The spectral response of the calibrated photodiode is provided by the manufacturer<sup>2</sup>. Concerning the second part, two possible methods were considered, which allow a scanning in such a way that the resulting influence on the spectrum can be accounted for:

**Calibration method based on narrowband band-pass filters** In the first method, interference band-pass filters<sup>3</sup> with a bandwidth of 3 nm are used to isolate a narrow wavelength region which is transmitted while light of other wavelengths is reflected. The transmitted wavelength depends on the angle at which light is incident on the filter. Thus, by rotating the filter, it is possible to scan through an extended wavelength region in narrow steps. To cover the whole wavelength region of the  $Q_1$ -branches of the hydrogen isotopologues, several filters with different peak transmission wavelengths are needed.

The following equation relates the photocurrent  $J_{f,\alpha}^{\text{PD}}$ , which is measured by the photodiode

<sup>2</sup>Hamamatsu Photonics, [www.hamamatsu.com](http://www.hamamatsu.com)

<sup>3</sup>from Knight Optical, [www.knightoptical.com](http://www.knightoptical.com)

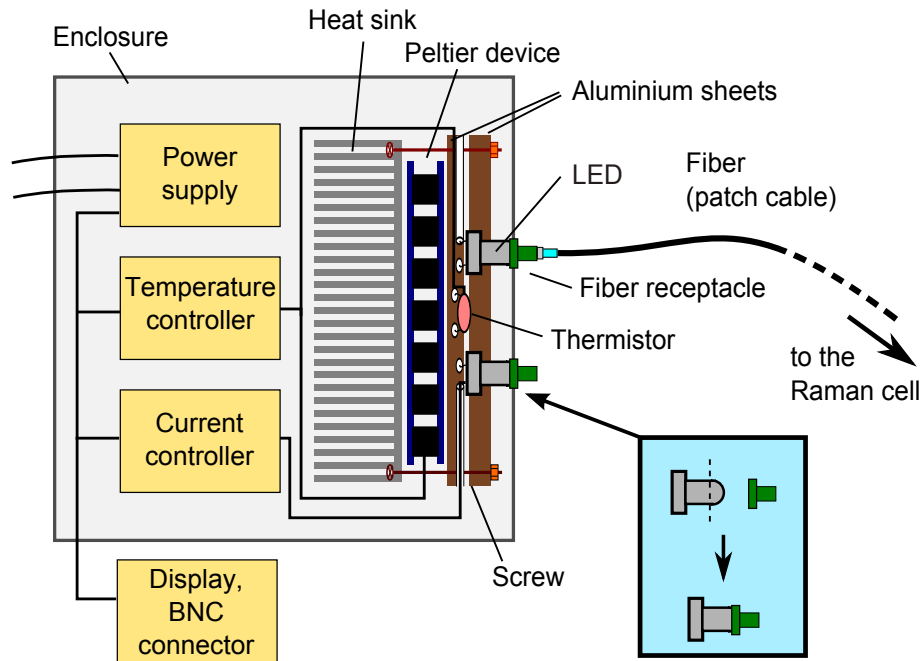


**Figure C.2: Schematic sketch of the LED source (not to scale).** The LED light can be directly coupled into an optical fiber via SMA receptacles (Laser Components, [www.lasercomponents.com](http://www.lasercomponents.com)). The top of each LED was machined off in order to allow for effective coupling, as illustrated in the inset. The LEDs are held in place between two aluminium sheets with grooves to lead the wires outside. (Note that only two LEDs are shown here for reasons of clarity. In the actual source, five LEDs are employed: the three LEDs named in figure C.1 plus two additional ones to extend the covered spectral region.) The LED temperature is stabilized by a feedback loop comprising temperature controller, thermistor and Peltier device (all from Analog Technologies, [www.analogtechnologies.com](http://www.analogtechnologies.com)). The thermistor is located close to the LEDs between the aluminium sheets and attached to the back sheet with thermal conductance glue. Thermal compound connects the Peltier device to the other side of this sheet as well as to a heat sink. If the measured LED temperature differs from the set temperature, the temperature controller activates the Peltier device for cooling or heating, respectively. The LED current is stabilized by a voltage-controlled current source. Temperature and current values can be read out via BNC connectors. For a picture of the LED source see figure 4.2.

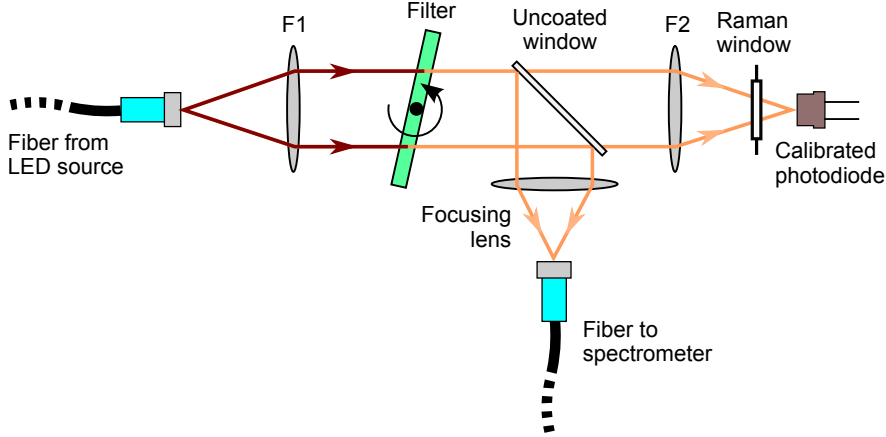


**Figure C.3: Schematic sketch of the calibration setup using filters (top view).** Light coming from the LED source is collimated and passed through a rotatable band-pass filter, which allows only a narrow wavelength region to be transmitted. An uncoated window at an angle of  $45^\circ$  to the beam direction splits the beam, so that it can be simultaneously imaged onto the calibrated photodiode and a spectrometer. The Raman window and the optics used for the replication of the scattering region (here represented by the optics F1, F2) are included in the calibration procedure.

for a certain filter  $f$  and a certain angle of rotation  $\alpha$ , to the real LED intensity  $I_{f,\alpha}^{\text{LED}}(x)$ :

$$J_{f,\alpha}^{\text{PD}} = \int c(x) \cdot T_{f,\alpha}(x) \cdot I_{f,\alpha}^{\text{LED}}(x) dx . \quad (\text{C.1})$$

$x$  denotes spectrometer pixel (which can be converted to wavelength),  $c(x)$  is the spectral response of the photodiode which is provided in form of a calibration curve by the manufacturer, and  $T_{f,\alpha}(x)$  denotes the transmission function of a filter  $f$  at an angle  $\alpha$ .

The principle measurement setup is shown in figure C.3. The imaging of the filtered LED light on both the photodiode and a spectrometer allows for a simultaneous measurement of the photocurrent  $J_{f,\alpha}^{\text{PD}}$  and the shape and relative intensity of the signal. The spectrometer is used to obtain the filter transmission function by comparing the intensity measured for a certain filter setting,  $I_{f,\alpha}^{\text{Sp}}(x)$ , to the intensity  $I_{\text{tot}}^{\text{Sp}}(x)$  measured if no filter is employed, i.e. if the full LED spectrum is measured by the spectrometer:

$$T_{f,\alpha}(x) = \frac{I_{f,\alpha}^{\text{Sp}}(x)}{I_{\text{tot}}^{\text{Sp}}(x)} . \quad (\text{C.2})$$

Note that the calibration results are independent of the spectral sensitivity of the spectrometer, since its influence cancels out when taking above ratio. Analysis methods which allow to extract the LED spectrum  $I_{f,\alpha}^{\text{LED}}(x)$  from the integral in eq. (C.1) were proposed within the scope of this thesis and the thesis of S. Napoli with contributions by M. Schlösser and T. James. They are described in detail in [Nap12].

**Calibration method based on the use of a prism** In the second method a prism is used to disperse the light, so that only a narrow wavelength region is imaged onto the photodiode. The latter is mounted on a mechanical arm which can be rotated to allow

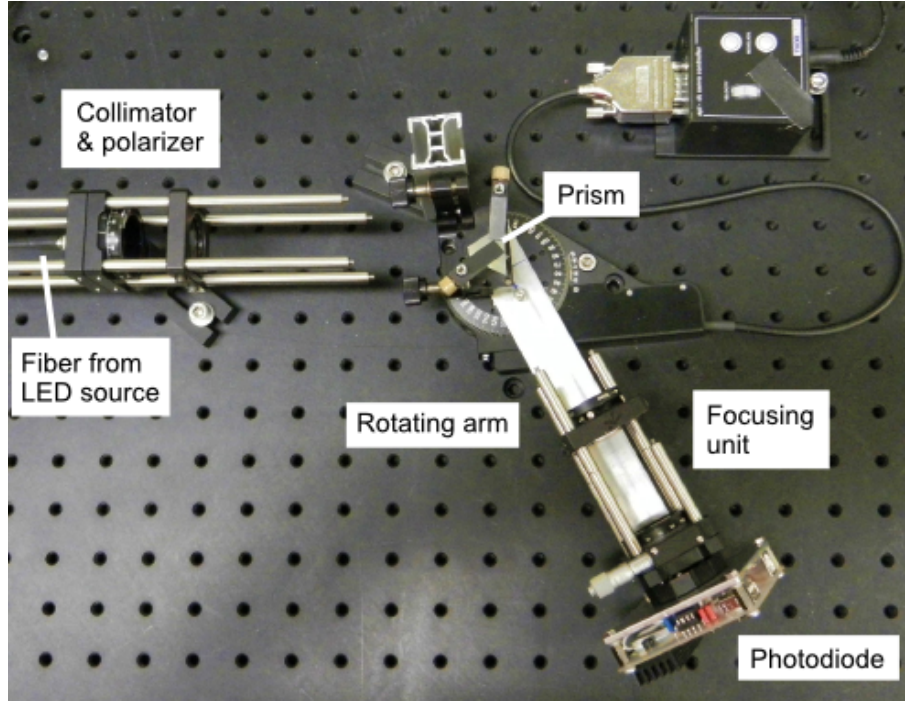


**Figure C.4: Calibration setup using a prism (top view).** The LED light coming from the fiber on the left side is collimated and polarized, before the beam is incident on the prism in an angle of  $56^\circ$ . The prism is mounted on a kinematic stage above the rotation stage which controls the rotating arm. The average exit point of light from the prism is chosen as the pivot point, around which the arm and thus the photodiode mounted to it rotates.

to scan through the spectrum. This setup represents essentially a prism spectrometer. A picture of a first test setup is shown in figure C.4.

In principle the same relation between wavelength-dependent LED intensity  $I^{\text{LED}}(\lambda)$  and photocurrent  $J_\alpha^{\text{PD}}$  as in case of the filter setup applies (cf. eq. (C.1)):

$$J^{\text{PD}}(\alpha) = \int c(\lambda) \cdot T(\lambda(\alpha)) \cdot I^{\text{LED}}(\lambda) d\lambda . \quad (\text{C.3})$$

Again,  $c(\lambda)$  is the photodiode response and  $T(\lambda(\alpha))$  the transmission function. The latter depends in this case on the angle of rotation of the mechanical arm,  $\alpha$ , which defines the position of the photodiode and thus the wavelength region which is observed. In contrast to the filter setup described above, the comparatively simple optical setup in this case allows a calculation of the transmission function. An appropriate modeling and simulation was performed by S. Napoli; for further details, the reader is referred to her master's thesis [Nap12].

## C.2 Replication of the Raman scattering region

The necessity of a good replication of the Raman scattering region was discussed in section 4.3. The Raman light is observed from a 6 mm long part of the elongated scattering volume

and with emission angles between  $0^\circ$  and  $12.7^\circ$  to the optical axis of the collection optics (cf. 4.3.3); to mimic both aspects simultaneously is a challenging task. Several approaches were considered:

**Use of a cylindrical lens** A cylindrical lens focuses a collimated beam onto a line, as illustrated in figure C.5. However, the different emission angles are well mimicked in the  $y$ - $z$ -plane<sup>4</sup> only; in the  $x$ - $y$ -plane, in contrast, the light is exclusively aligned parallel to the  $y$ -axis.

**Use of a movable concave mirror** Light from a point-like source can be imaged onto a point again by convex lenses or concave mirrors. In this case, the desired angular distribution can be easily achieved. A possible way to account for the line shape of the scattering region is illustrated in figure C.6: the light is focused into the Raman cell by a concave mirror, which can be moved parallelly to the laser beam path in small steps, e.g. with a piezo motor. For each step, the spectrum has to be measured, so that the final spectrum can be obtained by averaging over all single spectra. However, it would have to be investigated if this procedure leads to the desired result, i.e. a correct replication of the scattering region.

**Use of a diffuser** Another possibility which was considered is the use of a diffuser. There are so-called “Engineered Diffusers” available from RPC Photonics (<http://www.rpcphotonics.com/engineered.asp>), which – according to the manufacturer – are able to turn an incident collimated beam of light into diffuse light with specified intensity profile and divergence angles. However, a custom diffuser which could exactly meet the requirements costs around \$5000 or \$6000 [Tho12b]. A cheaper, non-custom line diffuser provides the right light pattern shape, but not the desired divergence angles. Alternatively, a simple ground glass diffuser providing these angles might be used in combination with (1) a cylindrical lens, which illuminates the diffuser with a line-shaped pattern; (2) an optical slit with the dimensions of the scattering region, which is positioned directly (2a) in front of or (2b) behind the diffuser. However, again it would have to be investigated if this leads to the desired results. In the cases (1) and (2a) especially, it is not clear if the diffuser works properly if light is incident not as a collimated beam with a certain diameter, but as a narrow line.

In all cases, an additional challenge is the accuracy in the sub-millimeter range desired for the replication of the position of the Raman scattering region. Also, optical aberrations like chromatic aberrations are introduced by most optical components; they have to be taken into account as well. These aspects emphasize the advantages of a calibration light source like the luminescence standard SRM 2242, which is employed directly at the scattering region without additional optics. This is one important reason why the LED approach was not further pursued in favor of the luminescence standard approach.

---

<sup>4</sup>as defined in the figure

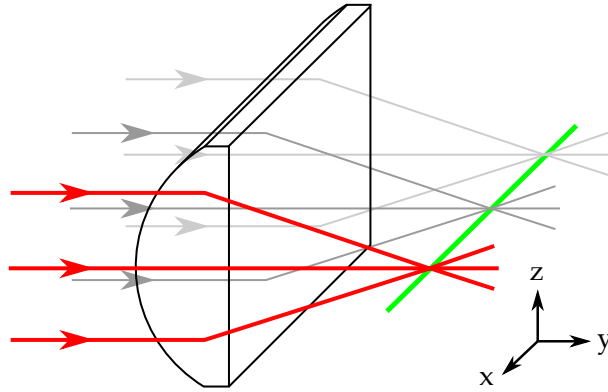


Figure C.5: Cylindrical lens.

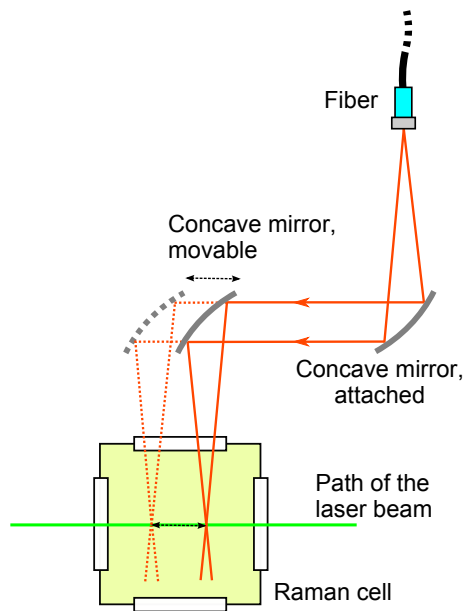


Figure C.6: Replication of the Raman scattering region by using a movable mirror.



# Appendix D

## Supplements to the HYDE measurements

### D.1 Measurement procedure of the HYDE measurements

The following measurement procedure is based on the procedure developed by H. Seitz [Sei11]. The following abbreviations are used: RP001 and RP002 are the pressure gauges which measure the pressure at the H<sub>2</sub> vessel BD001 and the D<sub>2</sub> vessel BD002. HV0 $xx$  with different digits  $xx$  denote valves. RF001 is the flow controller.

Date \_\_\_\_\_ Mixing \_\_\_\_\_ Operator \_\_\_\_\_

#### HYDE+ operation procedure sheet

(Version 3.3, edited by Simone Rupp/Magnus Schlösser, 11.06.2012)

#### Settings of Laser Raman System

Laser power	CCD-Temp	CCD-gain	CCD-readout	Slit width	Acquisition time	Number of spectra
Folder						

#### Data taking

Start of Lara measurements	Start of Yokogawa data acquisition
Laser shutter open ? <input type="checkbox"/>	
External shutter open? <input type="checkbox"/>	

Date \_\_\_\_\_ Mixing \_\_\_\_\_ Operator \_\_\_\_\_

**Operations at HYDE+ loop**

Time	Duration	Action	RP001	RP002	RF001 (FL1/SP1)	T <sub>heater</sub>	T <sub>catalyst</sub>	Check
<b>Evacuation and preparation</b>								
		Check if catalyst has been heated to 300°C for 3h in vacuum						
		Check if system has been evacuated with all valves open <5*10 <sup>-4</sup> mbar at turbo pump						
		Set catalyst temperature regulator to 300°C						
		Set offset of RP001, RP002 = 0 mbar						
<b>Filling of vessels (Pre-Run)</b>								
		Close all valves and switch off turbo pump						
		Fill BD001 (H <sub>2</sub> ) via HV005, HV010						
		Fill BD002 (D <sub>2</sub> ) via HV006, HV020						
		Close HV020, HV010						
		Open HV011, HV021						
<b>Mixing of gas (Pre-Run)</b>								
		Open HV022, HV033, HV034, HV035, (HV036,) HV037, HV012						

Page 2 / 7

Date \_\_\_\_\_ Mixing \_\_\_\_\_ Operator \_\_\_\_\_

		Start metal bellow pump						
		Set flow controller to 6 SL/M						
	1min	Mixing						
	1min	Block stream via closing HV011						
	1min	Unblock stream via opening HV011						
	1min	Block stream via closing HV022						
	1min	Unblock stream via opening HV022						
	1min	Block stream via closing HV011						
	1min	Unblock stream via opening HV011						
	1min	Block stream via closing HV022						
	1min	Unblock stream via opening HV022						
	1min	Mixing						
<b>Catalytic operation (Pre-Run)</b>								
		Check T <sub>heater</sub> (300°C ?) and T <sub>catalyst</sub>						
		Open HV044, HV045, close HV037						
	30min	Circulate gas through catalyst						

Page 3 / 7

Date	Mixing	Operator
<b>Evacuation and preparation (Main-Run)</b>		
	Set $T_{\text{heater}}$ to 25°C	
	Switch off heater	
1h	Wait until $T_{\text{catalyst}}=25^{\circ}\text{C}$	
	Switch off metal bellow pump	
1h	Open all valves apart from HV005, HV006, evacuate system $<2 \cdot 10^{-5}$ mbar at turbo pump	
<b>Filling of vessels (Main-Run)</b>		
	Close all valves and switch off turbo pump	
	Fill BD001 ( $\text{H}_2$ ) via HV005, HV010	
	Fill BD002 ( $\text{D}_2$ ) via HV006, HV020	
	Close HV020, HV010	
	Open HV050, HV051, HV052 and switch on turbo pump (if it's down to 0Hz, else wait until it is)	
	Open HV011, HV021	
<b>Mixing of gas (Main-Run)</b>		
	Open HV022, HV033, HV034, HV035, (HV036,) HV037, HV012	
	Switch on heater and check $T_{\text{heater}}$ (25°C) and $T_{\text{catalyst}}$ (25°C)	

Page 4 / 7

Date	Mixing	Operator
	Start metal bellow pump	
5min	Mixing	
1min	Block stream via closing HV011	
1min	Unblock stream via opening HV011	
1min	Block stream via closing HV022	
1min	Unblock stream via opening HV022	
1min	Block stream via closing HV011	
1min	Unblock stream via opening HV011	
1min	Block stream via closing HV022	
1min	Unblock stream via opening HV022	
10min	Mixing	
<b>Catalytic operation (Main-Run)</b>		
	Check $T_{\text{heater}}$ (25°C ?) and $T_{\text{catalyst}}$	
	Open HV044, HV045, close HV037	
30min	Circulate gas through catalyst	
	Install beam dump	Laser on again?

Page 5 / 7

Date	Mixing	Operator
	10min	Circulate gas through catalyst
		Remove beam dump
		Set $T_{\text{heater}}$ to 50°C
	30min	Circulate gas through catalyst
		Install beam dump
	10min	Circulate gas through catalyst
		Remove beam dump
		Set $T_{\text{heater}}$ to 75°C
	30min	Circulate gas through catalyst
		Install beam dump
	10min	Circulate gas through catalyst
		Remove beam dump
		Set $T_{\text{heater}}$ to 100°C
	30min	Circulate gas through catalyst
		Install beam dump
	10min	Circulate gas through catalyst

Page 6 / 7

Date	Mixing	Operator
		Remove beam dump
		Set $T_{\text{heater}}$ to 125°C
		Close HV050 and switch off turbo pump
	30min	Circulate gas through catalyst
		Install beam dump
	10min	Circulate gas through catalyst
		Remove beam dump
		Stop LARA data acquisition
		Switch off metal bellow pump
<b>End measurement</b>		
	10min	Open all valves, evacuate system
	(3h)	When $p_1, p_2 < 0.5\text{mbar}$ : Set $T_{\text{heater}}$ to 300°C
		Switch off heater
	(3h)	Switch on heater again before the next measurement starts

Page 7 / 7

## D.2 Correction of the $Q_1$ -branch of HD

In the analysis of HYDE measurements, absolute Raman signal amplitudes were obtained by determining the peak area of each  $Q_1$ -branch (cf. section 3.1.4). However, figure D.1 shows that the  $Q_1$ -branch of HD is overlapped by an  $O_1$ -branch line of  $H_2$  and an  $S_1$ -branch line of  $D_2$ . The resulting increase in measured peak area had to be corrected for: otherwise, the Raman signal amplitude is no longer linear with the mole fraction of HD present in the mixture. According to eq. (3.6), there is a linear relationship between the intensities of different lines of a Raman spectrum. If the corresponding proportionality constant  $c_x$  is known, it is possible to deduce the peak area of a  $S$ - or  $O$ -branch line from the measured peak area of the  $Q_1$ -branch of the same isotopologue. Thus, the corrected area of the  $Q_1$ -branch of HD can be calculated from the measured areas  $S_x$  as follows:

$$S_{HD,corr} = S_{HD} - c_{H_2} \cdot S_{H_2} - c_{D_2} \cdot S_{D_2} . \quad (D.1)$$

Measurements with pure  $H_2$  and  $D_2$  were used to obtain the correction factors  $c_x$ , which are given by the area of the  $O_1(J'' = 3)$  or  $S_1(J'' = 4)$  peak divided by the area of the corresponding  $Q_1$ -branch. In case of  $D_2$ , the double peak visible in the inset of figure D.1 had to be deconvoluted first. This was done by fitting two single peaks to the double peak structure using the *ShapeFit* routine described in [Jam12a] (see also the following section D.3). The obtained correction factors ( $c_{H_2} = 2.55 \cdot 10^{-3}$ ,  $c_{D_2} = 2.91 \cdot 10^{-3}$ ) were used to correct the area of the  $Q_1$ -branch of HD in all HYDE measurements.

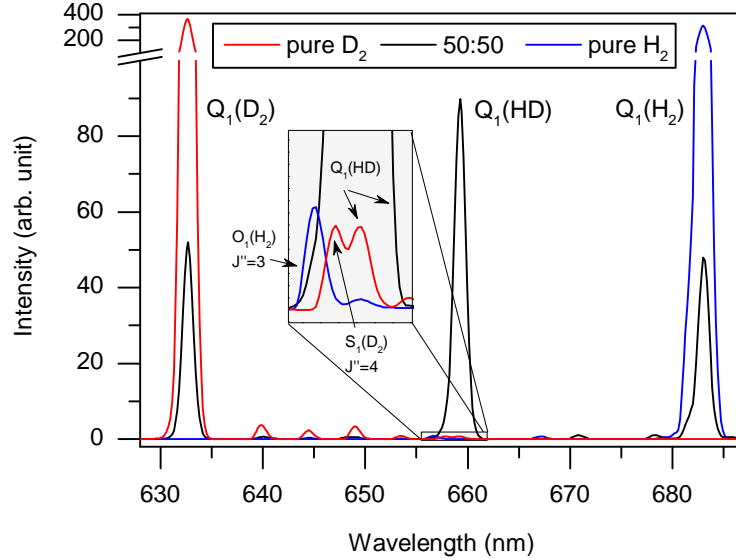


**Figure D.1: Overlap of hydrogen Raman peaks.** The plot shows the measured spectra of (i) pure  $H_2$  gas, (ii) pure  $D_2$  gas and (iii) an equilibrated  $H_2$ -HD- $D_2$  mixture with an initial  $H_2$ : $D_2$ -ratio of 50:50. A zoom into the region of the  $Q_1$ -branch of HD makes visible that this branch overlaps with the  $O_1(J'' = 3)$ -line of  $H_2$  and the  $S_1(J'' = 4)$ -line of  $D_2$ . Note that the  $Q_1$ -branch of HD is visible in the spectrum of ‘pure’  $D_2$  as well: the  $D_2$  gas purity is only 99.7%, with the remaining 0.3% being HD.

### D.3 Determination of Raman signal amplitudes using the *ShapeFit* method

Within the scope of this work, the peak area of a  $Q_1$ -branch, which was used as the absolute Raman signal amplitude of the respective isotopologue (cf. section 3.1.4), was obtained by summing up the intensity values of all pixels within a peak profile. As discussed in the previous section, this requires a correction of overlapping peaks. An alternative way to obtain Raman signal amplitudes without the need of such a correction is based on a fit of the Raman spectra. This is explained in more detail in the following.

The open-source spectral analysis software described in [Jam12a] provides a tool named *ShapeFit*, which is a fitting algorithm based on numerical line shape profiles. In an improved version of this software [Sch12c], it is possible to define multiple profiles and fit them to a spectrum. Thus, taking Raman spectra of  $H_2$ , HD and  $D_2$  as obtained in the HYDE measurements as an example, the following procedure leads to a determination of the Raman signal amplitudes:

1. In a first step, a line which has sufficient intensity and which does not overlap with other lines is selected from a spectrum taken at the Raman system employed (e.g. a line from a spectral calibration lamp). The shape of this peak represents a typical shape obtained at this specific system for an incident line-shaped light signal. Additionally, the shape of the  $Q_1$ -branch of HD is selected from a HYDE spectrum with a large HD fraction.<sup>1</sup> The two peaks are used to fit the double peak structure consisting of the  $O_1(J'' = 3)$ -line of  $D_2$  and the  $Q_1$ -branch of HD in the spectrum of ‘pure’  $D_2$  gas (cf. figure D.1 and explanations in the previous section). By subtracting the fitted HD  $Q_1$ -branch from the spectrum, the spectrum of  $D_2$  is corrected for the small HD impurity.<sup>2</sup>
2. The Raman spectrum of pure  $H_2$  gas and the HD-corrected one of pure  $D_2$  gas are taken as a whole as fit profiles. They are fitted to the spectrum of an equilibrated  $H_2$ -HD- $D_2$ -mixture. The residual spectrum represents the spectrum of pure HD.
3. The spectra of the three pure gases are normalized in such a way that the  $Q_1$ -branch area has the same value in each case.
4. These normalized spectra can then be used to fit all HYDE spectra. The fitted intensity of each spectrum represents the respective Raman signal amplitude.

Figure D.2 shows the normalized spectra obtained as described above for the three pure gases which are used in the HYDE measurements. If extended to the tritiated hydrogen isotopologues, this procedure can be included in the automated analysis of LARA spectra during KATRIN measurement runs. Care has to be taken in the determination of the Raman spectra of pure  $T_2$ , DT and HT, since  $T_2$  gas is limited in purity, so that corrections similar to the one described in step 1. for  $D_2$  will be necessary. A possible alternative

<sup>1</sup>If the relative Raman signal of HD is large, the distortion of the  $Q_1$ -branch peak shape due to the overlapping  $S$ - and  $O$ -branch line (cf. section D.2) is negligible.

<sup>2</sup>HD peaks other than the  $Q_1$ -branch are negligibly small (noise level) in the spectrum of ‘pure’  $D_2$  and do not have to be corrected for.

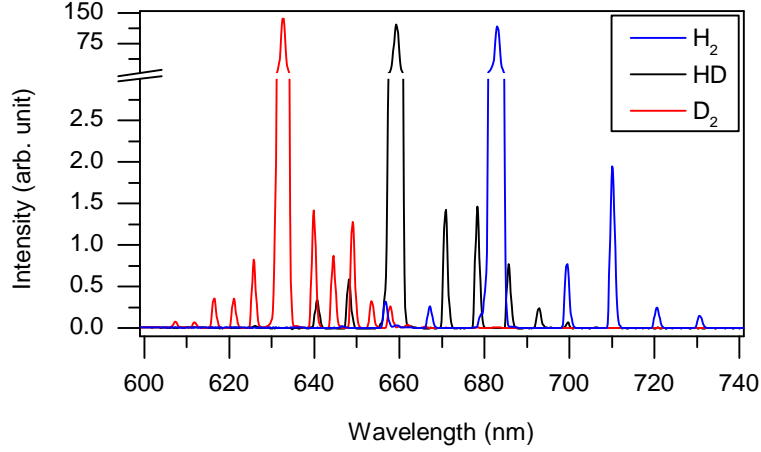


**Figure D.2:** Raman spectra of pure  $\text{H}_2$ ,  $\text{HD}$  and  $\text{D}_2$  gas. (See main text for further explanations.)

approach to obtain the spectra of pure gases is the convolution of theoretical Raman signal amplitudes (cf. section 4.1) with the typical line shape obtained for the Raman system employed (see step 1. above). This approach was suggested by M. Schlösser and is currently under investigation.

## D.4 Correlation of the fit parameters

A typical correlation matrix obtained for a fit of HYDE data, in which none of the fit parameters  $R'_{\text{H}_2}$ ,  $R'_{\text{HD}}$ ,  $R'_{\text{D}_2}$  and  $K(T_0)$  is fixed, is shown below. This specific matrix was obtained for the ‘all free’ fit scenario at a setpoint temperature of 25 °C.

$$A_{\text{Kor}} = \begin{pmatrix} 0.567385 & 0.572052 & 0.54653 & 3.73884 \cdot 10^{-5} \\ 0.572052 & 0.576777 & 0.551033 & -1.05005 \cdot 10^{-4} \\ 0.54653 & 0.551033 & 0.526455 & 3.55317 \cdot 10^{-5} \\ 3.73884 \cdot 10^{-5} & -1.05005 \cdot 10^{-4} & 3.55317 \cdot 10^{-5} & 1.70188 \cdot 10^{-3} \end{pmatrix}$$

Column and row index 1 stands for  $R'_{\text{H}_2}$ , 2 for  $R'_{\text{HD}}$ , 3 for  $R'_{\text{D}_2}$  and 4 for  $K$ . The strong correlation of the response functions among each other is clearly visible, while the  $R'_x$  and  $K$  values are only marginally correlated.

## D.5 All fit results of the HYDE measurements

Table D.1 contains the fit results of all HYDE fit scenarios ('All free', 'Binary fixed', 'K fixed'; cf. section 5.5.1) and for all temperature setpoints. The results are also plotted in the figures 5.3 and 5.4 in chapter 5.

**Table D.1: Results of all fit scenarios and at all catalyst temperature setpoints.** The statistical uncertainty  $\sigma$  was obtained by bootstrapping.  $T$  is the catalyst temperature setpoint. This table is included in a publication submitted to Analytical Chemistry [Sch12g].

$T$ (°C)	$R_{\text{H}_2,\text{rel}}$		$R_{\text{HD},\text{rel}}$		$R_{\text{D}_2,\text{rel}}$		$K(T)$	
	Value	$\sigma_{\text{rel}}$ (%)	Value	$\sigma_{\text{rel}}$ (%)	Value	$\sigma_{\text{rel}}$ (%)	Value	$\sigma_{\text{rel}}$ (%)
<i>All free</i>								
25	1.0094	0.28	1.0181	0.26	0.9725	0.25	3.26	3.09
50	1.0075	0.32	1.0203	0.28	0.9722	0.28	3.32	3.74
75	1.0058	0.36	1.0230	0.31	0.9712	0.30	3.36	4.37
100	1.0045	0.47	1.0268	0.38	0.9687	0.37	3.37	5.54
125	1.0028	0.65	1.0332	0.52	0.9640	0.52	3.36	7.80
<i>Binary fixed</i>								
25	1.0128	0.15	1.0180	0.29	0.9692	0.14	3.27	3.53
50	1.0116	0.17	1.0202	0.34	0.9681	0.16	3.32	4.03
75	1.0103	0.21	1.0228	0.42	0.9669	0.20	3.36	4.92
100	1.0084	0.27	1.0265	0.52	0.9651	0.25	3.38	6.05
125	1.0053	0.37	1.0327	0.72	0.9620	0.35	3.37	7.85
<i>K fixed</i>								
25	1.0092	0.23	1.0183	0.21	0.9724	0.20	3.26	-
50	1.0081	0.26	1.0191	0.22	0.9729	0.21	3.34	-
75	1.0070	0.28	1.0205	0.22	0.9724	0.21	3.40	-
100	1.0068	0.36	1.0222	0.27	0.9710	0.26	3.46	-
125	1.0071	0.47	1.0246	0.35	0.9684	0.37	3.52	-

# Bibliography

- [Aba11] K. Abazajian et al., *Cosmological and astrophysical neutrino mass measurements*, *Astropart. Phys.* **35**, 4 (2011) 177–184.
- [Ade08] H. Ader et al., *Advising on Research Methods: a consultant's companion*, Johannes Van Kessel Publishing, Huizen, NL (2008).
- [Aih11] H. Aihara et al., *The Eighth Data Release of the Sloan Digital Sky Survey: First Data from SDSS-III*, *ApJS* **193**, 2 (2011) 29.
- [Ant12] V. Antonelli et al., *Solar neutrinos*, *Adv. High Energy Phys.* (in press) (2012).
- [Ase11] V. Aseev et al., *An upper limit on electron antineutrino mass from Troitsk experiment*, *Phys. Rev.* **D84** (2011) 112003.
- [Atk06] P. W. Atkins et al., *Physical chemistry*, Oxford University Press, Oxford, UK, 8th edition (2006).
- [Aug12] M. Auger et al., *Search for Neutrinoless Double-Beta Decay in  $^{136}\text{Xe}$  with EXO-200*, *Phys. Rev. Lett.* **109** (2012) 032505.
- [Bab12] M. Babutzka et al., *Monitoring of the properties of the KATRIN Windowless Gaseous Tritium Source*, *New J. Phys.* **14** (2012).
- [Bar80] R. Barbieri et al., *Neutrino Masses in Grand Unified Theories*, *Phys. Lett. B* **90** (1980) 91.
- [Bor11] B. Bornschein, *Between Fusion and Cosmology - The Future of the Tritium Laboratory Karlsruhe*, *Fusion Sci. Technol.* **60**, 3 (2011) 1088–1091.
- [Boy08] R. W. Boyd, *Nonlinear optics*, Academic Press, Burlington, MA, USA, 3rd edition (2008).
- [Bru97] R. Brun et al., *ROOT – An object oriented data analysis framework*, *Nucl. Instrum. Methods Phys. Res., Sect. A* **389**, 1-2 (1997) 81–86.
- [Cho07] S. J. Choquette et al., *Relative Intensity Correction of Raman Spectrometers: NIST SRMs 2241 Through 2243 for 785 nm, 532 nm, and 488 nm/514.5 nm Excitation*, *Appl. Spectrosc.* **61**, 2 (2007) 117–129.
- [Cho12] S. J. Choquette, *Extended range data for SRM 2242 with 532 nm excitation*, personal communication via e-mail, National Institute for Standards and Technology (2012).

- [Chr76] K. Christmann et al., *Adsorption of hydrogen on a Pt(111) surface*, Surf. Sci. **54** (1976) 365–392.
- [Coh09] C. Cohen-Tannoudji et al., *Quantenmechanik*, volume 1, de Gruyter, Berlin, GER, 4th edition (2009).
- [Con12] J. Conrad et al., *Short baseline neutrino oscillation experiments*, Adv. High Energy Phys. (in press) (2012).
- [Dav12] M. W. Davidson, *Fundamentals of Light-Emitting Diodes (LEDs)*, Carl Zeiss Microscopy Online Campus (2012).
- [Dem06] W. Demtröder, *Experimentalphysik: Elektrizität und Optik*, volume 2, Springer-Verlag, Berlin, GER, 4th edition (2006).
- [Dem07] W. Demtröder, *Laserspektroskopie: Grundlagen und Techniken*, Springer-Verlag, Berlin, GER, 5th edition (2007).
- [Dem12] D. Demange et al., *Overview of R&D at TLK for process and analytical issues on tritium management in breeder blankets of ITER and DEMO*, Fusion Eng. Des. **87**, 7-8 (2012) 1206–1213.
- [Dos06] N. Doss et al., *Molecular effects in investigations of tritium molecule  $\beta$  decay endpoint experiments*, Phys. Rev. C **73** (2006) 025502.
- [Dre12] G. Drexlin et al., *Current Direct Neutrino Mass Experiments*, Adv. High Energy Phys. (in press) (2012).
- [Efr83] B. Efron et al., *A Leisurely Look at the Bootstrap, the Jackknife, and Cross-Validation*, The American Statistician **37**, 1 (1983) 36–48.
- [Efr94] B. Efron et al., *An Introduction to the Bootstrap*, Chapman and Hall/CRC, New York, USA (1994).
- [Eic09] F. Eichelhardt, *Measurement of the Tritium Pumping Properties of a 4.2 K Argon Condensate for the Cryogenic Pumping Section of KATRIN*, Ph.D. thesis, Universität Karlsruhe (TH) (2009).
- [Fel98] G. J. Feldman et al., *Unified approach to the classical statistical analysis of small signals*, Phys. Rev. D **57** (1998) 3873–3889.
- [Feo61] P. P. Feofilov, *The physical basis of polarized emission*, Consultants Bureau, New York, USA (1961).
- [Fer94] J. R. Ferraro et al., *Introductory Raman spectroscopy*, Acad. Press, Boston, USA, 1st edition (1994).
- [Fis10] S. Fischer, *Investigations of laser stability in the KATRIN Raman setup and first depolarisation measurements with tritium at TLK*, Diploma thesis, Karlsruhe Institute of Technology (2010).

- [Fis11] S. Fischer et al., *Monitoring of tritium purity during long-term circulation in the KATRIN test experiment LOOPINO using laser Raman spectroscopy*, Fusion Sci. Technol. **60** (2011) 925–930.
- [Gam12] Gamma Scientific, *RS-10D Calibration Light Source Data Sheet* (2012).
- [Giu12] A. Giuliani et al., *Neutrinoless Double Beta Decay*, Adv. High Energy Phys. (in press) (2012).
- [Goo12] GoodFellow, *Tungsten wire - Material Information* (2012), <http://www.goodfellow.com/A/Tungsten-Wire.html>.
- [Hak06] H. Haken et al., *Molekülphysik und Quantenchemie: Einführung in die experimentellen und theoretischen Grundlagen*, Springer-Lehrbuch, Springer-Verlag, Berlin, GER, 5th edition (2006).
- [Han04] S. Hannestad, *Neutrinos in cosmology*, New J. Phys. **6** (2004) 108.
- [Har12] J. J. Hartnell et al., *Long baseline neutrino oscillation experiments*, Adv. High Energy Phys. (in press) (2012).
- [Her11] P. Herwig, *Kalibrierung des KATRIN Laser-Raman-Systems mit nicht-tritiierten Wasserstoffisotopologen*, Diploma thesis, Karlsruhe Institute of Technology (2011).
- [Hol94] L. Holder et al., *Depolarization measurements of light propagating through an image fiber*, J. Opt. **25**, 4 (1994) 139.
- [Höt12] M. Hötzel, *Simulation and analysis of source-related effects for KATRIN*, Ph.D. thesis, Karlsruhe Institute of Technology (2012).
- [Int01] International Organization for Standardization, *ISO6142: Gas analysis – Preparation of calibration gas mixtures – Gravimetric method*, 2nd edition (2001).
- [Int03a] International Organization for Standardization, *ISO6144 Gas analysis – Preparation of calibration gas mixtures – Static volumetric method* (2003).
- [Int03b] International Organization for Standardization, *ISO6145 Gas analysis – Preparation of calibration gas mixtures using dynamic volumetric methods* (2003).
- [Jam12a] T. M. James et al., *Automated Quantitative Spectroscopic Analysis Combining Background Subtraction, Cosmic-Ray Removal and Peak Fitting*, submitted to Appl. Spectrosc. (2012).
- [Jam12b] T. M. James et al., *Precise Depolarization Ratio Measurements for all Diatomic Hydrogen Isotopologues*, publication in preparation (2012).
- [Joi93] Joint Committee for Guides in Metrology, *Guide to the expression of uncertainty in measurement*, International Organization for Standardization, Genève, 1st edition (1993).

- [Joi08] Joint Committee for Guides in Metrology, *International Vocabulary of Basic and General Terms in Metrology (VIM)*, *JCGM 200:2008*, International Organization for Standardization, Genève, 3rd edition (2008).
- [Kaj12] T. Kajita, *Atmospheric Neutrinos*, Adv. High Energy Phys. (in press) (2012).
- [Kat81] H. Katsuta et al., *Hydrogen and Deuterium Transport through Type 304 Stainless Steel at Elevated Temperatures*, J. Nucl. Sci. Technol. **18**, 2 (1981) 143–151.
- [KAT05] KATRIN collaboration, J. Angrik et al., *KATRIN Design Report 2004*, FZKA Scientific Report **7090** (2005).
- [Kla06] H. V. Klapdor-Kleingrothaus et al., *The evidence for the observation of  $0\nu\beta\beta$  decay: the identification of  $0\nu\beta\beta$  events from the full spectra*, Mod. Phys. Lett. A **21**, 20 (2006) 1547–1566.
- [Köll11] Z. Köllö et al., *A new method to measure small volumes in tritium handling facilities using  $p$ - $V$  measurements*, Fusion Sci. Technol. **60**, 3 (2011) 972–975.
- [Kom11] E. Komatsu et al., *Seven-year Wilkinson Microwave Anisotropy Probe (WMAP) Observations: Cosmological Interpretation*, ApJS **192**, 2 (2011) 18.
- [Kos12] A. Kosmider, *Tritium Retention Techniques in the KATRIN Transport Section and Commissioning of its DPS2-F Cryostat*, Ph.D. thesis, Karlsruhe Institute of Technology (2012).
- [Kra05] C. Kraus et al., *Final results from phase II of the Mainz neutrino mass search in tritium beta decay*, Eur. Phys. J. C **40** (2005) 447–468.
- [Las12] T. Lasserre et al., *Reactor Neutrinos*, Adv. High Energy Phys. (in press) (2012).
- [LeR11] R. LeRoy, *Recalculation of Raman transition matrix elements of all hydrogen isotopologues for 532nm laser excitation*, personal communication, University of Waterloo (2011).
- [Les12] J. Lesgourgues et al., *Neutrino mass from cosmology*, Adv. High Energy Phys. (in press) (2012).
- [Lew07] R. Lewis, *Development of a Raman System for In-Line Monitoring of Tritium at the Karlsruhe Tritium Neutrino (KATRIN) Experiment*, Ph.D. thesis, Swansea University (2007).
- [Lon02] D. A. Long, *The Raman effect : a unified treatment of the theory of Raman scattering by molecules*, Wiley, Chichester, GB (2002).
- [Lor02] T. J. Loredo et al., *Bayesian analysis of neutrinos observed from supernova SN-1987A*, Phys. Rev. **D65** (2002).
- [McC06] R. L. McCreery, *Photometric Standards for Raman Spectroscopy*, in: Handbook of Vibrational Spectroscopy, John Wiley & Sons, Hoboken, NJ, USA (2006).
- [McQ00] D. A. McQuarrie, *Statistical mechanics*, Univ. Science Books, Sausalito, CA, USA (2000).

- [Men10] G. Meneghesso et al., *Recent results on the degradation of white LEDs for lighting*, Journal of Physics D: Applied Physics **43**, 35 (2010) 354007.
- [Mes06] D. Meschede, *Gerthsen Physik*, Springer-Lehrbuch, Springer-Verlag, Berlin, GER, 23rd edition (2006).
- [Mir11] S. Mirz, *Aufbau und Charakterisierung eines verbesserten Laser-Raman-Systems für das KATRIN-Experiment*, Bachelor's thesis, Karlsruhe Institute of Technology (2011).
- [Miz94] M. Mizuno et al., *Determination of hydrogen concentration in austenitic stainless steels by thermal desorption spectroscopy*, Mater. Trans., JIM **35**, 10 (1994) 703–707.
- [Moh80] R. N. Mohapatra et al., *Neutrino Mass and Spontaneous Parity Violation*, Phys. Rev. Lett. **44** (1980) 912.
- [Nap12] S. Napoli, *Absolute Calibration of Laser Raman Signals for the Karlsruhe Tritium Neutrino (KATRIN) experiment*, Master's thesis, Swansea University (2012).
- [New12] Newport Corporation, *Calibrated Sources and Services*, Newport Resource e-Catalog (2012) 233–234.
- [Nis06] M. Nishi et al., *Study on tritium accountancy in fusion DEMO plant at JAERI*, Fusion Eng. Des. **81**, 1-7 (2006) 745–751.
- [NIS08] *Standard Reference Material 2242*, National Institute of Standards & Technology, Gaithersburg, MD, USA (2008).
- [Oce12a] Ocean Optics, *DH-2000-CAL Deuterium Tungsten Halogen Calibration Standard*, [www.oceanoptics.com/products/dh2000cal.asp](http://www.oceanoptics.com/products/dh2000cal.asp) (2012).
- [Oce12b] Ocean Optics, *STAN-RAM532 – NIST-Traceable Raman Standards*, [www.oceanoptics.com/products/stanram.asp](http://www.oceanoptics.com/products/stanram.asp) (2012).
- [Oht11] T. Ohta et al., *HD gas analysis with gas chromatography and quadrupole mass spectrometer*, Nucl. Instrum. Methods Phys. Res., Sect. A **640**, 1 (2011) 241–246.
- [Oht12] T. Ohta et al., *Distillation of hydrogen isotopes for polarized HD targets*, Nucl. Instrum. Methods Phys. Res., Sect. A **664**, 1 (2012) 347–352.
- [Ott08] E. Otten et al., *Neutrino mass limit from tritium beta decay*, Rept. Prog. Phys. **71** (2008).
- [Par03] S. Parker, *McGraw-Hill dictionary of scientific and technical terms*, The McGraw-Hill Companies, Inc., New York, USA, 6th edition (2003).
- [PDG12] Particle Data Group, J. Beringer et al., *The Review of Particle Physics*, Phys. Rev. **D86**, 010001 (2012).

- [Pau30] W. Pauli, *Offener Brief an die Gruppe der Radioaktiven bei der Gauvereins-Tagung zu Tübingen* (1930).
- [Pel03] M. J. Pelletier, *Quantitative Analysis Using Raman Spectrometry*, Appl. Spectrosc. **57**, 1 (2003) 20A–42A.
- [Pri10a] Princeton Instruments, *Data Sheet for Acton Standard Series, Spectrograph Model SP2150* (2010).
- [Pri10b] Princeton Instruments, *Grating Efficiency Curve for Spectrograph SP2150, 600 g/mm with 500 nm blast* (2010), [www.princetoninstruments.com/products/spec/actonseries/dsheet.aspxf](http://www.princetoninstruments.com/products/spec/actonseries/dsheet.aspxf).
- [Pri11] Princeton Instruments, *Data Sheet for PIXIS Series, CCD Model PIXIS: 2KB* (2011).
- [Ram28] C. V. Raman et al., *A New Type of Secondary Radiation*, Nature **121** (1928) 501–502.
- [Ray97] K. Ray et al., *Simplified calibration of instrument response function for Raman spectrometers based on luminescent intensity standards*, Appl. Spectrosc. **51**, 1 (1997).
- [Rei56] F. Reines et al., *The Neutrino*, Nature **178** (1956) 446–449.
- [Rob91] R. G. H. Robertson et al., *Limit on  $\bar{\nu}_e$  mass from observation of the  $\beta$  decay of molecular tritium*, Phys. Rev. Lett. **67** (1991) 957–960.
- [Sch87] C. Schwartz et al., *Nonadiabatic eigenvalues and adiabatic matrix elements for all isotopes of diatomic hydrogen*, J. Mol. Spectrosc. **121**, 2 (1987) 420–439.
- [Sch97] N. Schmitz, *Neutrinophysik*, Teubner, Stuttgart, GER (1997).
- [Sch09] M. Schlösser, *First Laser Raman measurements with tritium for KATRIN and studies of systematic effects of the LARA system*, Diploma thesis, Karlsruhe Institute of Technology (2009).
- [Sch11a] M. Schlösser, *The cLARAbrator – a tool for a true in-situ calibration source of the quantum efficiency of a LARA system*, Internal report, Karlsruhe Institute of Technology (2011).
- [Sch11b] M. Schlösser et al., *Design Implications for Laser Raman Measurement Systems for Tritium Sample-Analysis, Accountancy or Process-Control Applications*, Fusion Sci. Technol. **60** (2011) 976–981.
- [Sch12a] M. Schlösser, personal communication, Karlsruhe Institute of Technology (2012).
- [Sch12b] M. Schlösser, *PhD thesis in preparation*, Ph.D. thesis, Karlsruhe Institute of Technology (2012).
- [Sch12c] M. Schlösser, *ShapeFit Deluxe*, personal communication, Karlsruhe Institute of Technology (2012).

- [Sch12d] M. Schlösser et al., *Accuracy of the Laser Raman system for KATRIN*, Proc. Int. School of Physics 'E. Fermi', Course CLXXXII 'Neutrino Physics and Astrophysics', ed. G. Bellini (IOS, Amsterdam; SIF, Bologna), arXiv/1203.4099 (2012) 333–336.
- [Sch12e] M. Schlösser et al., *Accurate Calibration of the Laser Raman System for the Karlsruhe Tritium Neutrino Experiment*, J. Mol. Struct. (in press) (2012).
- [Sch12f] M. Schlösser et al., *Evaluation method for Raman depolarization measurements including geometrical effects and polarization aberrations*, J. Raman Spectrosc. (in press) (2012).
- [Sch12g] M. Schlösser et al., *In-Line Calibration of Process or Stand-alone Raman Systems for Analysis of Gas Mixtures with Sub-percent Accuracy*, submitted to Anal. Chem. (2012).
- [Sch12h] M. Schlösser et al., *Supplementary material to: Accurate Calibration of the Laser Raman System for the Karlsruhe Tritium Neutrino Experiment*, J. Mol. Struct. (in press) (2012).
- [Sei11] H. Seitz, *Kalibrierung des KATRIN Laser-Raman Systems mit katalytisch hergestellten, inaktiven Wasserstoffisotopologmischungen*, Bachelor's thesis, Karlsruhe Institute of Technology (2011).
- [Sem12] Semrock Inc., Rochester, NY, USA, *532 nm RazorEdge ultrasteep long-pass edge filter (LP03-532RU-25)* (2012), <http://www.semrock.com/FilterDetails.aspx?id=LP03-532RU-25>.
- [Sou86] P. C. Souers, *Hydrogen Properties for Fusion Energy*, University of California Press, Berkeley, CA, USA (1986).
- [Ste84] P. Steeger et al., *Polarization preservation in circular multimode optical fibers and its measurement by a speckle method*, J. Lightwave Technol. **2**, 4 (1984) 435–441.
- [Stu10a] M. Sturm, *Aufbau und Test des Inner-Loop-Systems der Tritiumquelle von KATRIN*, Ph.D. thesis, Karlsruhe Institute of Technology (2010).
- [Stu10b] M. Sturm et al., *Monitoring of all hydrogen isotopologues at tritium laboratory Karlsruhe using Raman spectroscopy*, Laser Phys. **20** (2010) 493–507.
- [Tay01] D. J. Taylor et al., *Enhanced Raman sensitivity using an actively stabilized external resonator*, Rev. Sci. Instrum. **72**, 4 (2001) 1970–1976.
- [Tel11] H. H. Telle, personal communication, Department of Physics, Swansea University (2011).
- [Tho12a] Thorlabs Inc., *Achromatic Depolarizers*, Thorlabs Product Catalog (2012), [www.thorlabs.com/catalogpages/V21/926.pdf](http://www.thorlabs.com/catalogpages/V21/926.pdf).
- [Tho12b] Thorlabs Tech Support, M. Scott, *Engineered Diffusers*, personal communication via e-mail, Thorlabs Inc. (2012).

- [Uda92] T. Uda et al., *Hydrogen Isotope Exchange Reaction Rates in Tritium, Hydrogen and Deuterium Mixed Gases*, *Radiochim. Acta* **56** (1992) 209–214.
- [Vei87] D. K. Veirs et al., *Raman Line Positions in Molecular Hydrogen: H<sub>2</sub>, HD, HT, D<sub>2</sub>, DT, and T<sub>2</sub>*, *Journal of Molecular Spectroscopy* **121** (1987) 401–419.
- [Yan80] T. Yanagida, *Horizontal Symmetry and Masses of Neutrinos*, *Prog. Theor. Phys.* **64** (1980) 1103.

# Danksagung

Diese Arbeit wäre ohne die Unterstützung und Mitarbeit vieler Personen nicht möglich gewesen. Ich möchte mich bei allen bedanken, die – jeder auf seine Weise – zum Gelingen beigetragen haben.

Ich danke Prof. Dr. Guido Drexlin dafür, dass er mir die Durchführung dieser spannenden und lehrreichen Arbeit ermöglicht hat.

Sehr herzlich möchte ich Dr. Beate Bornschein für ihr außerordentliches Engagement danken, mit dem sie sich um die optimale Förderung jedes einzelnen Studenten bemüht und dabei nie nur den angehenden Wissenschaftler, sondern stets den ganzen Menschen im Blick hat.

Ich danke Prof. Helmut H. Telle, der die Arbeit aus der Ferne begleitet hat und durch seine Fachkompetenz viele Fragen klären und Denkanstöße geben konnte.

Mein besonderer Dank gilt Magnus Schlösser für die gute Zusammenarbeit und die vielen hilfreichen Diskussionen, insbesondere aber auch für all die Zeit und Mühe, die in die hervorragende Betreuung dieser Arbeit geflossen sind.

Auch danke ich Sebastian Fischer für die stete Hilfsbereitschaft.

Für die gute Zusammenarbeit und das angenehme Arbeitsumfeld möchte ich der gesamten Laser-Raman-Gruppe danken: Dr. Beate Bornschein, Sebastian Fischer, Timothy James, Florian Kassel, Bennet Krasch, Silvia Napoli, Vera Schäfer, Magnus Schlösser, Dr. Michael Sturm, Prof. Dr. Helmut H. Telle.

Silvia Napoli danke ich für die sehr gute Zusammenarbeit und die äußerst herzliche Aufnahme bei meinem Besuch in Swansea. Auch Timothy James und Prof. Dr. Helmut H. Telle möchte ich nochmals für ihren Einsatz und die produktive Zeit in Swansea danken.

Ein herzlicher Dank geht an Hans-Dieter Adami, der stets die Zeit fand, sich meiner technischen Fragen, Probleme und besonderen Fertigungswünsche anzunehmen.

Danken möchte ich auch Steffen Jokisch für das Fräsen von Leiterplatten sowie Marco Röllig, Florian Priester und Martin Babutzka für ihre Hilfe bei Elektronikproblemen.

Ebenso danke ich Dirk Osenberg für seinen zuverlässigen, allmorgendlichen Einsatz während der HYDE-Messphase sowie Catalin-Gabriel Alecu für seine Hilfe mit dem Drucksensor.

Steven Choquette von NIST möchte ich für die unkomplizierte Kommunikation und das Bereitstellen von Messdaten herzlich danken.

Bedanken möchte ich mich auch bei Eva Porter und Sylvia Krieger, ohne die ich im Kampf mit den Formularen unweigerlich verloren gewesen wäre.

Für das sehr angenehme Arbeitsklima und die freundliche Aufnahme danke ich herzlich allen Mitarbeitern des TLK. Mein besonderer Dank gilt den anderen Diplomanden sowie Doktoranden und Bachelor-Studenten für die schöne gemeinsame Zeit.

Schließlich möchte ich meinem Freund Philip danken, der mich auch während der stressigsten Phasen der Diplomarbeit nicht nur tapfer ertragen hat, sondern mir stets hilfreich zur Seite stand.

Der letzte große Dank gebührt meinen Eltern. Sie haben mich immer in jeglicher Hinsicht unterstützt. Danke dafür!